

UNIVERSITY OF OKLAHOMA

GRADUATE COLLEGE

NANO INTEGRATED LITHIUM POLYMER ELECTROLYTES BASED ON  
ANODIC ALUMINUM OXIDE (AAO) TEMPLATES

A DISSERTATION

SUBMITTED TO THE GRADUATE FACULTY

in partial fulfillment of the requirements for the

Degree of

DOCTOR OF PHILOSOPHY

By

ROSHAN S. P. BOKALAWELA  
Norman, Oklahoma  
2012

NANO INTEGRATED LITHIUM POLYMER ELECTROLYTES BASED ON  
ANODIC ALUMINUM OXIDE (AAO) TEMPLATES

A DISSERTATION APPROVED FOR THE  
HOMER L. DODGE DEPARTMENT OF PHYSICS AND ASTRONOMY

BY

---

Dr. Matthew Johnson, Chair

---

Dr. Gregory Parker

---

Dr. Michael Santos

---

Dr. Sheena Murphy

---

Dr. Daniel Glatzhofer



## **Acknowledgements**

First, I wish to express my sincere honor and deep appreciation to my advisor, Professor Matthew B. Johnson, who has been so generous with his time and commitment to my success. I have greatly benefitted from his unconditional and exceptional support, which was an invaluable combination of teaching, supervision, leadership and expertise in both research and private life. His support and help were most valuable during both my exam periods and whenever I had to overcome difficulties in life.

My research would have been far behind if it was not for the support from my lab partner Jeremy Jernigan; his skills in the machine shop provided me with outstanding progress throughout this research work. So I express my greatest possible thanks to him.

I would also like to thank my graduate committee members; Prof. Gregory Parker, Prof. Sheena Murphy, Prof. Michael Santos, and Prof. Daniel Glatzhofer for their mentoring and support throughout graduate evaluations and the thesis work.

I also express gratitude and thanks to Professor Roger Frech and his students Dr. Matt Petrowsky and Allison Fleshman; they supported my research and provided a glovebox and lab space for my work in addition to discussions throughout the research, leading me to a successful end. Special thanks go to Professor Frech for his help with my research data especially IR and Raman

spectra and for discussions for manuscript preparation which was a great learning stage.

I also greatly appreciate and thank to Dr. Brian Grady for x-ray studies and spending time with us to evaluate x-ray data for manuscript preparation.

I also greatly acknowledge and thank Dr. Preston Larson and Dr. Joel Keay, whose expertise in scanning electron microscopy and technological applications, gave me immense help and advice related to SEM and laboratory work. Also their careful guidance in experimental methods gave me exceptional knowledge about laboratory work. Also their corrections and comments on my thesis were invaluable and led to the best possible outcome.

I am sincerely thankful to all my research group colleagues, Kevin Hobbs, Justin Lawyer, Dr. Mark Curtis, Chris Crowe, and all the other members who throughout this research gave me a great help and made it a priority in the lab.

All the faculty and staff members of the Department of Physics and Astronomy, the staff of the OU Graduate College and the International Student Services are gratefully acknowledged for helping in numerous ways throughout my graduate studies.

## Table of Contents

Acknowledgements.....	iv
List of Tables.....	xi
List of Figures.....	xii
Abstract.....	xix
Chapter 1: Introduction to Electrochemical Materials.....	1
1.1 Introduction.....	1
1.2 Electrochemical materials and applications.....	2
1.3 Polymer electrolytes .....	6
1.4 Properties of PEO polymer and PEO:LiTf(X:1) electrolytes .....	8
1.5 Anodized aluminum oxide (AAO) and applications .....	14
1.5.1 Introduction to AAO template fabrication .....	16
1.5.2 AAO pore growth mechanism.....	18
1.6 Introduction to next chapters .....	20
1.7 Introduction to appendices.....	21
Chapter 2: Introduction to Materials Characteristic Properties .....	23
2.1 Introduction.....	23
2.2 Molecular vibrations and vibrational spectra .....	23
2.3 X-ray scattering and materials physical properties.....	26
2.3.1 Estimation of crystal size.....	27
2.3.2 Determination of degree of crystallinity.....	28
2.3.3 PEO crystal structure and fiber patterns.....	29

2.4	Ionic transport in materials .....	30
2.4.1	Arrhenius equation. ....	31
2.4.2	Vogel-Tamman-Fulcher (VTF) equation.....	32
2.4.3	Williams-Landel-Ferry (WLF) equation .....	32
2.5	Scanning electron microscopy (SEM).....	33
Chapter 3: Experimental Details.....		36
3.1	Introduction.....	36
3.2	Fabrication of AAO templates.....	37
3.2.1	Annealing of AAO templates.....	41
3.2.2	Transferring annealed AAO into the inert atmospheric glove box.....	41
3.3	Coating of SiO <sub>2</sub> layers onto AAO pore walls.....	42
3.4	PEO polymer and PEO:LiTf(X:1) <sub>X=10,30</sub> bulk films fabrication.....	44
3.5	Vacuum-pulling of polymers into AAO pores .....	45
3.6	Removal of excess polymer from top and bottom of AAO.....	47
Chapter 4: Characterization of PEO and PEO:LiTf- Polymer Materials Filled AAO.....		48
4.1	Introduction.....	48
4.2	Scanning electron microscopy (SEM).....	48
4.3	FTIR spectra .....	50
4.4	FT-Raman spectra.....	52
4.5	WAXS diffractograms .....	54

4.6	AC-impedance spectra and conductivity.....	57
4.6.1	Determination of ionic conductivity in nano-pores.....	62
Chapter 5: Results and Discussion .....		64
5.1	Introduction.....	64
5.2	AC-impedance and ionic conductivity .....	66
5.2.1	Nyquist plots for AC-impedances for the bulk PEO:LiTf(10:1) polymer electrolyte and confined systems .....	67
5.2.2	Ionic conductivities of bulk PEO:LiTf(10:1) polymer electrolyte and confined systems .....	70
5.2.3	Conductance (30 °C) per Pore vs. Pore Diameter.....	73
5.3	Analysis of FTIR and Raman spectra.....	75
5.4	WAXS patterns and structural analysis .....	89
5.5	Summary and Conclusions .....	101
Bibliography.....		105
Appendix 1: Complementary tables and figures for FTIR and FT-Raman spectra		113
A1.1	FTIR spectra of empty nanopores.....	118
A1.2	Raman spectra of empty nanopores.....	118
Appendix 2: Supplementary information for WAXS.....		119
A2.1	Equations for lattice interplanar spacing ( $d_{hkl}$ ) calculation.....	119
A2.2	WAXS of untilted and 10-degree tilted polymer-filled O-AAO- 45nm pore samples.....	122





A4.4.2 Electro-polishing the AAO surface.....	136
A4.4.3 Anodization steps of aluminum.....	137
A4.4.4 Fabrication of AAO of thickness less than 40 $\mu\text{m}$ .....	139
A4.4.5 Removal of the aluminum substrate .....	140
A4.4.6 Removal of oxide barrier layer of AAO templates.....	141
A4.5 Solution preparation data for aluminum metal anodization .....	143
Appendix 5: SiO <sub>2</sub> deposition on oxide surfaces .....	146
A5.1 Introduction.....	146
A5.2 Summary of SiO <sub>2</sub> deposition on AAO pore walls by vacuum- pulling method.....	147
Appendix 6: Supplementary figures .....	148
A6.1 Optical picture of the glovebox set-up.....	148
A6.2. Set-up for AC-impedance measurements of AAO templates..	149
Appendix 7: Study of photo-catalysis using titanium dioxide nanotube layers .....	150
Appendix 8: Glossary .....	155

## List of Tables

Table 1.	Common empirical data for oxalic, sulfuric, and phosphoric acid anodization.....	19
Table 2.	Existence of the water and –OH groups after annealing at various temperatures.....	55
Table A1.1.	Molecular vibrational frequencies of Poly(ethylene oxide), (PEO), for mid Infra-Red(IR) region, A and C depicts for amorphous and crystalline phases, and; br-broad, s-small, m-medium, sh-shoulder, vs-very small, w-weak.....	113
Table A1.2.	Molecular vibrational frequencies of Poly(ethylene oxide), (PEO), for FT-Raman (mid IR- region). A and C depicts for amorphous and crystalline phases, and; br-broad, s-small, m-medium, sh-shoulder, vs-very small, w-weak.....	114
Table A1.3.	Molecular vibrational frequencies of PEO:LiTf polymer electrolytes in mid Infra-red(IR) region. A and C depicts for amorphous and crystalline phases, and; br-broad, s-small, m-medium, sh-shoulder, vs-very small, w-weak.....	115
Table A1.4.	Molecular vibrational frequencies of PEO:LiTf polymer electrolytes for FT-Raman ( in mid IR region). A and C depicts for amorphous and crystalline phases, and; br-broad, s-small, m-medium, sh-shoulder, vs-very small, w-weak.....	116
Table A1.5.	Character table for PEO under the factor group $D(4\pi/7)$ .....	117
Table A1.6.	Character table for PEO:LiTf under the factor group $C(2\pi/2)$ .....	117
Table A2.1	d-spacings, reflection angles and intensities of PEO helix-crystal.	123
Table A2.2	d-spacings, reflection angles and intensities of P(EO) <sub>3</sub> :LiTf crystal.....	124
Table A3.1	Parameters and derivations of the electrical properties of materials.....	128
Table A4.1.	Solution data for aluminum and titanium metal anodization.....	145

## List of Figures

Figure 1.1	Schematic for a microscopic view of a rechargeable $\text{Li}^+$ battery cell assembly based on reference [34]. Anode material as graphite (C), cathode material as $\text{Li}_{1-x}\text{Mn}_2\text{O}_4$ , and electrolyte is a lithium based material.....	3
Figure 1.2	Basic Schematic of a fuel cell assemblies. Fuels and oxidants are selected according to the type of electrolyte material. Eg.:(1) Hydrogen fuel and oxygen as oxidant used in proton exchange membrane fuel cell (PEMFC). (2) Methanol and oxygen used in direct methanol fuel cells (MFC).....	4
Figure 1.3	Helix chain length variations with average number weight of poly(ethylene oxide).....	8
Figure 1.4	Percentage crystallinity with average number weight of poly(ethylene oxide).....	9
Figure 1.5	pictorial representations of a 3D spherulite and a lamella. (1, 2, 3 are normal coordinates to the lamella) [46].....	10
Figure 1.6	PEO molecular conformations [47].....	10
Figure 1.7	Crystal structures of planar zig-zag (a) and helix (b) PEO [47]...	11
Figure 1.8	Crystal structure view of PEO:LiTf(3:1) compound through (a b 0) and (a 0 c) planes; shaded atoms indicate $\text{CF}_3\text{SO}_3^-$ ion coordination [48].....	12
Figure 1.9	Phase diagram of the PEO:LiCF <sub>3</sub> SO <sub>3</sub> (X:1) [49]. The labels: “L” stands for liquid, “L+P(EO <sub>3</sub> ·LiCF <sub>3</sub> SO <sub>3</sub> )” for liquid and (3:1) crystal phase, and “PEO+P(EO <sub>3</sub> ·LiCF <sub>3</sub> SO <sub>3</sub> )” for solid phases....	13
Figure 1.10	schematic diagrams for Al anodization. (The beaker of solution is placed in a cooling unit to control its temperature, In general, the cathode is Pt and computer control of the applied current/voltage is optional.....	17
Figure 1.11	schematic plots for current density versus time for Al anodization. Inset shows the various stages of pore growth and indicated on the plot.....	18

Figure 2.1	Vibrational modes of PEO chain atoms.....	24
Figure 2.2	CF <sub>3</sub> SO <sub>3</sub> <sup>-</sup> ion coordination in PEO chain making O:Li(3:1) compound.....	25
Figure 2.3	Schematic representations of crystal ( <i>hkl</i> ) planes and the crystal thickness “ <i>t</i> ” (a), and intensity histogram showing “FWHM” at 2×θ <sub>0</sub> (b).....	27
Figure 2.4	Schematic of a histogram showing the crystalline peaks and amorphous halo of a semi-crystalline material.....	28
Figure 2.5	Schematic of Ewald construction for fiber pattern of monoclinic PEO crystal obtained by rotating the reciprocal lattice around the c-axis.....	30
Figure 2.6	Schematic of an electron probe parameters on a specimen: D <sub>p</sub> - diameter, <i>i<sub>p</sub></i> - current, α <sub>p</sub> - convergence angle, and V <sub>o</sub> - accelerating voltage [113].....	35
Figure 3.1	SEM images of 45 nm pore size AAO anodized in oxalic acid solution (left) and commercially available 200 nm pore size anodisc from Whatman (right). (a), (b) are top surface views, (c), (d) are cross sectional views of the pores and (e), (f) are bottom surface of the AAO templates.....	39
Figure 3.2	Top down, cross-sectional (along the top, middle, and bottom length of the films), and bottom view SEM images of commercially available 60 μm thick Whatman Anodiscs with specified pore diameters of 200 nm, 100 nm, and 20 nm. There is very little change in the average pore diameters of the AAO films looking top down while the non uniformity in the pore channels is evident in the cross-sectional views including a tapering of the pore diameters towards the bottom. The bottom surface of the anodiscs shows the distribution of the surface textured pore diameters to obtain the relevant specified pore sizes.....	40
Figure 3.3	SEM images (top view, 10° tilted top, cross-sectional, 10° tilted bottom, and bottom view) of 100 μm thick O-AAO and S-AAO templates before and after deposition of 1-3 layers of a 2 nm thick SiO <sub>2</sub> chemical deposition.....	43

Figure 3.4	Schematic of apparatus used to pull polymer materials into AAO pores (a) and photograph of the apparatus used to pull the polymer through the AAO pores (b). All the equipment is in a glove box. An image (c) of the as-pulled PEO material in and on the AAO is shown (inset).....46
Figure 4.1	SEM micrographs showing several views of a PEO:LiTf(10:1) filled O-AAO template with 45 nm pores. The negligible thickness of the excess polymer layers on the polymer-filled template should be noted.....49
Figure 4.2	Schematics of the IFS 66v/S IR spectrometer sample compartment and the optical path (from IFS 66v/S IR manual) .....50
Figure 4.3	Custom designed leak tight FTIR sample holder with XY adjusting ability. (a) Full assembled holder, (b) holder parts in apart.....51
Figure 4.4	Schematics of FRA-106 spectrometer sample compartment and optical path (a), and optical picture of the FRA-106 spectrometer and the sample compartment (b).....53
Figure 4.5	Custom designed Raman sample holder with air tight ability. Sample placed on the 200 mm thick ZnSe window. (a) Laser incident side, (b) holder in apart for sample mounting.....53
Figure 4.6	Hygroscopic behavior of PEO and PEO:LiTf; (a) Optical micrograph of a PEO:LiTf (10:1) in O-AAO vacuum pulled outside the glove box showing water accumulation in tens of seconds, (b) Diffractogram of PEO:LiTf(20:1) under inert conditions, (c) (d) PEO:LiTf(20:1) in O-AAO and template showing amorphous structures respectively, (f), (g) Intensity vs. $2\theta$ histograms of previous diffractograms.....56
Figure 4.7	Block diagram for the AC-impedance measurements setup.....57
Figure 4.8	Schematic (left) and optical image of AC-impedance contact probes. The probe contact area is 1.52 mm in diameter, gold coated, and insulated from the heater coils with ceramic.....58
Figure 4.9	A 100 mm PEO:LiTf (10:1) film in the 1.5 mm diameter contact probes (a), PEO:LiTf (10:1) in O-AAO film in the contact probes (b).....59

Figure 4.10	Bulk resistance for different gold contact areas: (a) Measured the same O-AAO-PEO:LiTf (10:1) sample with different contact configurations Top (Bot.) contact $\phi=1.66$ (2.05) mm , (b) Top (Bot.) contact $\phi=1.66$ (3.25) mm, (c) Nyquist plots of AC-impedances of different gold contact configurations measured at 30 °C, 50 °C, 70 °C and 90 °C; closed symbols for Au(1.63mm)/O-AAO45nm-PEO:LiTf(10:1)/Au(2.0mm) and open symbols for Au(1.63mm)/O-AAO45nm-PEO:LiTf(10:1)/Au(3.25mm).....62
Figure 4.11	Schematic diagram for pore dimensions of AAO porosity calculation; circle depicts as pore and hexagonal boundary shows the outer dimension of a single pore.....63
Figure 5.2.1	Nyquist Plots: for AC-impedances in the frequency range 1 kHz - 10 MHz for the bulk PEO:LiTf(10:1) polymer electrolyte for the temperatures 30, 50, 70, and 90 °C, respectively (70 and 90 °C (inset)).....68
Figure 5.2.2	Nyquist plots for AC-impedances in the frequency range 1 kHz -10 MHz for the PEO:LiTf(10:1) polymer electrolyte confined in 30nm (a) and 45nm (b) pores for the temperature range 25 – 90 °C, respectively (70 and 90 °C (inset)).....69
Figure 5.2.3	Arrhenius plots for the bulk and confined PEO:LiTf(10:1) polymer electrolyte. Bulk and confined in 200 (Anodisc), 45, 30, and 18 nm diameter pores. Open symbols are as measured, solid symbols are normalized for template porosity. A table of activation energies is shown inset.....71
Figure 5.2.4	Arrhenius plots for the bulk and confined PEO:LiTf(10:1), PEO:LiTf(30:1) polymer electrolytes in 45 nm pores. Solid symbols are as measured, open symbols are normalized for template porosity.....72
Figure 5.2.5	Conductance per pore vs. pore diameter for: as-prepared AAO (red circles); SiO <sub>2</sub> -coated AAO (blue triangles); and Anodisc (orange diamond) at 30°C. Also plotted are lines for conductance per pore for conductivity typical of solid PEO:LiTf (10:1) at 30 °C (solid line), for conductivity of liquid PEO:LiTf (10:1) extrapolated to 30°C (dashed), and for conduction only for a constant skin depth around the pore perimeter (dotted). Inset shows diagrams and expressions for conductance, $G_A$ and $G_P$ , of a single pore for conduction over the entire cross-sectional area ( $A_A$ ) or a

	skin depth of thickness $t$ ( $A_p$ ), respectively; with pore diameter $d$ , length $l$ , and conductivity $\sigma$ .....	74
Figure 5.3.1	FTIR spectra (4000-1200 $\text{cm}^{-1}$ ) of PEO [A] and PEO:LiTf(10:1) [B] bulk films and confined in: Anodisc (200 nm), 45nm pores O-AAO, 30nm pores S-AAO, 41, 26, 18 nm pores coated with $\text{SiO}_2$ layers on S- and O-AAO pores respectively.....	78
Figure 5.3.2	FTIR spectra (1420-1220 $\text{cm}^{-1}$ ) of PEO [A] and PEO:LiTf(10:1) [B] bulk films and confined in: Anodisc (200 nm), 45nm pores O-AAO, 30nm pores S-AAO, 41, 26, 18 nm pores coated with $\text{SiO}_2$ layers on S- and O-AAO pores respectively.....	81
Figure 5.3.3	Raman spectra in the spectral region (3500-400) $\text{cm}^{-1}$ for PEO [A] and PEO:LiTf(10:1) [B] polymer bulk films and those films confined in 18, 26, 30, 45nm pores.....	83
Figure 5.3.4	Raman spectra in the spectral region (3100-2600) $\text{cm}^{-1}$ for PEO [A] and PEO:LiTf(10:1) polymer bulk films and those films confined in 18, 26, 30, 45nm pores.....	85
Figure 5.3.5	Raman spectra in the spectral region (1420-1220) $\text{cm}^{-1}$ for PEO [A] and PEO:LiTf(10:1) [B] polymer bulk films and those confined in 18, 26, 30, 45nm pores.....	86
Figure 5.3.6	Raman spectra in the spectral region (950-750) $\text{cm}^{-1}$ for PEO [A] and PEO:LiTf(10:1) polymer bulk films and those confined in 18, 26, 30, 41, and 45nm pores.....	88
Figure 5.4.1	WAXS patterns of bulk PEO (a) and PEO:LiTf(10:1) (b).....	89
Figure 5.4.2	Intensity versus $2\theta$ profiles of bulk PEO (green) and PEO:LiTf(10:1) (red).....	90
Figure 5.4.3	Ewald constructions of untilted [E] and $10^\circ$ tilted [F] PEO. Inset figure [A] is showing the PEO crystal looking through the b-axis and inset [B] shows the PEO crystal looking through the c-axis. [C] and [D] show the (120) and ( $hkl$ ) planes in the lattice.....	91
Figure 5.4.4	WAXS of empty pores and bulk PEO and PEO:LiTf a) WAXS pattern of coated and uncoated AAO, as labeled. b) Line profiles from WAXS patterns of various bulk PEO and PEO:LiTf and PEO-filled AAO and empty AAO. c) WAXS patterns for bulk PEO and PEO:LiTf and empty AAO, as labeled.....	92



Figure 5.4.5	WAXS patterns for untilted PEO filled 30 nm pores (a), 10° tilted PEO filled 30 nm pores (b), S-AAO-30nm template (c), Bulk PEO (d).....	94
Figure 5.4.6	WAXS patterns for 10° tilted PEO filled 30 nm pores (top), template (bottom left), and untilted PEO filled 30 nm pores (bottom right) [A]. View of PEO crystal looking through b and c axes [B]. Ewald constructions of untilted [C] and 10° tilted [D] orientations.....	94
Figure 5.4.7	Intensity versus two theta profiles for PEO in 30 nm pores 10° tilted and untilted.....	95
Figure 5.4.8	WAXS patterns for untilted PEO:LiTf(10:1) filled 30 nm pores (a), 10° tilted PEO:LiTf(10:1) filled 30 nm pores (b), S-AAO-30 nm template (c), Bulk PEO:LiTf(10:1) (d).....	97
Figure 5.4.9	(A) WAXS patterns for 10° tilted PEO:LiTf(10:1) filled 30 nm pores (top), template (bottom left),and untilted PEO:LiTf(10:1) filled 30 nm pores (bottom right). Ewald constructions of untilted [C] and 10° tilted [D] orientations.....	97
Figure 5.4.10	Intensity versus two theta profiles for PEO:LiTf (10:1) in 30 nm pores 10° tilted and untilted.....	98
Figure 5.4.11	WAXS patterns of bulk PEO:LiTf and Anodisc-filled PEO:LiTf: [A] WAXS patterns of Anodisc-filled and bulk PEO:LiTf, [B] Line profiles from WAXS patterns of various bulk PEO and PEO:LiTf and PEO-filled AAO and empty AAO, [C] WAXS patterns of bulk PEO:LiTf and anodisc-filled PEO:LiTf at 0° and 10° tilt, as labeled.....	100
Figure A1.1	FTIR spectra (4000-1200 cm <sup>-1</sup> ) of AAO templates: All templates annealed at 1000 °C for 15h in high purity N <sub>2</sub> ; 45 nm pores O-AAO, 30nm pores S-AAO, and 41, 26, and 18 nm pores were obtained by SiO <sub>2</sub> coating on annealed 45 and 30 nm pores respectively.....	118
Figure A1.2	Raman spectra (3500-400 cm <sup>-1</sup> ) of AAO templates: All templates annealed at 1000 °C for 15h in high purity N <sub>2</sub> , 45 nm pores O-AAO, and 30nm pores S-AAO. 41, 26, and 18 nm pores were obtained by SiO <sub>2</sub> coating on annealed 45 and 30 nm pores respectively.....	118

Figure A2.1	WAXS patterns of untilted and 10 degree tilted PEO-filled O-AAO-45nm pore sample.....	122
Figure A2. 2	WAXS patterns of untilted and 10 degree tilted PEO:LiTf(10:1)-filled O-AAO-45nm pore sample.....	122
Figure A2. 3	Mercury 2.4 program interface for crystal structure analysis of PEO and its powder-diffraction pattern analysis.....	125
Figure A2. 4	Mercury 2.4 program interface for crystal structure analysis of P(EO) <sub>3</sub> :LiTf and its powder-diffraction pattern analysis.....	126
Figure A3.1	The vector diagram (left) and sinusoidal waveforms of the current (i) and the voltage (v).....	127
Figure A3.2	Points for a range of frequencies on the Z' axis in the complex impedance plane for an ideal resistor, R.....	129
Figure A3.3	Points for a range of frequencies on the Z'' axis in the complex impedance plane for an ideal capacitor, C.....	130
Figure A3.4	Points for a range of frequencies in the complex impedance plane for combinations of resistors and capacitors in series (a) and parallel (b).....	131
Figure A3.5	AC-impedance spectrums for an electrolyte (solid line) and ideal electrolyte system (dash line) with blocking electrodes.....	133
Figure A4.1	Schematic of a black wax coated aluminum.....	137
Figure A4.2	AAO sample cutting lines for smaller sample sizes. Numbers indicate cutting sequence.....	140
Figure A4.3	Schematic for applying tape window for thick AAO samples when removing the oxide barrier layer.....	143
Figure A5.1	SEM micrographs of AAO pore diameter reduced down to 6nm from 30nm original size by coating SiO <sub>2</sub> layers.....	147
Figure A6.1	Optical picture of the glovebox set-up used in this research work.....	148
Figure A6.2	Set-up used for AC-impedance measurements of PEO:LiTf(X:1) filled AAO templates.....	149

## Abstract

Since their discovery in the 1970s, polymer electrolytes have been actively studied because they have properties important for many device applications. However, even after 40 years, the detailed mechanisms of conductivity in these electrolytes are still not completely understood. Moreover, the conductivity in polymer electrolytes is one of the limiting factors of these devices so that different methods to enhance conductivity are actively being explored. One proposed method of enhancing the conductivity is to confine the polymer electrolyte in the nanoscale, but the study of material properties at the nanoscale is challenging in this area. In this work, we confine poly(ethylene oxide) lithium triflate (PEO:LiTf)(X:1)<sub>X=10,30</sub> polymer electrolytes in carefully fabricated nanometer-diameter anodized aluminum oxide (AAO) pore structures. We demonstrate two orders of magnitude higher conductivity in the confined structures versus that of bulk films. Using x-ray characterization we show that this increased conductivity is associated with ordered PEO polymer chains aligned in the template pore direction. The activation energy of the AAO-confined polymer electrolyte is found to be smaller than that of the unconfined melt and about half that of the unconfined solid. This result indicates that not only is the room-temperature confined polymer ordered, but that this order persists at temperatures where the nano-confined polymer electrolyte is expected to be a liquid.

The geometric bulk resistances of the electrolytes were obtained by AC-impedance spectra, from which the ionic conductivities were calculated. The

Arrhenius plots of temperature dependent ionic conductivities showed that the usual melting temperature of the PEO phase in confined PEO:LiTf(X:1)<sub>X=10,30</sub> is suppressed and a single activation energy was evident throughout the temperature range 25–90 °C.

Wide-angle x-ray scattering (WAXS) patterns show that the polymer chains in both the pure PEO and PEO:LiTf(10:1) electrolyte are aligned along the pore axis and that the structure is ordered in the nano pores. This was based on our observations that the intensity of the PEO crystalline peaks at 19.2° (120) and 23.0° [(hk2) and (hk4)] when the incident x-ray beam was parallel to the pore axes was reduced, but intensity of recovered when the pores were tilted by 10° with respect to the incident x-ray beam.

Exploring the infra-red and Raman vibrational spectra of nano-confined pure PEO and PEO:LiTf(10:1) structures with the bulk films, we found that the IR absorbance bands and the Raman intensities showed a high dichroism to the normal and parallel electric fields of the IR radiation. The parallel band intensity decreased while the normal band intensity increased, consistent with an alignment of the polymer chains along the pore direction.

To perform this research, on our millimeter-sized, hygroscopic samples, substantial changes in the implementation of the characterization techniques such as: AC-impedance spectroscopy, FTIR, Raman-scattering, WAXS, and SEM were required. These changes included: new sample holders to prevent water uptake; a new method to align samples to ensure consistent and reproducible measurements

with the new holder designs; and the development and implementation of an entirely new system for measuring the conductivity versus temperature of our template samples in a glovebox.

The Appendices at the end of this thesis include details of the developed procedures and apparatus, as well as additional experimental results not shown in the thesis.

# Chapter 1: Introduction to Electrochemical Materials

## 1.1 Introduction

With the onset of the climate change due to the increasing use of automobiles, and powered equipment, human society has an ever greater demand for portable energy storage, renewable energy sources and devices such as solid-state batteries, capacitors, fuel cells, solar cells, *etc.* The development and technological applications of these energy sources focus on the performance as well as safety, stability, and the cost. In particular, in energy storage devices, lithium-ion-based energy sources, such as lithium-ion and lithium-polymer rechargeable batteries, have received the most attention because currently they have the highest energy capacities and power densities. On the other hand, polymer electrolytes are emerging as suitable candidates to replace the liquid electrolytes, where their flexible solid forms allow for a variety of micro and macro fabrication architectures and bulk production. Although polymer electrolytes are considered as potential candidates, one major drawback is their low ionic conductivity at ambient temperatures where most domestic energy applications operate. To overcome this problem, investigations of polymer electrolytes have focused on changing the physical and structural properties of the polymers by various methods [1-33]. However, one area that has not been extensively studied is the effect of nanometer spatial confinement on polymer electrolytes. In this research work, lithium salt-dissolved solid poly(ethylene

oxide) polymer electrolytes, [PEO:LiTf(X:1)], are confined in nanopores under well-controlled environment and procedures; and characterized by AC-impedance spectroscopy, wide angle x-ray scattering (WAXS), Fourier transform infra-red spectroscopy (FTIR), Fourier-transform Raman spectroscopy and scanning electron microscopy (SEM).

In the remaining sections of this chapter, under the topic “Electrochemical materials and applications”, electrochemical materials including specific examples are discussed. This section is followed by “Polymer electrolytes” where different polymers, their characteristics and fabrication methods are introduced. In section 1.4, under the topic “Properties of PEO polymer and PEO:LiTf(X:1) electrolytes”, a full description of the Poly(ethylene oxide) polymer, (PEO), and PEO:LiTf(X:1) polymer electrolytes properties and their characterization methods is given in detail. In the last section of this chapter, a general introduction of anodic aluminum oxide (AAO) template fabrication is given.

## **1.2 Electrochemical materials and applications**

Electrochemical materials and their properties have undergone intensive research and development for over a century. Currently, their demand in commercial applications in a variety of physical, chemical, thermal, mechanical and electrical forms is increasing. Most of the demand has focused on energy storage and supply, such as batteries and capacitors, renewable energy, like fuel cells, as well as electrochemical displays and sensors. Figure 1.1 shows a

schematic of a rechargeable  $\text{Li}^+$  battery cell assembly [34]. During a charging cycle of this rechargeable cell,  $\text{Li}^+$ -ions are released from the  $\text{Li}_{1-x}\text{Mn}_2\text{O}_4$  cathode and migrate through the electrolyte to the graphite anode and are stored between graphite layers (intercalated). This ionic migration process is reversed during the discharging cycle with electrons flowing through the load (lamp) and the  $\text{Li}^+$ -ions migrating back to the  $\text{Li}_{1-x}\text{Mn}_2\text{O}_4$  cathode.

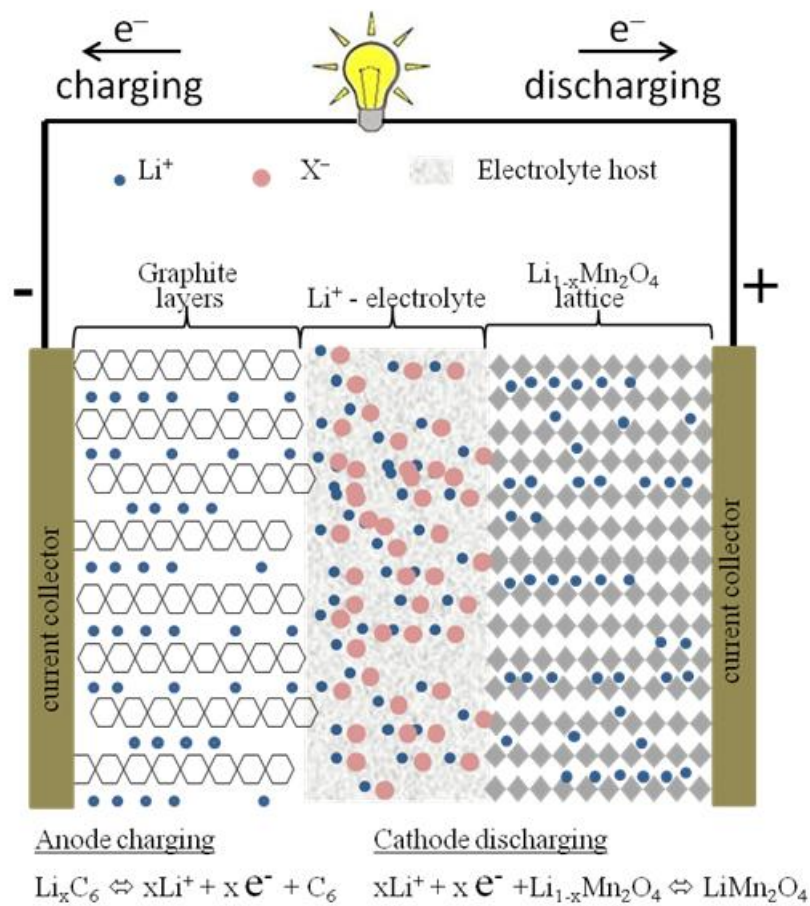


**Figure 1.1** Schematic for a microscopic view of a rechargeable  $\text{Li}^+$  battery cell assembly based on reference [34]. Anode material as graphite (C), cathode material as  $\text{Li}_{1-x}\text{Mn}_2\text{O}_4$ , and electrolyte is a lithium based material.



Figure 1.2 shows a schematic for a generic fuel cell assembly, which in general, are named as the type of electrolyte used to promote the ionic conduction. For example, in a proton conducting fuel cell,  $H^+$  ions are combined with  $O^{2-}$  at the cathode releasing  $H_2O$ . In all fuel cells, fuel and oxidant in the gas state are dissociated into ions using catalytic reactions at the anode and the cathode. Depending on the type of electrolyte, positive ( $H^+$ ) or negative ( $O^{2-}$ ) ions migrate through the electrolyte and react with their ionic counterpart.

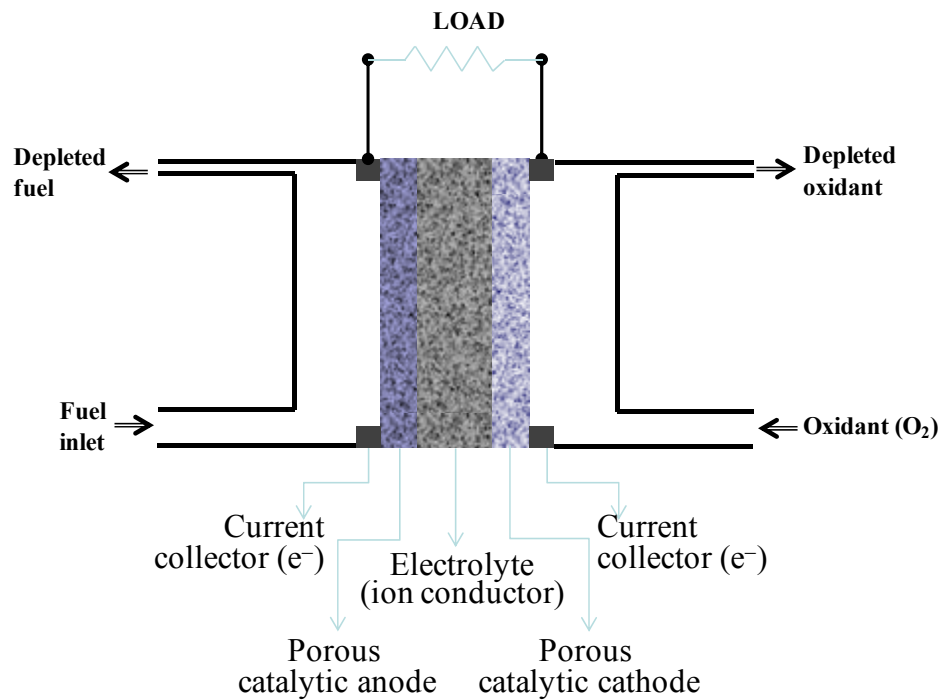


**Figure 1.2** Basic Schematic of a fuel cell assemblies. Fuels and oxidants are selected according to the type of electrolyte material. Eg.:(1) Hydrogen fuel and oxygen as oxidant used in proton exchange membrane fuel cell (PEMFC). (2) Methanol and oxygen used in direct methanol fuel cells (MFC).

For most commercial fuel cell and battery device applications, the device should be portable, efficient at ambient temperatures, durable, and cost effective for mass production. For these purposes, non-volatile solid forms of

electrochemical materials have greater demand as liquid forms are often volatile, have leakage problems, and are difficult to fabricate with, micron-dimensions. Currently, there are a few solid-state materials that are used commercially as electrolytes, such as  $\text{PbF}_2$ ,  $\beta\text{-Al}_2\text{O}_3$ ,  $\text{AgI}$ , and S-glasses. These are useful in ambient temperature applications, such as solid-state batteries and sensors, however, the use of solid-state electrochemical materials in novel technological devices is still not widespread or currently available. One aspect of this research work is to overcome the above application difficulties by implementing nanoscale architecture to enhance the properties of the electrochemical materials.

The fabrication of electrolyte materials in their bulk form has been carried out by numerous methods such as: by chemical means; solvent casting; liquid state mixing; and vapor deposition, etc. Characteristics such as: electrical properties (bulk geometric resistances and ionic conductivities; dielectric relaxations; ionic charge and discharge properties, capacities); molecular vibrations and dynamic motions; molecular and crystal structures; and thermal properties of electrolyte materials, have been widely investigated. The most common characterization methods employed include: cyclic voltammograms; AC-impedance spectroscopy; calorimetric; vibrational spectroscopy; x-rays; scanning electron microscopy (SEM); transmission electron microscopy (TEM); and nuclear magnetic resonance (NMR).

### 1.3 Polymer electrolytes

For portable solid-state electrolyte applications, a recognized advantage is the use of polymers, with polar functional groups. Here polymers are used as solid solvents for various organic and inorganic salts [34-40]. Over the past four decades, many solid-polymer electrolytes, based on different polymers such as: poly(ethylene oxide) (PEO), poly(propylene oxide) (PPO), poly(methyl methacrylate) (PMMA), poly(ethylene imine) (PEI), poly(acrylo nitrile) (PAN), and many others, have been characterized and analyzed. A major challenge is to optimize the electrochemical properties, specifically to obtain high ionic conductivities with strong thermal and structural stability, and mechanical flexibility [34-45]. One of the most investigated groups of polymer electrolyte systems is ionic salts dissolved in (PEO) electrolytes. Among them, lithium-based salts like lithium trifluoromethanesulfonate (LiTf) dissolved in PEO have been extensively investigated and optimized [36, 38-45]. The major unique properties of PEO:Li<sup>+</sup> Y<sup>-</sup>(X:1)electrolytes are their high ionic conductivities and structural stability when compared to the other type of polymer electrolytes. Unfortunately, at ambient temperatures, PEO<sub>n</sub>:(Li<sup>+</sup> CF<sub>3</sub>SO<sub>3</sub><sup>-</sup>) electrolytes show ionic conductivity in the range (10<sup>-6</sup>-10<sup>-8</sup>) S cm<sup>-1</sup> which is still not a good enough for commercial applications, which requires conductivities >10<sup>-2</sup> S cm<sup>-1</sup>. To obtain higher ionic conductivities at ambient temperatures, polymer electrolytes have been modified using the various methods listed below:

- [1] Addition of low molecular weight PEO or another polymer as a binder [1,2];
- [2] Incorporation of plasticizers [1-3];
- [3] Addition of inert oxide materials (composite polymer electrolytes) [4-11];
- [4] Addition of clay or dye materials [12];
- [5] Application of compression or stretch [13,14];
- [6] Different thermal treatments like annealing [15,16];
- [7] Magnetically orienting polymer electrolytes [17,18];
- [8] Unusual crystalline polymer electrolytes [19,24]; and
- [9] Confinement to nanometer dimensions [25-33].

In the above methods, for initial polymer electrolyte fabrication, the solvent casting synthesis process is typically used. The polymer-electrolyte complexes are prepared by mixing appropriate proportions of polymer, salt, and other additional compounds in an anhydrous solvent, such as acetonitrile, and casting on a suitable non-adhesive substrate, like poly(tetrafluoroethylene) (PTFE), to obtain an electrolyte film. The solvent evaporates in a chemically inert atmosphere followed by a vacuum drying process, as necessary.

While some polymers in nanoscale domains have been investigated by several research groups [37-45]. They have not been systematically explored in careful manner, In this work, the effects of low molecular weight poly(ethylene oxide) (PEO,  $M_w=3,400$  g/mol) polymer and PEO:LiTf(X:1) polymer electrolytes confined in nanometer-sized pores are analyzed in detail, and the mechanism for

the dramatic ionic conductivity enhancement of these materials confined in the nano-pores at ambient temperatures is investigated.

#### 1.4 Properties of PEO polymer and PEO:LiTf(X:1) electrolytes

Poly(ethylene oxide) is made of repeating ethylene oxide monomer units, - $[\text{C}_2\text{H}_4\text{O}]_n$ . The mean molecular weight and the chain lengths are modified by changing the polymerization conditions. The physical properties, such as thermal transitions, dielectric properties, crystallinity and viscosity, *etc.* are dependent on the molecular weight of the polymer. Estimated chain length versus molecular mass obtained from the bond lengths and atomic masses is shown in figure 1.3.

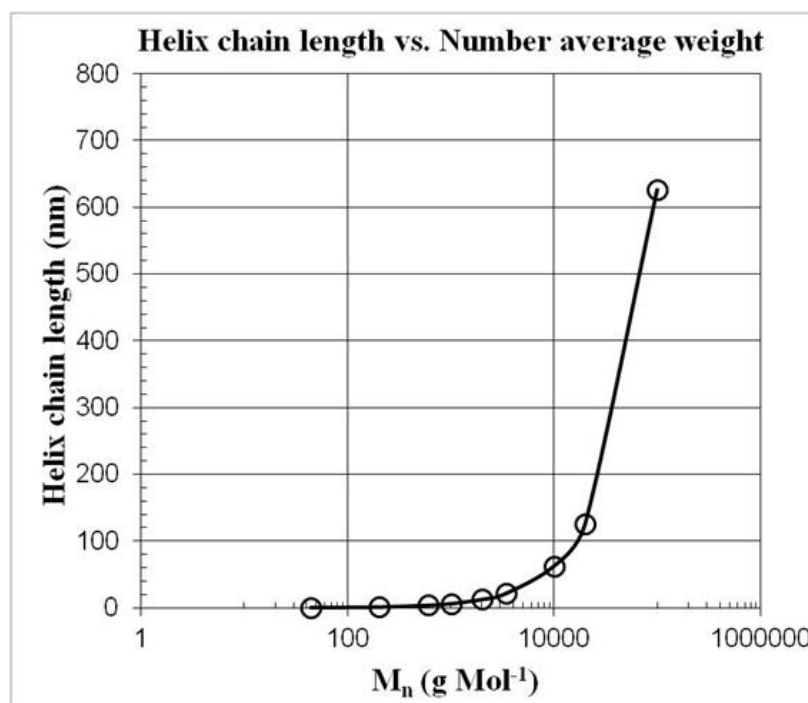
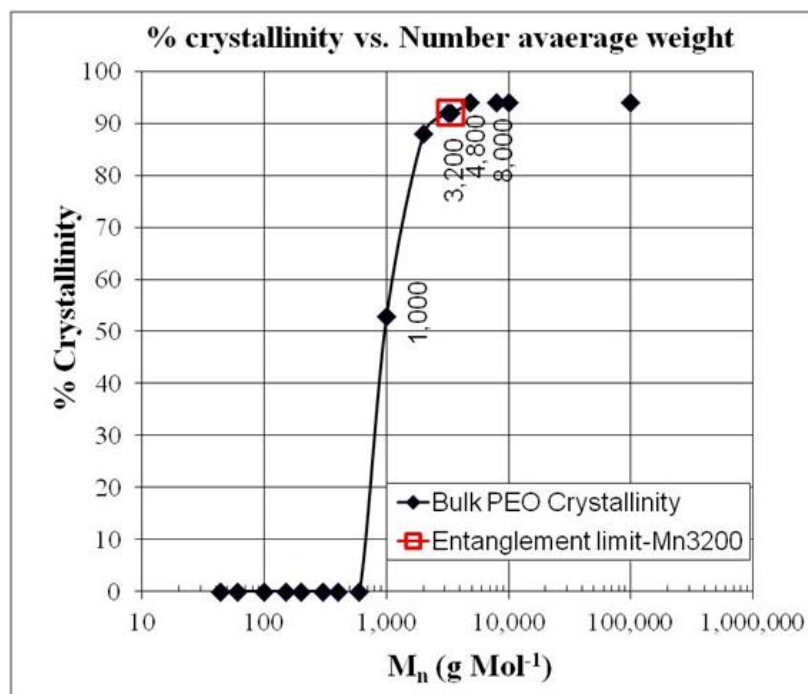
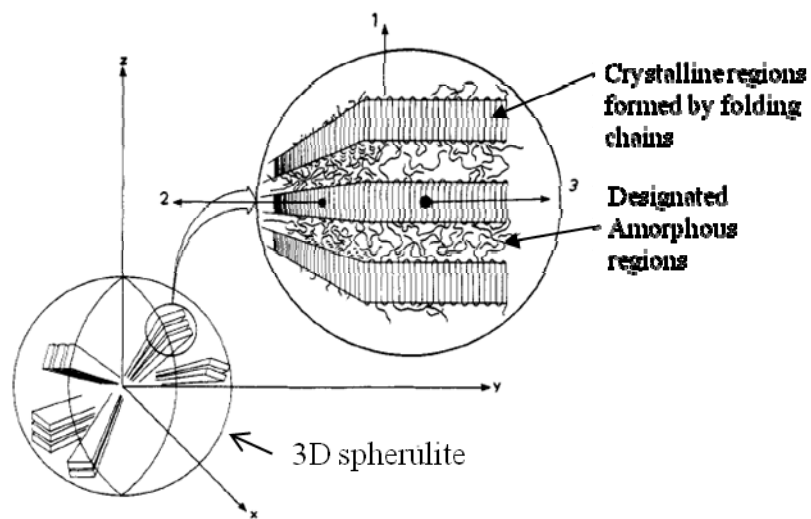


Figure 1.3 Helix chain length variations with average number weight of poly(ethylene oxide).



**Figure 1.4** Percentage crystallinity with average number weight of poly(ethylene oxide).

The change in the percentage of crystallinity as a function of the molecular mass of PEO is shown in figure 1.4. While the low molecular weight PEO polymers ( $< 800 \text{ g mol}^{-1}$ ) are liquid, PEO polymers with weights between  $800\text{-}1500 \text{ g mol}^{-1}$  are waxy and higher molecular weight PEO polymers are solid. Around  $M_n = 3200 \text{ g mol}^{-1}$ , the polymer molecules are long enough to entangle with each other, while some of the chain segments are unwound to make crystalline and amorphous phases. When the chain lengths become longer than the entanglement limit, polymer chain orientations become highly complex and the degree of crystallinity reaches a maximum, independent of the chain length. A sketch of the bulk crystalline lamellae structure in a polymer film is shown in figure 1.5 [46].



**Figure 1.5** Pictorial representations of a 3D spherulite and a lamella. (1, 2, 3 are normal coordinates to the lamella) [46].

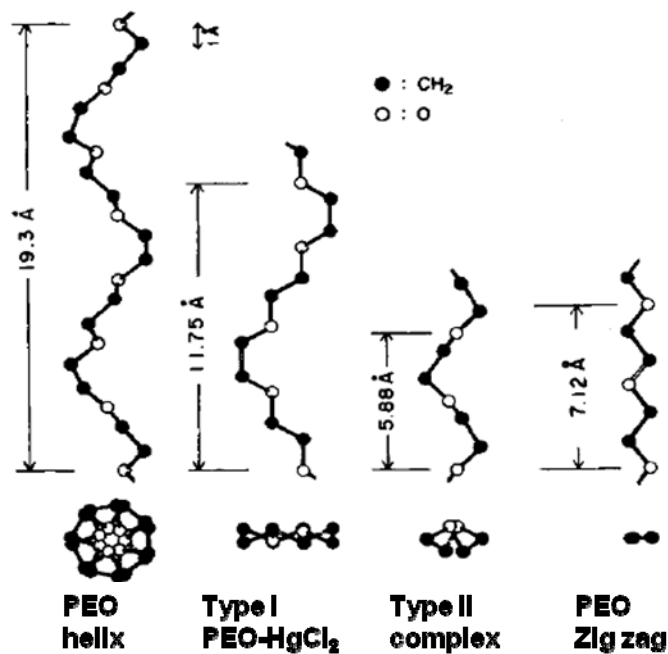


**Figure 1.6** PEO molecular conformations [47].

From the early studies of PEO molecular structure, it has been established that different forms of chain conformations in space can exist as shown in figure 1.6 [47]. A helix chain conformation is made of two helices having seven ethylene monomer units for each unit. A single helix crystalline lattice has a monoclinic crystal lattice with  $a = 8.05 \text{ \AA}$ ,  $b = 13.04 \text{ \AA}$ ,  $c = 19.48 \text{ \AA}$  and [the angle  $\beta_{ac}$  is  $125.4^\circ$ ]. Crystal structures of PEO with different conformations are shown in figure 1.7 [47].

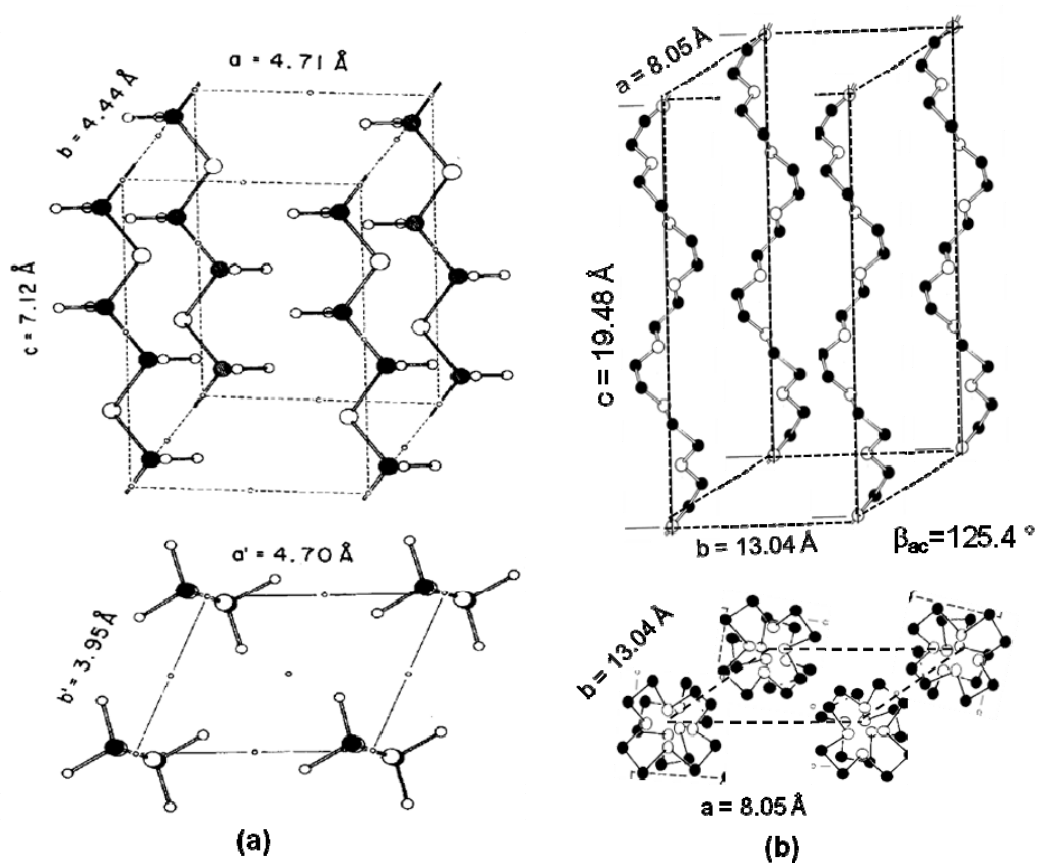


**Figure 1.7** Crystal structures of planar zig-zag (a) and helix (b) PEO [47].



The structural conformations and the properties of polymers are more complicated when an organic or inorganic salt is mixed with it. As an example, LiTf salt dissolved in PEO makes a crystal phase of O:Li(3:1) composition as shown in figure 1.8 [48]. In addition to O:Li(3:1) crystallites, pure PEO helix crystals along with amorphous PEO and PEO:LiTf phases are also present in a bulk film.

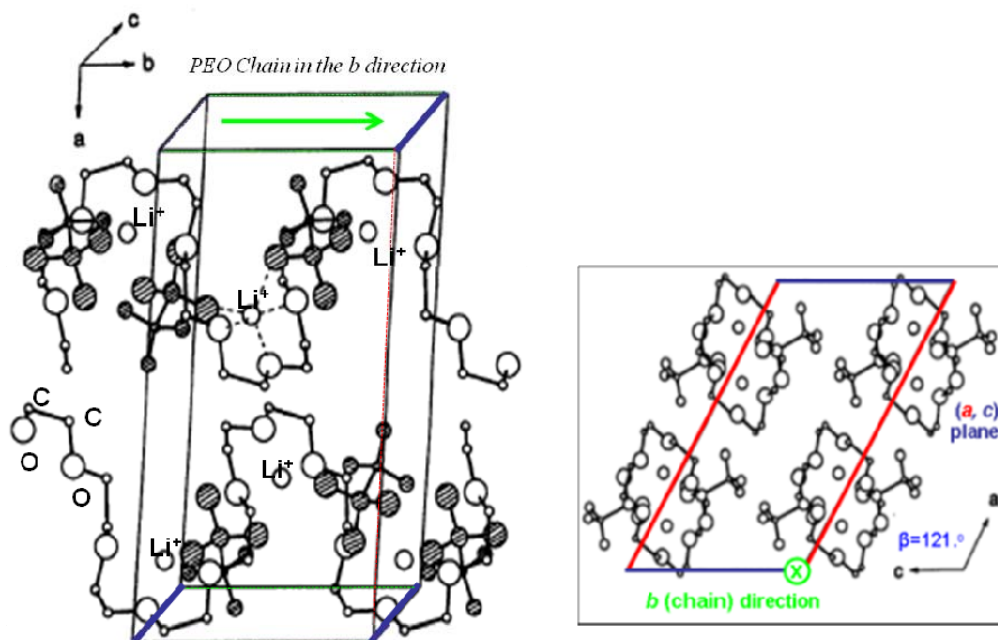


**Figure 1.8** Crystal structure view of PEO:LiTf(3:1) compound through (a b 0) and (a 0 c) planes; shaded atoms indicate  $\text{CF}_3\text{SO}_3^-$  ion coordination [48].

As shown in figure 1.8, a 3:1 phase lithium-ion is coordinated with five oxygen atoms, three consecutive oxygen atoms (3:1) from a PEO chain and other two from two  $\text{CF}_3\text{SO}_3^-$  anions which reside outside the chain.

The O:Li(3:1) crystal unit cell is monoclinic with  $a = 16.77 \text{ \AA}$ ,  $b = 8.61 \text{ \AA}$ ,  $c = 10.07 \text{ \AA}$  and  $\beta_{ac} = 121.02^\circ$ . As indicated, the multi-phase PEO:LiTf(X:1) structure gives rise to major changes in the physical properties in bulk systems and when it is confined in a nanoscale domain. The behavior of the physical states of the PEO:LiTf(X:1) structures are shown by the phase diagram, figure 1.9 [49], which relates the thermal properties against the mass ratio of the PEO and LiTf.

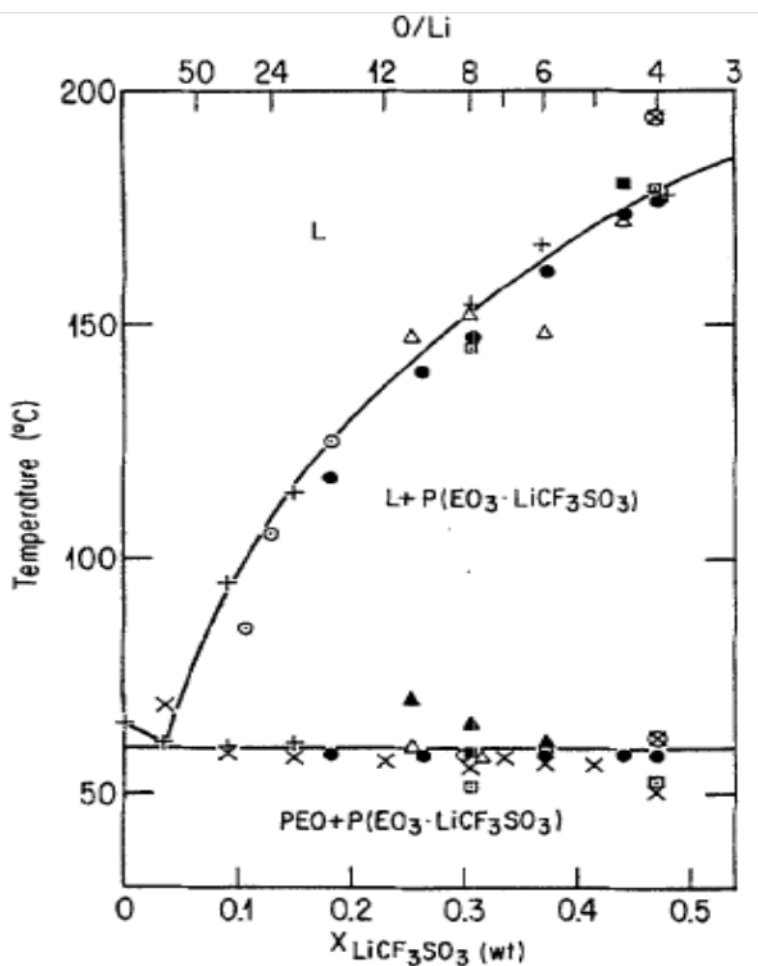


**Figure 1.9** Phase diagram of the PEO:LiCF<sub>3</sub>SO<sub>3</sub>(X:1) [49]. The labels: “L” stands for liquid, “L+P(EO<sub>3</sub>·LiCF<sub>3</sub>SO<sub>3</sub>)” for liquid and (3:1) crystal phase, and “PEO+P(EO<sub>3</sub>·LiCF<sub>3</sub>SO<sub>3</sub>)” for solid phases.

The investigation of ionic conductivity in polymer electrolyte complexes show that the ionic transport occurs in the liquid or solid amorphous phase, while there is no strong evidence supporting a contribution from the crystalline domains like O:L(3:1) compounds in PEO:LiTf(X:1) systems.

In this work, the molecular bonds vibrational studies of PEO polymer and PEO:LiTf(X:1) complexes confined in 18, 22, 26, 30, 40, 45 nm diameter AAO pores and 200 nm diameter anodisc<sup>TM</sup> are characterized in a controlled manner by Fourier-transformed infra-red red (FTIR) and Raman scattering spectra and the structural properties are characterized by wide angle x-ray scattering (WAXS). In addition, the electrical properties are investigated by AC-impedance measurements and the morphology of the polymer systems in nanopores is studied by the scanning electron microscopy (SEM).

### **1.5 Anodized aluminum oxide (AAO) and applications**

Electrolytically grown non-porous alumina films and porous templates on various substrates have been used for over a century. Most of the conventional commercial applications are protective oxide coatings, dielectric capacitors and decorations. The first observations and detailed understanding of the properties of porous anodized aluminum oxide (AAO) were reported by Edward and Keller in 1941 [50]. Their pioneering work on porous oxide growth on an aluminum surface led to the future modeling of AAO pore growth mechanisms[50-53]. Other researchers over the decades have further investigated the mechanism of the

growth and technical aspects for fabrication of AAO and the anodization of other metals. [54-62].

In 1995, a structural replication process for the fabrication of well-ordered high aspect ratio anodic alumina templates was introduced with two anodization steps [63]. The long-term first anodization is carried out under specific conditions that initiate an oxide layer with a non-organized pore structure that transforms into a close-packed, well-ordered array of pores with time. This oxide surface is stripped off leaving behind well-ordered nanoscale dimples from the pore bottoms on the aluminum surface. The second anodization initiates its pore growth at these pore bottoms and thus starts and maintains the growth of well-ordered pores. This two-step replication process gives a method for well-ordered pore growth which has led to new fabrication techniques for a variety of nano structures as well as new theoretical models for nanopore growth.

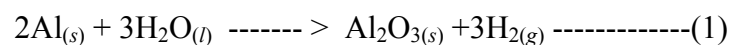
The demand for high aspect ratio nano-pore structures with chemically inert surfaces for both scientific research and commercial applications has led to further developments and new fabrication techniques. By controlling the anodizing conditions and the anodization steps, several research groups have succeeded in fabricating well-ordered AAO templates with control over the pore size, the pore structural shapes, patterning, as well as thickness of the film. All of these fabrication methods are achieved by pre-indenting the aluminum surface as introduced in the two-step replication method. The most widely used surface pre-indenting methods are electrochemical, electrical and mechanical, where the final

goal is to develop the simplest techniques which meet commercial demand on AAO templates with their own integrity. Electrochemical surface pre-indenting methods, make use of electrolytes, mostly diluted acids like sulfuric, oxalic, or phosphoric. For the electrical field approach, control of the applied electric fields and current densities is important and SiC molds, hard polymeric nano beads, and atomic force microscopy tips are used for mechanical pre-indentation [46,47,50,63-70].

Well-ordered, high aspect ratio, and high pore density AAO templates have been introduced in many applications such as the fabrication of semiconductor structures [71], nano-capacitors [72], nano-magnetism [73], nano-fluidics[74, 75], for biological molecules separation, storage and delivery [75, 76], nano-dots, wires, hollow tubes [77, 82], lithographic masks [84], sensors [85], nano-fuel cells and batteries [86-88].

### 1.5.1 Introduction to AAO template fabrication

The general chemical reaction of electrically anodized aluminum oxide, AAO, takes place as shown in the chemical formula (1) [53].



where  $\text{Al}_2\text{O}_3$  formation takes place at the anode surface which in this case is the Al metal while the platinum acts as the cathode, discharging electrons to form  $\text{H}_2_{(g)}$ . A schematic diagram for the experimental setup is shown in figure 1.10.

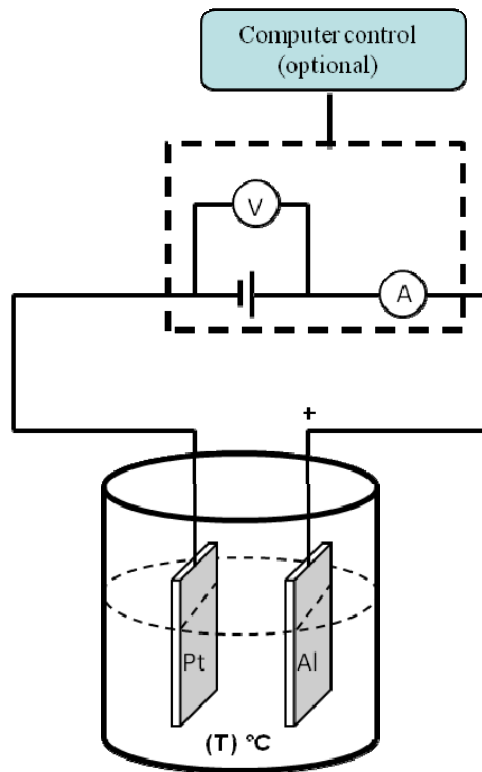


**Figure 1.10** Schematic diagram for Al anodization. (The beaker of solution is placed in a cooling unit to control its temperature, In general, the cathode is Pt and computer control of the applied current/voltage is optional.

During the anodization process, the formation and deposition of alumina on the aluminum surface can take place as barrier type or porous type films. When the aluminum metal is anodized in an electrolyte solution of  $5 < \text{pH} < 7$  and the applied DC-current density is constant, the deposited alumina is a barrier type film. Porous type alumina films are deposited when oxide dissolving diluted acidic electrolytes and constant electric fields are used for a period of time. The anodization temperature of both barrier and porous type alumina is also a factor in the oxide growth rate. For the purpose of this thesis, only porous type AAO fabrication was used.

### 1.5.2 AAO pore growth mechanism

Two simultaneous processes occur during the alumina anodization. First, when an electric field is applied between the anode (aluminum) and cathode (platinum), a barrier type oxide layer is formed on the Al surface. This phenomenon is called field-assisted oxidation and continues until the electric current density reaches its minimum value. A typical experimentally observed oxide growth plot of current density versus time is shown in figure 1.11. Second, at the minimum current density, the grown oxide layer starts to dissolve into the electrolyte.

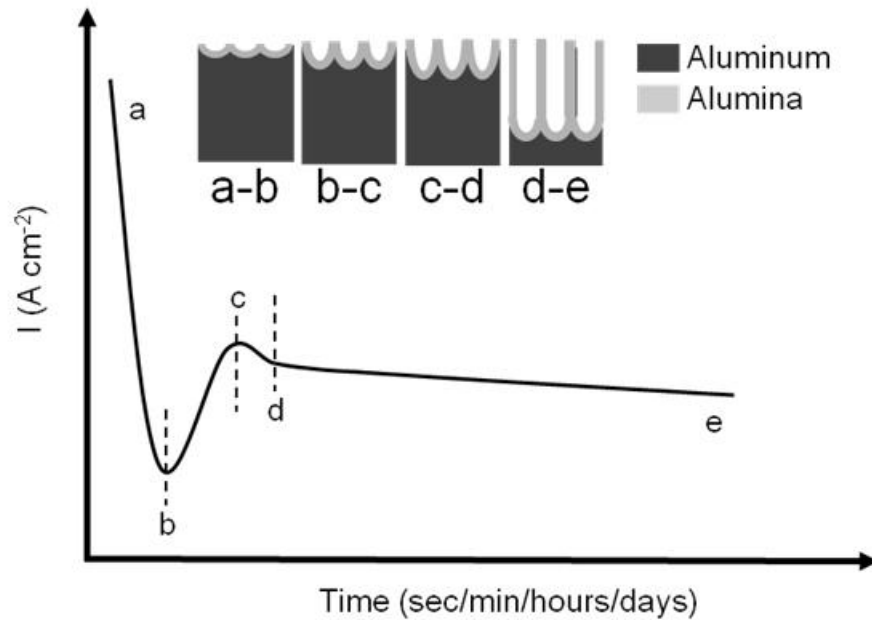


**Figure 1.11** Schematic plot for current density versus time for Al anodization. Inset shows the various stages of pore growth and indicated on the plot.

This field-assisted dissolution of oxide occurs anisotropically towards the Al surface while initiating the pore bases and keeping the shortest distance for anionic carriers to reach the aluminum surface and continue further oxidation. In figure 1.11, during period (b)-(c), field assisted dissolution takes place while the oxide growth rate increases. At time (c) the oxide dissolving power increases slightly compared to the oxidation rate and continues until time (d). From time (d) on, the oxidization and the dissolution rate are at equilibrium, and the current remains constant until the entire Al atoms are oxidized or the electrical field is broken down. The inset pictures show the AAO pore growth on the aluminum surface at different stages in time. In practical approaches of AAO fabrication, it is observed that the typical current density versus time curves take the same shape but the time intervals of different features vary. This indicates that the pore diameter and pore density are dependent on the applied field strength as well as the pH, type and temperature of electrolyte. It is also observed that the condition for good pore ordering in a particular electrolyte solution occurs at a particular applied electric field. Common examples are shown in table 1.

**Table 1.** Common empirical data for oxalic, sulfuric, and phosphoric acid anodization.

Electrolyte	Concentration	DC voltage	Pore diameter (T<40um)	Inter-pore distance
Oxalic	0.3 M	40	30-33	100-105
Sulfuric	0.3M	26	19-20	60-65
Phosphoric	0.3 M	195	100-120	500
Phosphoric	10 wt%	160	150-220	420



Empirically, the center-to-center inter pore-distance of well-ordered AAO structures,  $D_{pp}$ , has been observed to be a function of the applied potential,  $U$ , with a growth rate factor of  $\sim 2.5$  nm/V. The relation is given by equation (2) [57, 58].

$$D_{pp} = k \cdot U \text{ -----(2)}$$

The volume of the pores can be enlarged by chemically etching the pore wall material. The material etches anisotropically while the pore diameter is widened isotropically through the pore channel. On the other hand, the pore volume can also be reduced by depositing layers of suitable organic or inorganic materials on the wall surface such as a coating of  $Al_2O_3$  or  $SiO_2$  layers on the pore surface. See appendix 5 for the  $SiO_2$  coating method used in this work.

## **1.6 Introduction to next chapters**

The following outlines the rest of this thesis. Chapter 2 describes the various material characterization techniques used in completing this work. This includes: molecular vibration studies by FTIR and Raman spectroscopy; explanation of structural properties by WAXS; measurements of electrical properties by AC-impedance spectroscopy; and study of surface morphology by SEM.

Chapter 3 explains the details of the experimental methods used in this research work including: the fabrication of anodic alumina templates; preparation of bulk PEO and PEO:LiTf(X:1) films; the method of inserting polymer materials

into the nanopores by vacuum pulling; as well as a method for removing excess polymer material from the top and bottom of the pulled nanopore templates.

In chapter 4, the instruments and techniques for the characterization of PEO polymer and PEO:LiTf-filled AAO are discussed.

Chapter 5 presents the results and discussion of this research work. In the first part of this chapter, the AC-impedance spectra and ionic transport properties of the PEO:LiTf(X:1)<sub>X=10,30</sub> bulk samples and the confined PEO:LiTf(X:1)<sub>X=10,30</sub> nanopore samples are discussed. For the vibrational spectra, peak intensity reduction or vanishing, and peak shifting are discussed with appropriate transition mode assignments in separate spectral regions. Finally, the WAXS patterns of the of PEO, PEO:LiTf(10:1) confined in nanopore samples are compared to the bulk samples and the crystal structural changes of the PEO and PEO, PEO:LiTf(3:1) are discussed. In the end of this chapter, a summary is given for all the results obtained to explain the enhancement of ionic conductivity in a nanopore scale.

## **1.7 Introduction to appendices**

In appendix 1, table A1 and table A2 illustrate molecular vibrational frequencies of Poly(ethylene oxide), (PEO), and PEO:LiTf(X:1) polymer electrolytes in mid infra-red(IR) region in which IR and Raman spectra are shown in the left and right panels respectively. In table A3, the character table for PEO under the factor group  $D(4\pi/7)$  is shown. FTIR and Raman spectra for empty AAO samples are shown in figures A1.1 and A1.2

In appendix 2, the equations for lattice interplanar spacing  $d_{hkl}$  calculation and d-spacings for PEO and P(EO)<sub>3</sub>:LiTf crystals are shown. WAXS patterns of untilted and 10 degree tilted polymer-filled O-AAO-45nm pore samples are shown in this appendix. At the end of this appendix, the Mercury 2.4 computer program output for the above crystals is also shown.

In appendix 3, a brief introduction to AC-impedance measurement technique is given, which explains how to obtain geometric bulk resistance of an electrolyte system

In appendices 4 and 5, chemical information, sample cleaning procedures, detailed steps of the fabrication of AAO, and SiO<sub>2</sub> layers coating on AAO pore walls are explained. A picture of the glovebox used in this research work and complementary picture of the conductivity measuring setup are shown in appendix 6.

Appendix 7 is includes a published paper under the topic “Study of photocatalysis using titanium dioxide nanotube layers” which includes work done in addition to the research on AAO.

## Chapter 2: Introduction to Materials Characteristic Properties

### 2.1 Introduction

Electrochemical materials have characteristics, which are governed by their chemical, physical, structural and electrical properties. In this chapter, I briefly describe the background material for: characteristics of molecular vibrational energies via vibrational spectroscopy; structural properties, such as crystal size and degree of percentage of crystallinity by x-ray analysis; ionic transport by electrical measurements; and surface morphology by SEM.

### 2.2 Molecular vibrations and vibrational spectra

In general, the total energy of a molecule can be broken up into several different modes, as shown in equation (3). For a molecule, all of these energy modes can be changed through interactions (absorption or emission) with electromagnetic radiation of different energy (wavelengths). Energies associated with the transition of electrons between molecular levels require ultra-violet (UV) or visible light and energies associated with the vibration of molecular bonds lie in the infra-red spectral (IR) range. Molecules rotational transitions occur in the microwave range, while translational transitions occur in the radio frequency (RF) range.

$$E_{\text{total}} = E_{\text{electronic}} + E_{\text{vibrational}} + E_{\text{rotational}} + E_{\text{translational}} \text{ -----(3)}$$

The normal vibrational modes of poly(ethylene oxide) polymer molecules can be described by the changes in the characteristic chemical bond lengths and angles of its simple constituent monomer, caused by environmental perturbations and can be observed in IR spectral features. The perturbations of the resonance vibrations of a pair or group of atoms, in a polymer give rise to changes in their dipole moments and their polarizability. In this work, the influence of nanometer confinement on the molecular vibrational modes of stretching ( $\nu$ ), rocking ( $\rho$ ), wagging ( $\omega$ ), twisting ( $\tau$ ), and bending ( $\delta$ ) of PEO polymer and PEO:LiTf(10:1) electrolytes are investigated. Diagrams illustrating the normal molecular vibrations of PEO, are shown in figure2.1.

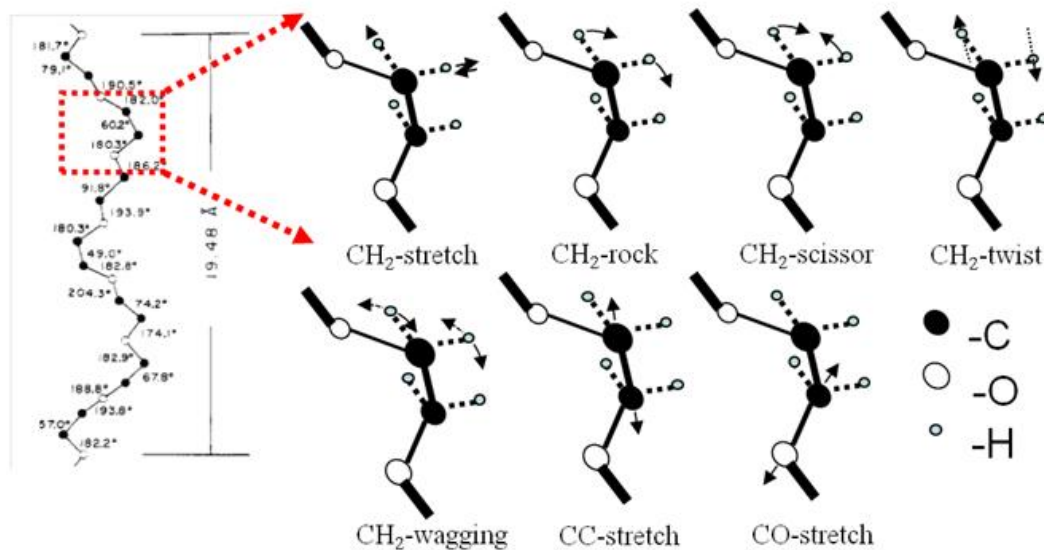


**Figure 2.1** Vibrational modes of PEO chain atoms.

Figure 2.2 shows the triflate-ion conformation in an PEO:LiTf (3:1) compound. As shown in the figure, a lithium ion is coordinated with five oxygen atoms; three consecutive oxygen atoms (3:1) from the PEO chain and two from the two  $\text{CF}_3\text{SO}_3^-$  anions from outside and opposite to the chain.

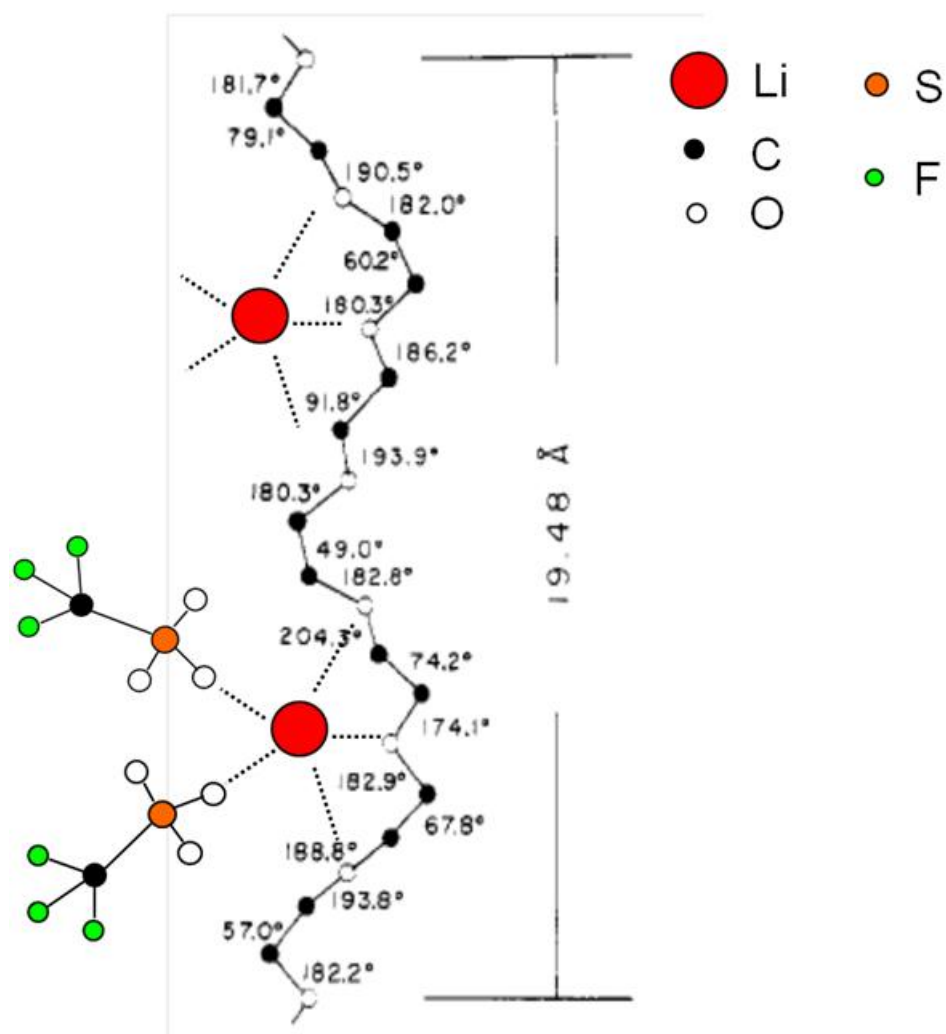


**Figure 2.2**  $\text{CF}_3\text{SO}_3^-$  ion coordination in PEO chain making O:Li(3:1) compound.

The tables A1.1 and A1.2 (Appendix-1) tabulates vibrational frequencies for different IR and Raman modes of PEO molecules. The tables A1.3 and A1.4

(Appendix-1) tabulates the IR and Raman modes of PEO:LiTf(X:1) electrolytes respectively [89-104].

In the analysis of bulk versus nano-confined polymer systems, changes in spectral features are investigated. Specifically, intensities, positions, widths and shapes of absorption peaks in IR spectra, or emission peaks in Raman scattering spectra are used to investigate the effect of nanometer-scale confinement on PEO polymer and PEO:LiTf polymer electrolytes.

### **2.3 X-ray scattering and materials physical properties**

The study of x-ray diffraction and scattering from polymers and other materials is a fundamental and well-established non-destructive technique. The characterization of: crystal formation; structural geometry and crystal spatial orientation; and the degree of crystallinity against the amorphous counterparts are some of the important properties of a polymer material. In the characterization of polymer materials, wide-angle x-ray scattering (WAXS) and small-angle x-ray scattering (SAXS) techniques are widely used to determine these properties. In SAXS, x-ray scattering angles from  $1-5^\circ$  are measured, while in WAXS scattering angles from  $5-180^\circ$  are measured. In practice, most wide-angle diffraction peaks for polymer materials lies within an angular range of  $5-90^\circ$ .

WAXS diffraction information is displayed by two methods. One is the photographic image of the diffracted X-ray pattern (diffractogram) and the other

is the diffraction histogram, which plots the diffracted x-ray intensity against the scattered or diffracted angle,  $2\theta$  [105].

### 2.3.1 Estimation of crystal size

In a mixture of crystallites, the crystal size can be estimated by the well-known Scherrer formula, equation (4).

$$t_{hkl} = k \lambda / \beta \cos(\theta_o) \text{ -----(4)}$$

Figure 2.3(a) shows the relationship between the crystal thicknesses, “ $t_{hkl}$ ”, with several layers of parallel lattice planes ( $hkl$ ) and figure 2.3(b) shows the corresponding intensity vs.  $2\theta$  histogram. In the Scherrer formula,  $\lambda$  is the x-ray wavelength,  $\theta$  is one half of the angle between the incident and diffracted beam from the ( $hkl$ ) planes,  $\beta$  is the full width half maximum (FWHM) of the peak at  $2\theta$  in the histogram as shown in figure 2.3(b), and  $k$  is an empirical constant with a value of  $\sim 0.9$  [105].

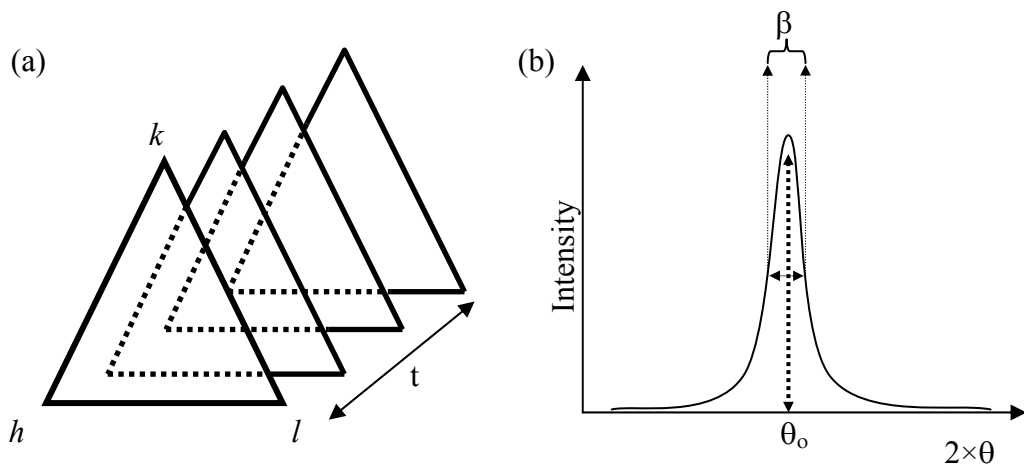


**Figure 2.3** Schematic representations of crystal ( $hkl$ ) planes and the crystal thickness “ $t$ ” (a), and intensity histogram showing “FWHM” at  $2\times\theta_o$  (b).



### 2.3.2 Determination of degree of crystallinity

One important property of x-rays is that they diffract from crystalline phases and scatter from amorphous phases of the material. This characteristic property is used as a means to measure the amount of crystalline versus amorphous phases in a material. In a diffraction pattern, the crystalline phases give rise to sharp peaks (spots) or if it is polycrystalline, sharp concentric rings, while amorphous phase gives rise to a diffuse (broad) concentric halo. Figure 2.4 is a schematic of a histogram for a semi-crystalline material composed of crystalline and amorphous phases. The two peaks are due to the diffraction from two different crystal planes in the crystalline phase and the broken line indicates the diffuse halo arising from the amorphous phase.

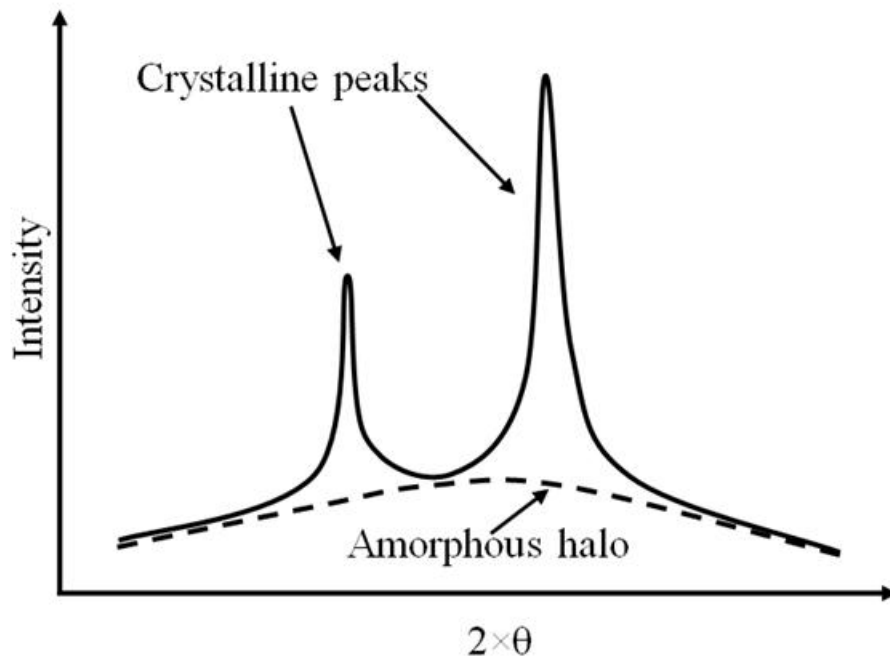


**Figure 2.4** Schematic of a histogram showing the crystalline peaks and amorphous halo of a semi-crystalline material.

If  $I_c(\rho)$  is the intensity of the x-rays diffracted from the crystalline phase and  $I(\rho)$  is the total diffracted and scattered x-ray intensity from the specimen, the ratio of the integrated intensity of  $I_c(\rho)$  over the reciprocal lattice space ( $\rho_{hkl}$ ) to the total integrated intensity is defined as the degree of crystallinity ( $\chi_c$ ). The  $\chi_c$  in equation (5) is shown without taking into account the atomic perfection factors [105].

$$X_c = \frac{\int_0^\infty |\rho^2| I_c(\rho) d\rho}{\int_0^\infty |\rho^2| I(\rho) d\rho} \text{-----(5)}$$

### 2.3.3 PEO crystal structure and fiber patterns

In this work, WAXS is used to study the effect of nanometer confinement on the structure of PEO and PEO:LiTf polymer materials. For the monoclinic crystalline structure of PEO (inset in figure 2.5), the fiber WAXS pattern is constructed by rotating the reciprocal lattice about the fiber-axis (in this case the c-axis), as shown in figure 2.5 [106]. For the calculation of reciprocal space lattice coordinates, the real crystal dimensions of  $a = 8.05 \text{ \AA}$ ,  $b = 13.04 \text{ \AA}$ ,  $c = 19.48 \text{ \AA}$  and  $\beta_{ac} = 125.4^\circ$  were used and the interplanar spacings,  $d_{hkl}$ , are calculated for a monoclinic system [47-49, 89-104]. See appendix-2 for equations for d-spacings.

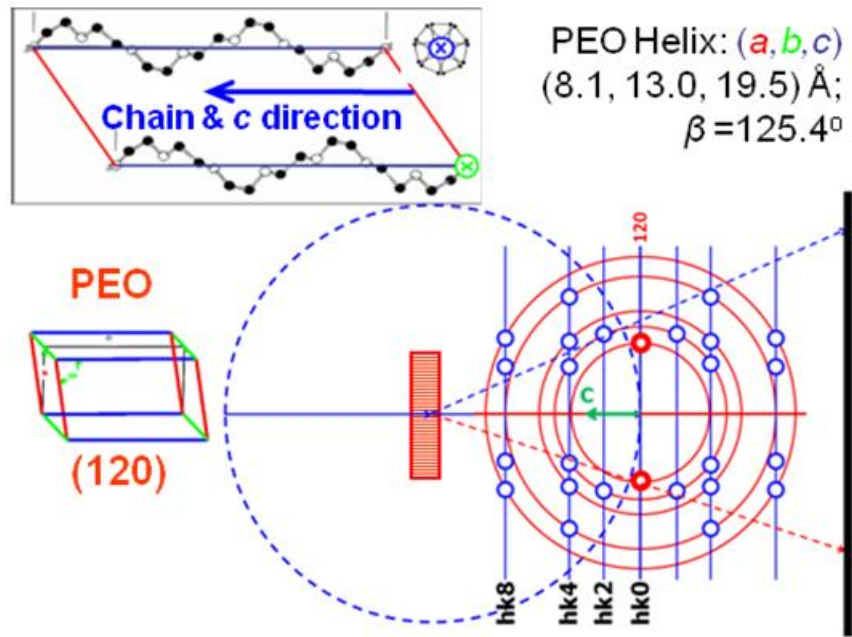


**Figure 2.5** Schematic of Ewald construction for fiber pattern of monoclinic PEO crystal obtained by rotating the reciprocal lattice around the c-axis.

## 2.4 Ionic transport in materials

The microscopic description of ionic conductivity in a material is given by equation (6).

$$\sigma = \sum n_i (z_i e) \mu_i \quad \text{-----(6)}$$

Where  $n_i$  – number of  $i^{\text{th}}$  ionic species per volume

$z_i$  – valance number of  $i^{\text{th}}$  ionic species

$\mu_i$  – mobility of  $i^{\text{th}}$  ionic species

This equation does not show the direct representation of the temperature dependency of the ionic conductivity in a material. However, there are several empirically formulated equations for the temperature dependent ionic conductivities of different types and phases of electrolyte materials. Among

them, the Arrhenius, Vogel-Tamman-Fulcher (VTF), and Willams-Landel-Ferry (WLF) equations are common for representing the mechanisms of ionic conductivities in materials. They were derived by taking into account the different intrinsic properties of the materials [107-113].

#### 2.4.1 Arrhenius equation

This equation for ionic conductivity measurements is formulated by taking into account the ions hopping from a higher energy state (occupied) to a lower energy state (vacancy) in crystalline, semi-crystalline and solid amorphous phases such as glass-like materials. According to this mechanism, the log of the ionic conductivity behaves linearly with temperature for a given solid phase of a material. The Arrhenius equation is shown in equation (7) [108].

$$\sigma = \sigma_0 \exp[-E_a/kT] \text{-----}(7)$$

where,  $\sigma_0 = (1/3kT) (ze)^2 n a_0^2 v_0$

$z$ =valance number of the ionic species

$e$ =electron charge

$n$ =mobile ionic concentration

$a_0$ =least hopping distance

$v_0$ = ion oscillation frequency

$k$ =Boltzmann constant

$E_a$ =activation energy

#### 2.4.2 Vogel-Tamman-Fulcher (VTF) equation

Electrolytes, which show liquid-like mechanical properties over a large temperature range exhibit non-linear ionic conductivities with temperature. This equation is derived based on the viscosity properties of the material. It has the form shown in equation (8).

$$\sigma T^{1/2} = \sigma_0 \exp[-B/k(T-T_s)] \text{-----} (8)$$

where,  $\sigma_0 = n (ze)^2 C/k$

B-energy constant (not activation energy)

$T_s$ -reference temperature (equilibrium glass transition for polymers)

This equation fits well for liquid electrolytes and some less-viscous amorphous rubbery electrolytes [5,112].

#### 2.4.3 Williams-Landel-Ferry (WLF) equation

The WLF equation is a complimentary equation to the VTF equation. The WLF equation was derived for, and is a good fit to, most of the liquid phase polymer electrolytes. Its general form for ionic conductivity as a function of the temperature is shown in equation (9).

$$\text{Log}[\sigma(T)/\sigma(T_s)] = [C_1(T-T_s)/(C_2+(T-T_s))] \text{-----} (9)$$

Where,  $T_s$  – reference temperature for a polymer (empirically  $T_s-T_g \sim 50K$ )

$C_1, C_2$  – universal constants ( $C_1 \sim 8.9, C_2 \sim 102k$ )

In practice, the ionic conductivities of materials are obtained by measuring the bulk electrical resistance and taking into account geometrical factors. If 'R' is the bulk electrical resistance, 'l' is the shortest ionic traveling distance, and 'A' is the area of the electrolyte contacting area with the electrodes, then the ionic conductivity,  $\sigma$ , can be calculated by equation (10).

$$\sigma = l/RA \text{ -----(10)}$$

Here, most of the time,  $R$ , is obtained by an AC-impedance spectrum. (See appendix-3 for a brief introduction to the AC-impedance spectroscopy technique) [112].

## 2.5 Scanning electron microscopy (SEM)

Scanning electron microscopy (SEM) is a surface-sensitive imaging technique capable of nanometer spatial resolution providing topological, morphological and elemental composition information. It involves a highly focused electron beam rastering across a surface. This electron beam interacts with the surface through a wide range of scattering events to produce low-energy secondary electrons, high-energy backscattered electrons, x-rays, and Auger electrons. These x-rays and electrons can be independently detected using specialized detectors to produce useful signals. The SEM image is constructed using a raster mapping technique. This technique involves a detected signal, for

example that from the secondary electron detector, to be mapped onto a CRT (cathode ray tube) or computer screen with the x, y position representing the position of the electron beam on the surface and intensity proportional to the signal, to give a secondary electron image. In this way any signal can be mapped across the surface to give images indicating topography, crystallinity, composition etc. For surface characterization of a sample, there are four major imaging parameters, which can be adjusted that greatly affect the nature of the SEM image obtained and their optimization is dependent on the details of the surface electronic properties of the sample. These parameters are: the beam current,  $i_p$ , which controls the signal strength and the noise level; the beam accelerating voltage, ( $V_o$ ), which effects the resolution as well as the surface penetration depth; the probe convergence angle,  $\alpha_p$ , which can control the depth of focus and resolution; and the electron probe size,  $d_p$ , which primarily affects resolution and strength of signal. The user's ability to optimize these parameters allows the different properties of the surface to be imaged [113]. Figure 2.6 shows a schematic of the major beam parameters involved for obtaining an electron beam finely focused at the surface of a specimen.

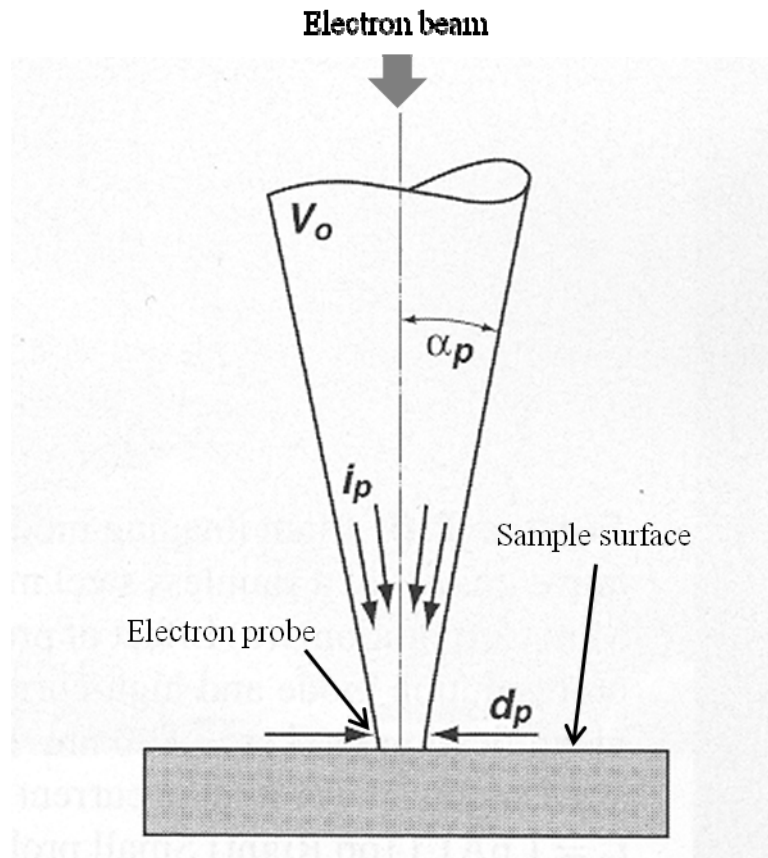


**Figure 2.6** Schematic of an electron probe parameters on a specimen:  $D_p$  - diameter,  $i_p$  - current,  $\alpha_p$  - convergence angle, and  $V_o$  - accelerating voltage [113].

In the next chapter, the detailed experimental procedures used for this research work are described. This includes: the fabrication of the AAO, nanopore templates, the synthesis of the PEO and PEO:LiTf polymer bulk films, and vacuum pulling the polymer into nanopore of the template.



## Chapter 3: Experimental Details

### 3.1 Introduction

In this chapter, the details of all the experimental procedures used in this research work are described. This includes: 1) the fabrication recipes of AAO templates with different pore densities and pore diameters, the coating of the AAO pores with SiO<sub>2</sub> layers to reduce the pore diameters, and the annealing recipe to remove the water content within the pores themselves; and 2) the vacuum-pulling method used to draw the polymers into the nanopores, followed by the removal of the thick polymer layers on the top and bottom of the polymer-filled AAO template. Removal of the water content [steps in 1.)] is important because the water content greatly affects the morphology of the polymer structure within the pores and can dominate the conductivity of the polymer electrolyte. Removal of the excess polymer on the top and bottom surfaces [steps in 2.] is crucial to be able to measure the nanoscale properties of the polymer and polymer electrolyte within the nanopores. Problems relating to the hygroscopic nature of both the PEO polymer and polymer electrolytes dominate much of this work. This hygroscopic nature required the development of the annealing procedures, and major modification of a glovebox to allow for the vacuum-pulling method as well as the routine measurement of electrical conductivity. Below I describe the methods in the order they were typically executed.

### 3.2 Fabrication of AAO templates

All oxalic and sulfuric anodic aluminum oxide (AAO) templates, with well-ordered nano-pores, were fabricated by following a two-step anodization process as described elsewhere [59, 63]. A detailed list of the fabrication steps are described in the appendix 4 [A4.4]. All the chemical details are provided in the appendix 4 [A4-1]. Before annealing of the starting aluminum metal surface, aluminum foil pieces with dimensions of 15 mm x 20 mm were degreased by following the cleaning procedure detailed in Appendix 4 [A4.3]. These foils were then annealed at 540 °C for 3 hours in forming gas (20% H<sub>2</sub> with a nitrogen balance) at a flow rate of 1 LPM in a LINDBERG/BLUE-M model TF555035A-1 tube furnace. The annealed pieces were degreased once again as described in Appendix 4 [A4.3] prior to electro-polishing. One side of the aluminum foil was electro-polished in a 3:1 mixture of perchloric acid: ethanol at 2 °C using a Pt foil as the cathode and applying a current of approximately 1 mA/mm<sup>2</sup>. For oxalic acid-produced AAO films (O-AAO), a 0.3M oxalic acid solution at 2 °C was used as the electrolyte to anodize the electro-polished aluminum foil. 40 V was applied between the Al foil serving as the anode and a Pt cathode for 2100 minutes to obtain a 100 μm thick O-AAO film with 45 nm diameter pores. A similar process was used for sulfuric acid-produced AAO films (S-AAO), where a 0.3M sulfuric acid solution at 2 °C was used as the electrolyte, and 26 V was applied for 760 minutes to obtain a 100 μm thick S-AAO film with 30 nm diameter pores (see appendix 4 [A4.5] for solution preparation data). The excess aluminum substrate

was dissolved from the template by immersing in a saturated mercuric chloride solution. With the Al substrate-removed, the 100  $\mu\text{m}$  thick AAO film was then cleaned with DI water and air-dried. The Aluminum and AAO film interfacial non porous thin barrier layer, grown during the pore growth, removed by chemical etching. For the barrier layer removal, the sample was floated on a 5% phosphoric acid solution and finally cleaned with DI water. For O-AAO barrier layer removal, the floating time is 28-30 minutes while the S-AAO barrier layer removal was 10-12 minutes. For comparison, figures 3.1 and 3.2 show SEM images of pore uniformity and the geometric pore distributions of the laboratory fabricated AAO films discussed above and commercially available anodic AAO films from Whitman Inc.

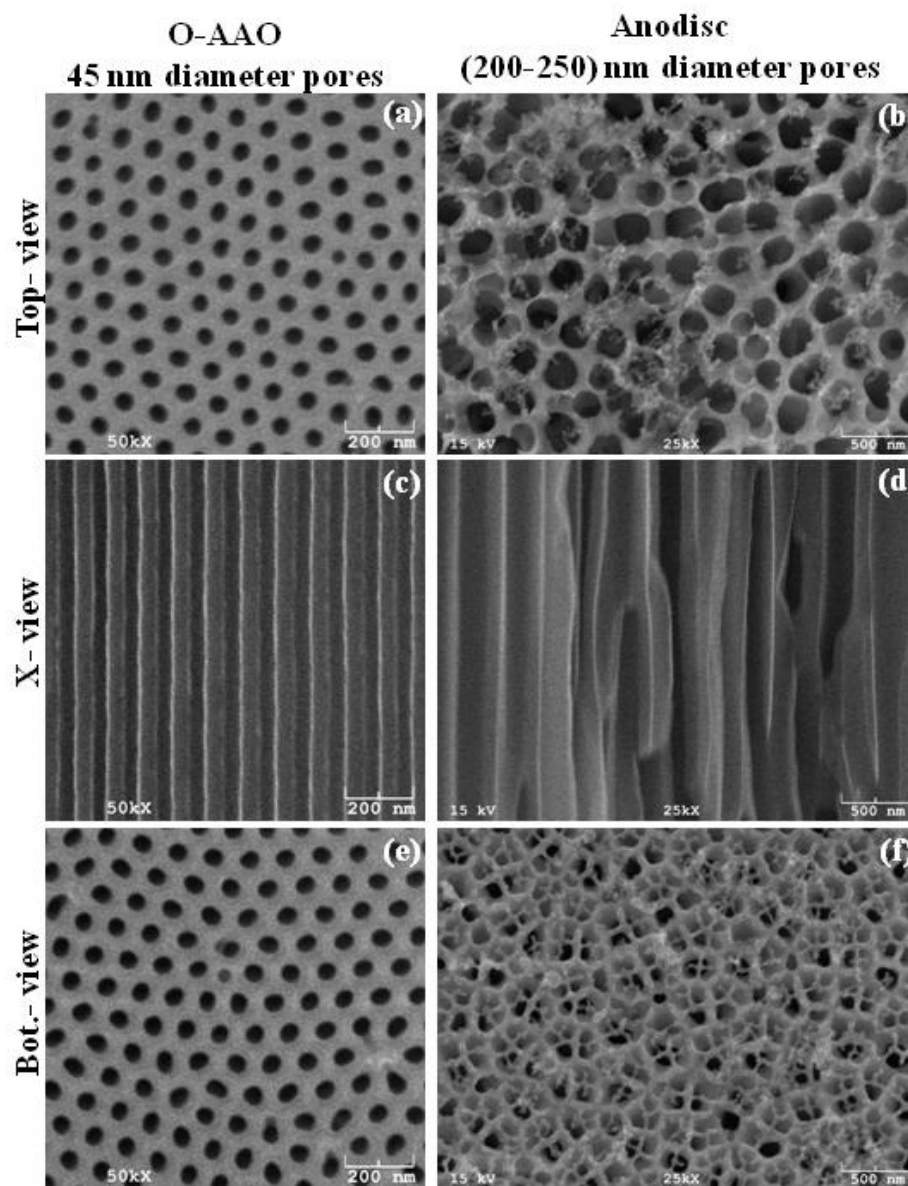


**Figure 3.1** SEM images of 45 nm pore size AAO anodized in oxalic acid solution (left) and commercially available 200 nm pore size anodisc from Whatman (right). (a), (b) are top surface views, (c), (d) are cross sectional views of the pores and (e), (f) are bottom surface of the AAO templates.

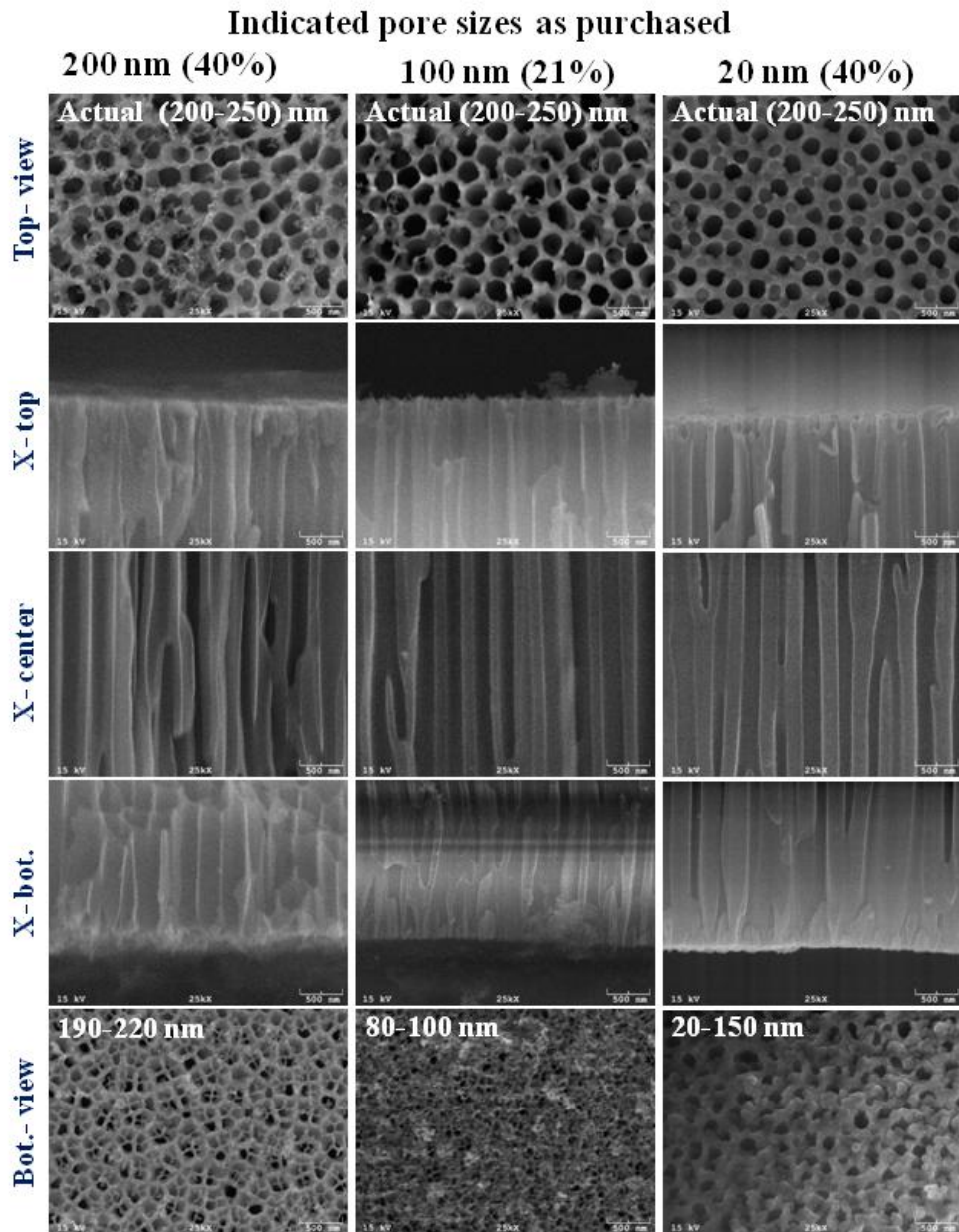


**Figure 3.2** Top down, cross-sectional (along the top, middle, and bottom length of the films), and bottom view SEM images of commercially available 60  $\mu\text{m}$  thick Whatman Anodiscs with specified pore diameters of 200 nm, 100 nm, and 20 nm. There is very little change in the average pore diameters of the AAO films looking top down while the non uniformity in the pore channels is evident in the cross-sectional views including a tapering of the pore diameters towards the bottom. The bottom surface of the anodiscs shows the distribution of the surface textured pore diameters to obtain the relevant specified pore sizes.

### **3.2.1 Annealing of AAO templates**

All AAO samples (size ~10 mm x10 mm) were annealed to remove the water and surface hydroxyl groups on all the surfaces (top, bottom and pore walls), as well as the oxalate ions in O-AAO and sulphate ions in S-AAO within the walls. This annealing was done by a two-step process to avoid mechanical breakdown and excessive deformation of the films. Firstly, individual templates were annealed (in a LINDBERG/BLUE-M model BF51732C-1 furnace) at 600 °C for 10 h with 2 LPM of high purity dry nitrogen flow into the chamber. To avoid mechanical breakage and stop the templates from curling, during the annealing process approximately 3 g of a 100 µm pore size porous ceramic piece was placed on top of the template and a 110 g ceramic weight was placed on top of that. Secondly, after the templates cooled to room temperature from the first annealing process, they were placed between porous ceramic pieces (~3 g each) and annealed (in a LINDBERG/BLUE-M model TF555035A-1 tube furnace) at 1000 °C for 15 hours in a dry nitrogen environment with a flow rate of 1 LPM.

### **3.2.2 Transferring annealed AAO into the inert atmospheric glove box**

It is very important that the annealed AAO samples are free of moisture before any preparation and characterization of PEO base polymer materials inside the pores. For that, the 15 hour annealed templates were allowed to cool down to 600 °C in the same atmosphere and carefully transferred inside the porous ceramic pieces into a pre-heated ceramic crucible at 600 °C. Within a few

seconds, the crucible with the AAO templates was transferred into a desiccator connected to a vacuum pump. The vacuum desiccator was transferred into a sample processing dry nitrogen filled glove box. FTIR spectra showed that these samples were free of water as compared to non-annealed samples. Both FTIR and Raman spectra were taken prior to the polymer insertion into the pores.

### **3.3 Coating of SiO<sub>2</sub> layers onto AAO pore walls**

Smaller AAO pore diameters of 18 nm, 22 nm, 26 nm and 41 nm were obtained by depositing SiO<sub>2</sub> layers onto the pore walls of as grown AAO templates (typical size for S-AAO is 30 nm and for O-AAO 45 nm ). The uniform deposition of a 2-nm-thick SiO<sub>2</sub> layer was done by liquid-phase chemical deposition onto the surface of the AAO pore walls. This single-layer deposition step was then repeated multiple times to achieve smaller AAO pore diameters. The deposition of the SiO<sub>2</sub> layers was done in an inert glove box because it uses SiCl<sub>4</sub> (l) which vigorously decomposes in air.

There are several steps for the SiO<sub>2</sub>-coating process. A detailed procedure is shown in appendix-5. In brief, different solutions are vacuum-pulled consecutively through the nanopores. The steps are: 1. SiCl<sub>4</sub>(l) is vacuum-pulled through the pores and allowed to dry; 2. CCl<sub>4</sub>(l) is vacuum-pulled through the pores to rinse and remove any excess SiCl<sub>4</sub> on the pore walls; 3. 1:1 CCl<sub>4</sub>:methanol solution is vacuum-pulled through the AAO pores to dilute the

previously deposited  $\text{CCl}_4$  on the walls; and finally 4. ethanol is vacuum-pulled to remove any additional  $\text{CCl}_4$  on the walls.

Our experimental results and the literature [115,116] indicate this procedure deposits 2 nm of  $\text{SiO}_2$  for one deposition cycle. By repeating three deposition cycles, AAO pores with initial diameters of 30 nm can be reduced to diameters of 18 nm (with 6 nm thick  $\text{SiO}_2$  walls on the pore surface). Figure 3.3 shows the SEM pictures of all pore geometries.

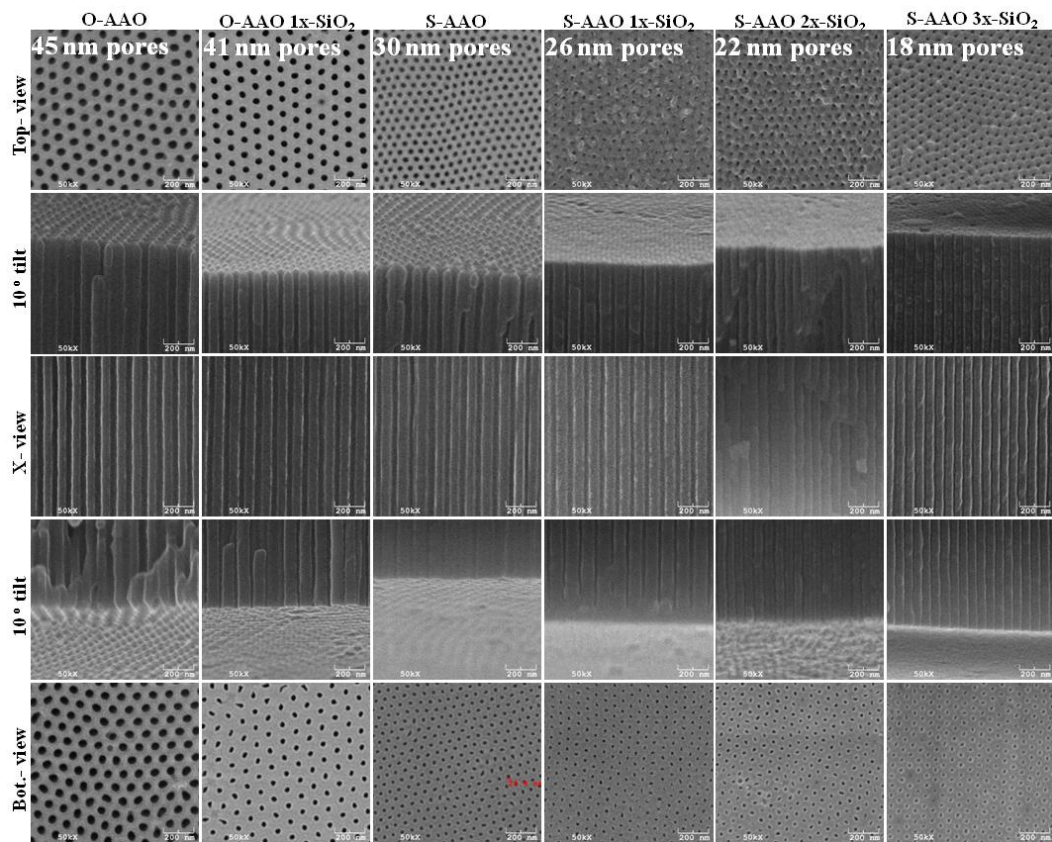


**Figure 3.3** SEM images (top view,  $10^\circ$  tilted top, cross-sectional,  $10^\circ$  tilted bottom, and bottom view) of  $100\ \mu\text{m}$  thick O-AAO and S-AAO templates before and after deposition of 1-3 layers of a 2 nm thick  $\text{SiO}_2$  chemical deposition.



### 3.4 PEO polymer and PEO:LiTf(X:1)<sub>X=10,30</sub> bulk films fabrication

Bulk films of PEO polymer and PEO:LiTf(X:1)<sub>X=10,30</sub> were prepared as controls for characterization measurements to compare to the vacuum-pulled PEO-polymer materials inside the AAO templates. Details of all the chemicals are listed in the Appendix 4 [A4-2]. These bulk PEO:LiTf(X:1)<sub>X=10,30</sub> polymer electrolyte complexes were prepared by measuring appropriate weight ratios of the ether-oxygen of the PEO polymer to Li<sup>+</sup> ions in the LiTf and dissolving in acetonitrile. This solution was magnetically-stirred overnight in the glove box and cast into a Teflon container to evaporate the acetonitrile. The acetonitrile free PEO:LiTf(X:1)<sub>X=10,30</sub> electrolyte was kept open for more than four days in the glove box prior to use. By a similar manner, pure PEO polymer was prepared by dissolving in an appropriate volume of acetonitrile to keep the preparation conditions similar. These polymer materials do not make films like high molecular weight PEO but instead agglomerate in the Teflon container. To make uniform 100- $\mu$ m-thick films, a one-inch-diameter Teflon sheet, heated to 120 °C, was placed on top of a one-inch-diameter ZnSe window seated in a slip-fit metal-core holder with a 100- $\mu$ m-thick, one-inch-outer-diameter Teflon spacer. At 120 °C, an appropriate small piece of polymer material was placed at the center of the Teflon sheet and brushed/stirred with a Teflon stick for three minutes to remove any air bubbles. Finally, another one inch Teflon sheet was aligned on top of the spacer and pressed down with another ZnSe window to make the 100  $\mu$ m thick

film. These films were then used for FTIR, FT-Raman, WAXS, and conductivity measurements.

### **3.5 Vacuum-pulling of polymers into AAO pores**

A schematic and optical micrograph of the vacuum-pulling apparatus within a glove box is shown in figure 3.4. An optical picture of the complete glove box set-up (with feedthroughs) is shown in appendix 6 [A6.3]. The tube to pull the vacuum is connected to an outside vacuum pump by a feedthrough connection. Three vacuum gauges are used for monitoring the pressure during the pulling process. One is connected at the pump, one at the controller, and one near the sample. The vacuum-pulling holder/base for the sample is made of stainless steel with a 2-mm diameter hole. This holder/base is positioned on a hotplate. For polymer material (pure PEO and PEO:LiTf(X:1)) insertion into the pores, the AAO template is placed on a 4-mm-nominal-inner-diameter and 1.75-mm-thick O-ring (2-008) centered on top of the vacuum hole.

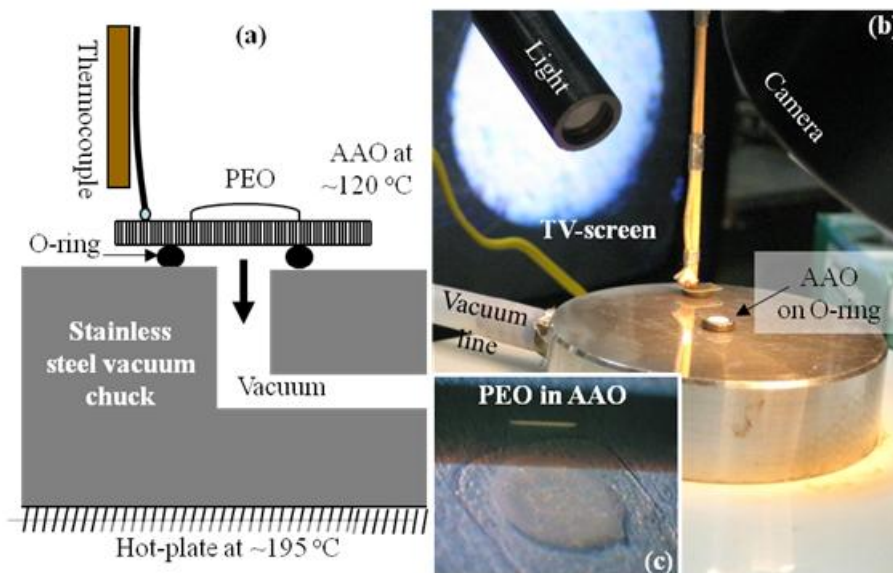


**Figure 3.4** Schematic of apparatus used to pull polymer materials into AAO pores (a) and photograph of the apparatus used to pull the polymer through the AAO pores (b). All the equipment is in a glove box. An image (c) of the as-pulled PEO material in and on the AAO is shown (inset).

Initially, vacuum of 2" of Hg is applied to securely hold the sample on the O-ring. (Here our vacuum is measured as inches of Hg below atmospheric pressure.) An initial temperature of 120 °C on the top surface of the AAO template is obtained by setting the hotplate temperature to 190 °C. The AAO templates are left at 120 °C for more than 30 minutes prior to pulling polymer material. An amount of polymer material covering the pulling area is spread on top of the AAO and stirred/brushed slowly with a Teflon stick for 2 min. while it melts with vacuum level at 2" of Hg maintained on the AAO film. During this time, any air bubbles were removed from the pulling area by monitoring the live image taken by a camera mounted on top of the sample and connected to the computer by a feedthrough in the glove box. During the next two minutes, the

pulling vacuum is increased to 8" of Hg and then further increased to 16" of Hg for the following minute. During the last 10 seconds of the polymer pulling process, the bulk excess of remaining polymer material on top of the AAO film was wiped off with a triangular-cut (for wiping convenience) polishing cloth (South Bay Technologies, P/N PMT08A-10). Finally, the vacuum pressure is released, and the AAO sample is lifted off the O-ring and left to stand in the open in the glove box for more than 12 hours.

### **3.6 Removal of excess polymer from top and bottom of AAO**

For removal of the excess polymer material on the top and bottom, the sample was placed on top of a porous Teflon surface with 25- $\mu\text{m}$  average pore diameter (Small Parts, Inc.) and an acetonitrile drop was placed over the excess polymer material on the top AAO surface. After 2-3 seconds, the drop was gently wiped off with an acetonitrile-damp polishing cloth cut in a triangular shape. This process was repeated for the other side of the film and then the film was left in the glove box for more than 24 h prior to any characterization.

The following chapter describes the instrumentation and techniques used to characterize and evaluate the properties of the PEO and PEO:LiTf(X:1)<sub>X=10,30</sub> polymer bulk and confined material.

## **Chapter 4: Characterization of PEO and PEO:LiTf- Polymer**

### **Materials Filled AAO**

#### **4.1 Introduction**

In this chapter, the SEM, FTIR, FT-Raman and WAXS instrumentation used for this research work is discussed. Throughout this chapter, the new sample holders and procedures developed here to safeguard the integrity of the PEO polymer materials is emphasized.

#### **4.2 Scanning electron microscopy (SEM)**

Scanning electron microscopy was performed using a JEOL JSM-880 SEM with a lanthanum hexaboride ( $\text{LaB}_6$ ) gun typically operating at 15 kV. All samples were mounted on SEM sample holders in the glove box and transferred in a vacuum desiccator to the Emitech-575XD turbo-pumped sputter coater to coat the samples with  $<5$  nm of iridium for better electron conduction. The iridium-coated samples were taken to the SEM in a vacuum desiccator and the time exposed to the outer environment during transferring was less than 10 sec. Figure 4.1 shows SEM micrographs of 45 nm diameter AAO nano pores filled with PEO:LiTf(10:1).

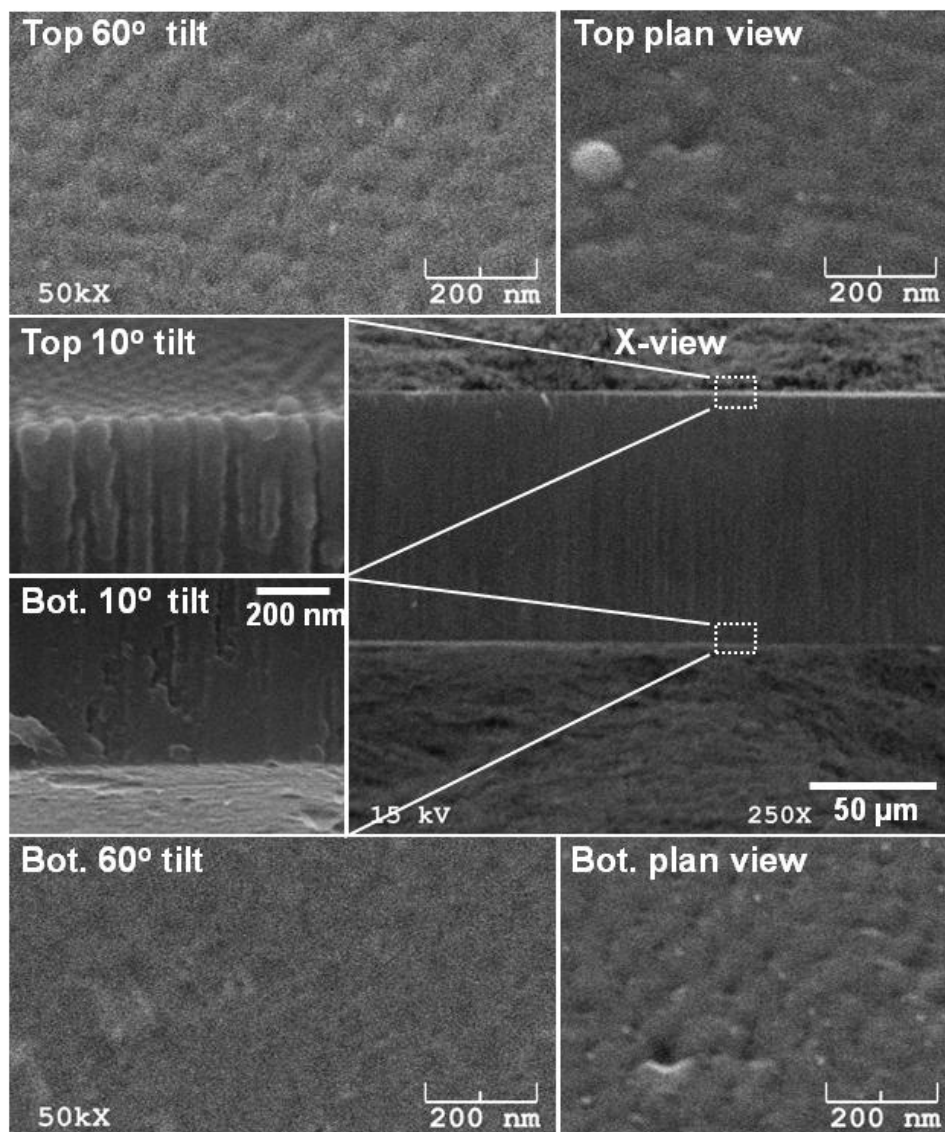


**Figure 4.1** SEM micrographs showing several views of a PEO:LiTf(10:1) filled O-AAO template with 45 nm pores. The negligible thickness of the excess polymer layers on the polymer-filled template should be noted.

### 4.3 FTIR spectra

FTIR spectra were taken using a Bruker IFS 66v spectrometer in the spectral region  $400\text{-}4000\text{ cm}^{-1}$  with a KBr beam splitter and  $1\text{ cm}^{-1}$  resolution. The data acquisition was controlled by a computer running the OPUS program. A schematic diagram of the spectrometer is shown in figure 4.2.

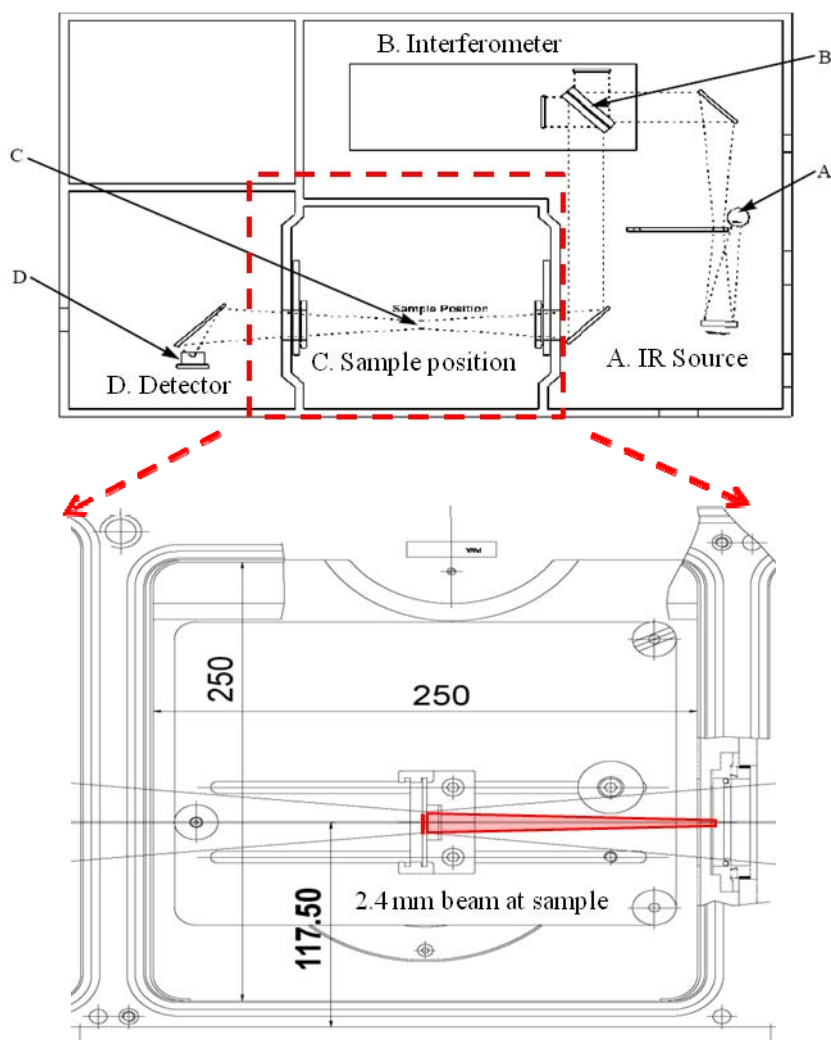


**Figure 4.2** Schematics of the IFS 66v/S IR spectrometer sample compartment and the optical path (from IFS 66v/S IR manual).

The beam diameter at the sample was reduced to 2.4 mm by adjusting the aperture size and aligned to the sample center, which had an effective diameter of 4 mm. Sixty four scans were taken per spectrum to increase the signal to noise ratio. The sample chamber was purged with dry nitrogen during loading and unloading of the samples and kept under vacuum during the scans. All samples were loaded into the custom designed IR sample holder while in the dry nitrogen glove box. The custom holder centers the sample effective area to the beam and is shown in figure 4.3.

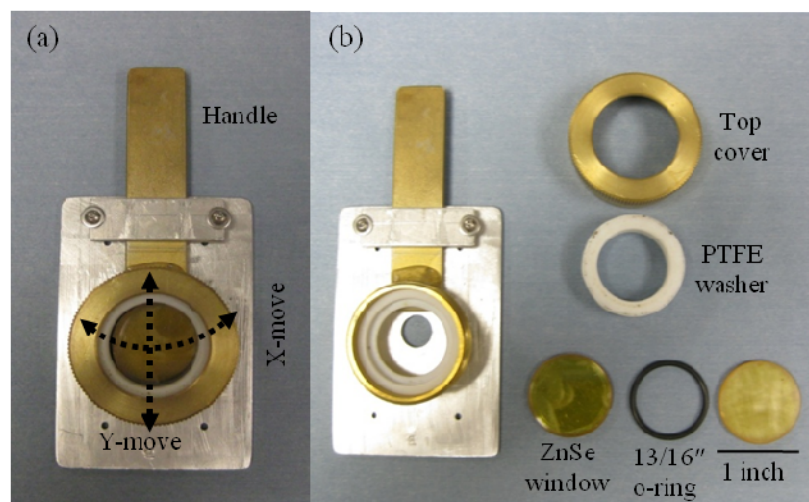


**Figure 4.3** Custom designed leak tight FTIR sample holder with XY adjusting ability. (a) Full assembled holder, (b) holder parts in apart.

The air-tight sample holder allows X-Y tilting to align the sample center to the beam with the aid of an IR sensing card. As shown in figure 4.2, the IR beam is incident on the back surface of a ZnSe window roughened with 10  $\mu\text{m}$  particle size alumina powder to reduce the effects of “etaloning” in the IR spectra. A single rough surface is a crucial factor to obtain cleanest spectra because the 100-



$\mu\text{m}$  AAO films on their own show etalon interference. Before acquiring an IR spectrum of the sample, a background spectrum of the empty sample holder with ZnSe windows was taken so that it be appropriately removed from the raw sample spectrum using OPUS. After the IR spectrum was taken, the sample was unloaded from the IR sample holder and mounted in the Raman sample holder in the glove box to take a Raman spectrum. Just after the Raman spectrum was collected, in the glove box, the sample was transferred back to the IR sample holder and a FTIR spectrum was taken again, to monitor the amount of trace atmospheric moisture picked up by the sample during our FTIR and Raman procedures. The before Raman and after Raman IR spectra scans showed that the change of the -OH peak absorbance was insignificant, indicating the absence of moisture picked up during the 10-hour Raman scans.

#### **4.4 FT-Raman spectra**

FT-Raman spectra were taken by a Bruker-FRA 106/S FT-Raman spectrometer as shown in figure 4.4. This spectrometer uses a solid state laser diode pumped Nd:YAG excitation source operating at 1064 nm with wavelength stability  $<1\text{ cm}^{-1}$  and a having a bandwidth of  $0.5\text{ cm}^{-1}$ . The D 418-S Raman detector is liquid nitrogen cooled during the scans. All spectra were obtained by using the double sided, forward backward acquisition mode and the Raman laser power set to 1200 mW. The beam diameter at the sample was  $100\ \mu\text{m}$ . FT-

Raman spectra were acquired for all samples immediately after the IR spectra were obtained.

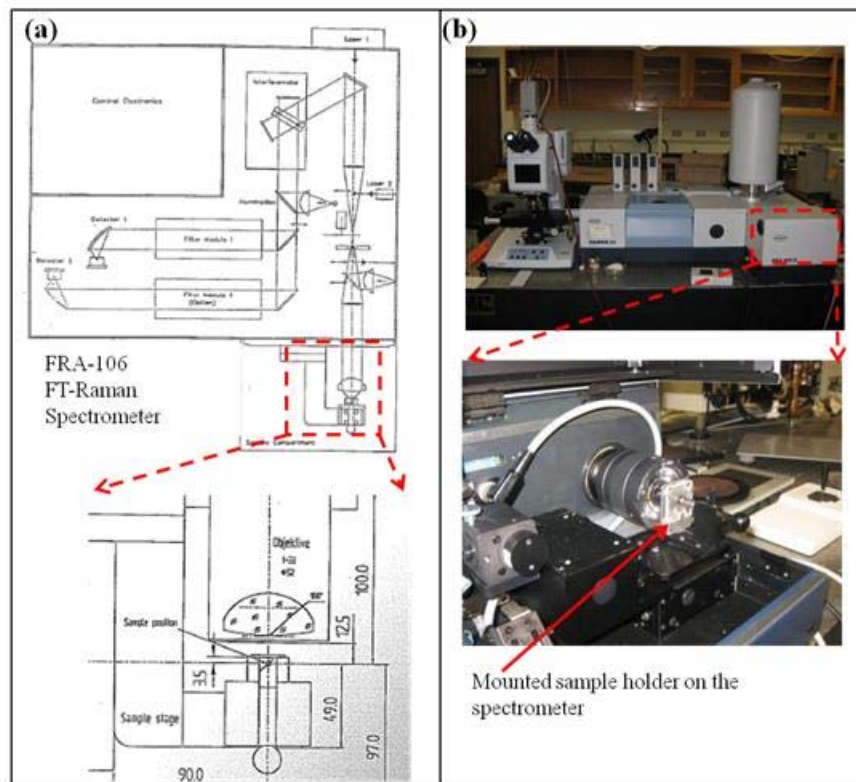


**Figure 4.4** Schematics of FRA-106 spectrometer sample compartment and optical path (a), and optical picture of the FRA-106 spectrometer and the sample compartment (b).

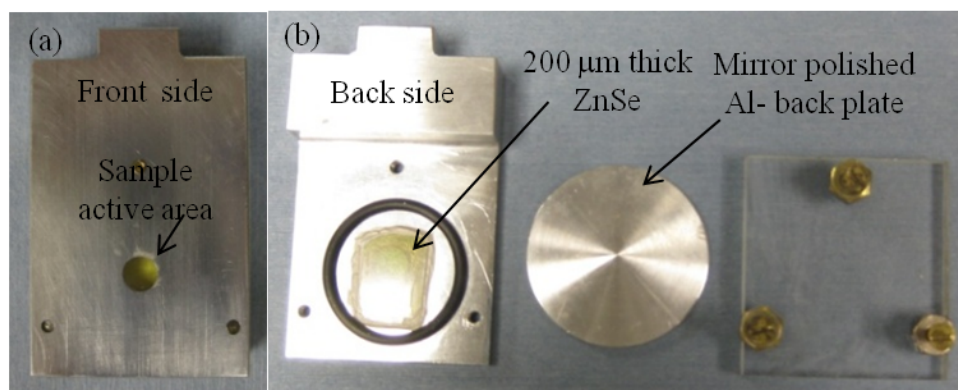


**Figure 4.5** Custom designed Raman sample holder with air tight ability. Sample placed on the 200 mm thick ZnSe window. (a) Laser incident side, (b) holder in part for sample mounting.

A quartz beam splitter was used, and the FT-Raman the spectral region was 50-3500  $\text{cm}^{-1}$  with 2  $\text{cm}^{-1}$  resolution. Acquisition was controlled by a computer using the OPUS computer program. All samples were loaded into the Raman sample holder in the dry nitrogen glove box. Again the Raman sample holder was custom designed to avoid moisture absorption by the hygroscopic sample from the surroundings, and is shown in figure 4.5.

The beam is incident onto a ZnSe window whose thickness is 200  $\mu\text{m}$  to maximize the scattered spectral intensities. For the AAO-based samples, 10,000 scans were carried out to get spectra with sufficient signal-to-noise (S/N) ratio, while for the bulk polymer materials, 1000 scans were sufficient.

#### **4.5 WAXS diffractograms**

X-ray measurements were made using a pinhole-collimation S-MAX3000 system from Rigaku with a microfocus tube. The x-rays were produced from a copper source using a 45 kV electron beam with 0.66 mA of current and collimated using 3 pinholes to a 400  $\mu\text{m}$  beam diameter. Wide-angle x-ray spectra (WAXS) were collected with a FUJIFILM BAS-IP MS 2325 imaging plate with a hole cut in the center of the plate (which allows for simultaneous small-angle measurements, which were not made) placed perpendicular to the incident x-ray beam, approximately 5 cm away from the sample. The sample chamber was kept under vacuum during the spectra acquisition. The exposed image plates were scanned using a FUJIFILM BAS-1800II image reader.

It is crucial that the PEO-based polymer samples remain in a moisture-free environment, because they are highly hygroscopic and would otherwise quickly become hydrated and amorphous. In addition to the concern of moisture in the environment, the AAO templates themselves must be annealed at high temperature to remove the water (initially several monolayers thick) from the pore walls of the as-fabricated AAO. Table 2 shows the annealing temperatures and the type of –OH groups on remaining on the pore walls at the various stages.

**Table 2.** Existence of the water and –OH groups after annealing at various temperatures.

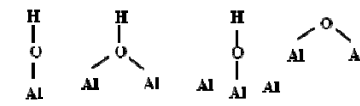
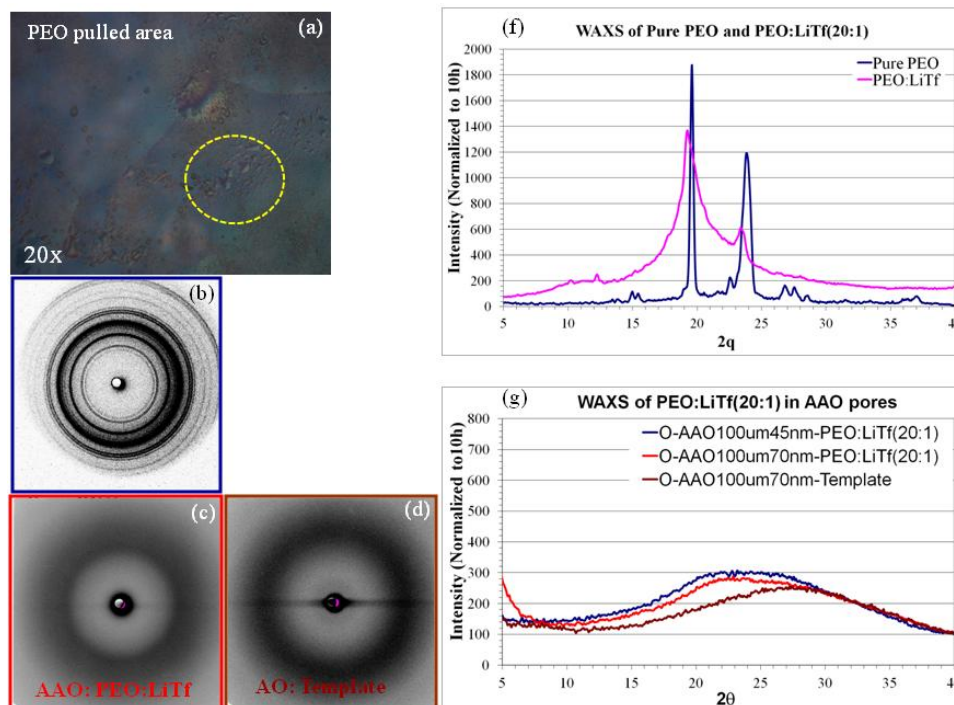
<b>As grown</b>	<b>130 °C Anneal</b>	<b>500 °C Anneal</b>	<b>1000 °C Anneal</b>
Fully hydroxylated <b>Acidic Surface</b>		Only fixed –OH & remainder –O <b>Neutral surface</b>	all –OH removed, fully oxidized <b>Basic Surface</b>
Several monolayers (MNs) of H <sub>2</sub> O	1 ML of H <sub>2</sub> O		& isolated (fixed) Al-OH

Figure 4.6 shows the diffraction patterns of PEO:LiTf(20:1) in 45 and 70 nm AAO nanopores taken under normal lab conditions (moisture rich), (c) and (d); and figure 4.6(b) is a deffractogram of PEO:LiTf(20:1) bulk sample taken under inert conditions.



**Figure 4.6** Hygroscopic behavior of PEO and PEO:LiTf; (a) Optical micrograph of a PEO:LiTf (10:1) in O-AAO vacuum pulled outside the glove box showing water accumulation in tens of seconds, (b) Diffractogram of PEO:LiTf(20:1) under inert conditions, (c)(d) PEO:LiTf(20:1) in O-AAO and template showing amorphous structures respectively, (f), (g) Intensity vs.  $2\theta$  histograms of previous diffractograms.

To maintain moisture-free conditions, the samples were loaded on to the WAXS sample holder in the dry-nitrogen-filled glove box and transferred to a vacuum desiccator that was evacuated outside the glove box. Samples were exposed to normal atmosphere less than 10 seconds during loading and unloading of the samples into the WAXS chamber. Polymer materials as bulk film samples were exposed to the x-ray beam for about 6 hours and the polymer materials confined in AAO samples were exposed more than 16 hours to obtain sufficient signal in the diffractograms. To further investigate the polymer orientation in the nanopores, we also performed WAXS of the AAO-confined PEO and PEO:LiTf

(10:1) samples with sample normal tilted at  $10^\circ$  to the x-ray beam. The x-ray exposed image plates were scanned using a FUJIFILM BAS-1800II model image reader to obtain digital pictures.

#### 4.6 AC-impedance spectra and conductivity

For ionic conductivity measurements, the bulk resistance of the films was obtained from AC-impedance spectra. The HP4192A impedance analyzer was connected with 1-m-long 50-Ohm BNC cables through a feed-through to the 1.52 mm diameter sample contact electrodes mounted in the glove box, as shown in the block diagram in figure 4.7 (see appendix 6, [A6.1] for glove box set up).

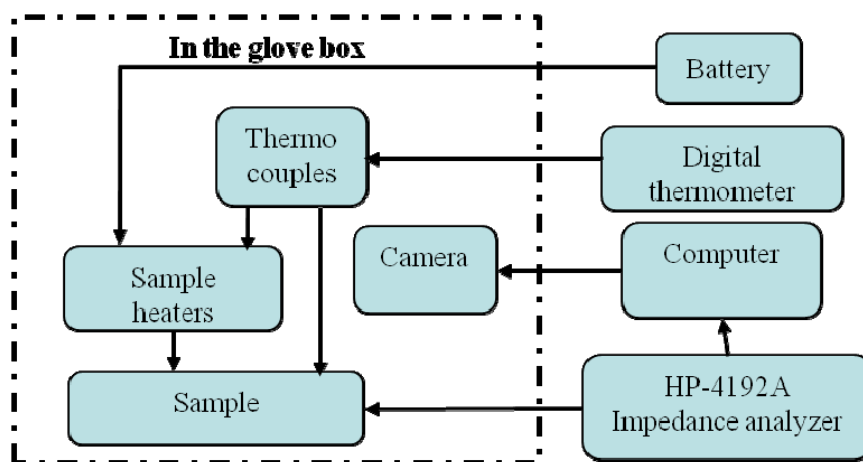
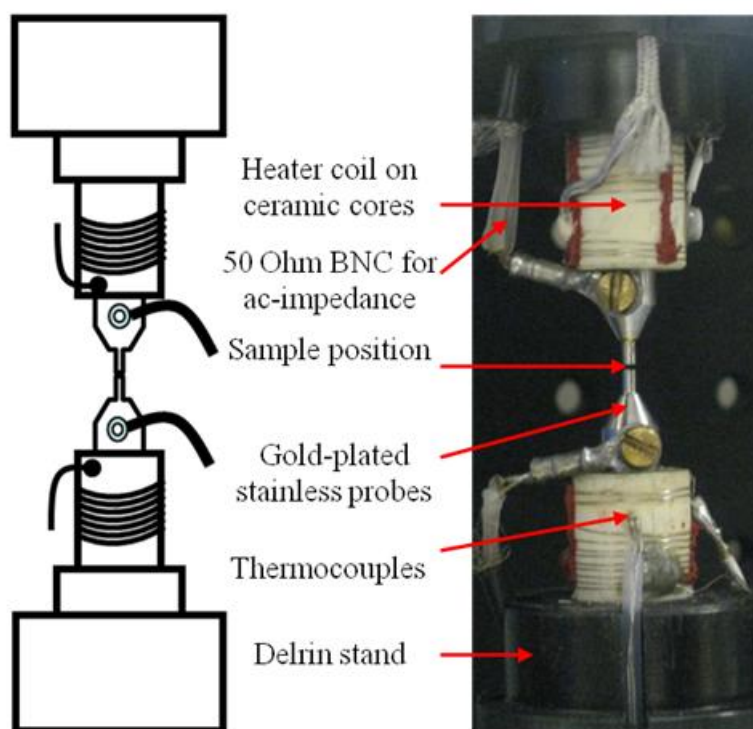


Figure 4.7 Block diagram for the AC-impedance measurements setup.

Before all impedance measurements, the leads and contact probes resistances and capacitance were compensated for by obtaining short-circuit and open-circuit measurements at a frequency of 1 MHz with a 0.025 V amplitude

oscillation. The impedance spectra were taken by (logarithmically) sweeping in the spectral region 100Hz to 10 MHz with 0.025 V oscillator amplitude. The custom-designed sample-contact electrode assembly used for these measurements is shown in figure 4.8 (see appendix 6 [A.6.2] for complete set-up). With the xyz-mechanical stages included in this assembly, we could routinely align the contact probes to the mm-diameter active areas of the samples and make reliable electrical contact. This success required the use of a computerized optical digital camera (in the glove box) to monitor the relative positions of the contact probe/sample/contact probe with sub-mm resolution.



**Figure 4.8** Schematic (left) and optical image of AC-impedance contact probes. The probe contact area is 1.52 mm in diameter, gold coated, and insulated from the heater coils with ceramic.

A series of impedance spectra were taken for the 100- $\mu\text{m}$ -thick PEO:LiTf(10:1) bulk film for temperatures from room temperature, 25  $^{\circ}\text{C}$ , to 90  $^{\circ}\text{C}$  in 10 degree increments. Before each impedance spectra, the sample was held at temperature for 45 minutes to ensure a uniform temperature. To initially prepare the sample for these measurements, the PEO:LiTf(10:1) bulk film was inserted between the probes, at room temperature, and heated to 60  $^{\circ}\text{C}$  for 10 minutes to make better contact with the electrodes, and the surrounding melted material was carefully removed with a PTFE stick. Then sample was cooled to room temperature prior to the start of the series of impedance spectra.

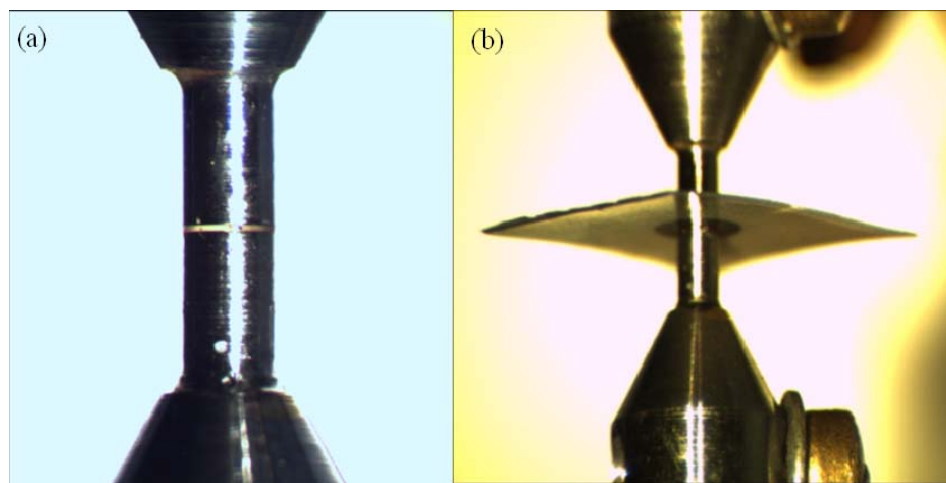


**Figure 4.9** A 100  $\mu\text{m}$  PEO:LiTf (10:1) film in the 1.5 mm diameter contact probes (a), PEO:LiTf (10:1) in O-AAO film in the contact probes (b).

Figure 4.9 shows optical micrographs of a 100  $\mu\text{m}$  PEO:LiTf (10:1) bulk film between the probes (left) and an AAO-confined PEO:LiTf(10:1) sample between the same contact probes (right) . For the AAO-confined samples, the



first impedance spectrum was collected at 25 °C. Then a series of impedance spectra was obtained for temperatures from 30 to 90 °C in 10 degree increments. Again, before each impedance spectra was obtained, the sample was held at the stabilized temperature for 45 minutes to ensure that the sample was at a uniform temperature. To get better electrical contact for the nanopore-confined PEO:LiTf (10:1) samples, 150-nm-thick sputtered Au contacts were deposited on the front and back of the samples (using the Emitech-575XD turbo-pumped sputter coater, operated with an Ar plasma). The front and back contacts were deposited in two successive sputter runs with the sample clamped between aligned-holes in a folded Kapton sheet. The contacts were  $2.00\pm 0.01$  mm in diameter and typically aligned to better than 0.1 mm. Samples were kept in a vacuum desiccator while they were transferred from the glove box to the sputter coater and from the sputter coater to the glove box.

The bulk resistances for conductivity measurements were obtained from the radius of the semicircles in the Nyquist plots. For our temperature range, there was more than an order-of-magnitude variation in conductivity (diameter of the half circle). Accurate determination of the diameter was greatly aided by taking impedance scans throughout this temperature range and carefully observing the trends with temperature. This approach allowed us to confidently determine accurate resistances even when our half-circles did not start at the origin (high frequency end of the scan) or the half-circle did not completely return to the x-axis (low frequency end of scan). To confirm the correct behavior of our

electrical contact procedures, we took impedance scans for a series of temperatures (30, 50, 70 and 90 °C, then 70, 50, and 30 °C). Then we increased the size of the smaller contact, by sputtering a new, larger Au contact centered on top of the original contact. Impedance scans were then repeated for the same series of temperatures. Comparing Nyquist plots we find the resistances are the same for each temperature before and after the second Au contact on one side was enlarged. See figure 4.10 for details. This indicated two important points: 1) our sputtered-Au contacts were stable and reliable, and 2) appreciable conduction through the film only takes place where the Au contacts on the two sides overlap. The latter point confirmed that the ultra-thin layer of polymer electrolyte that remained on the top and bottom surfaces of the AAO templates did not contribute to the impedance measurements. Again, only the polymer electrolyte within the pores contacted on both sides with our Au contacts contributed to the impedance.

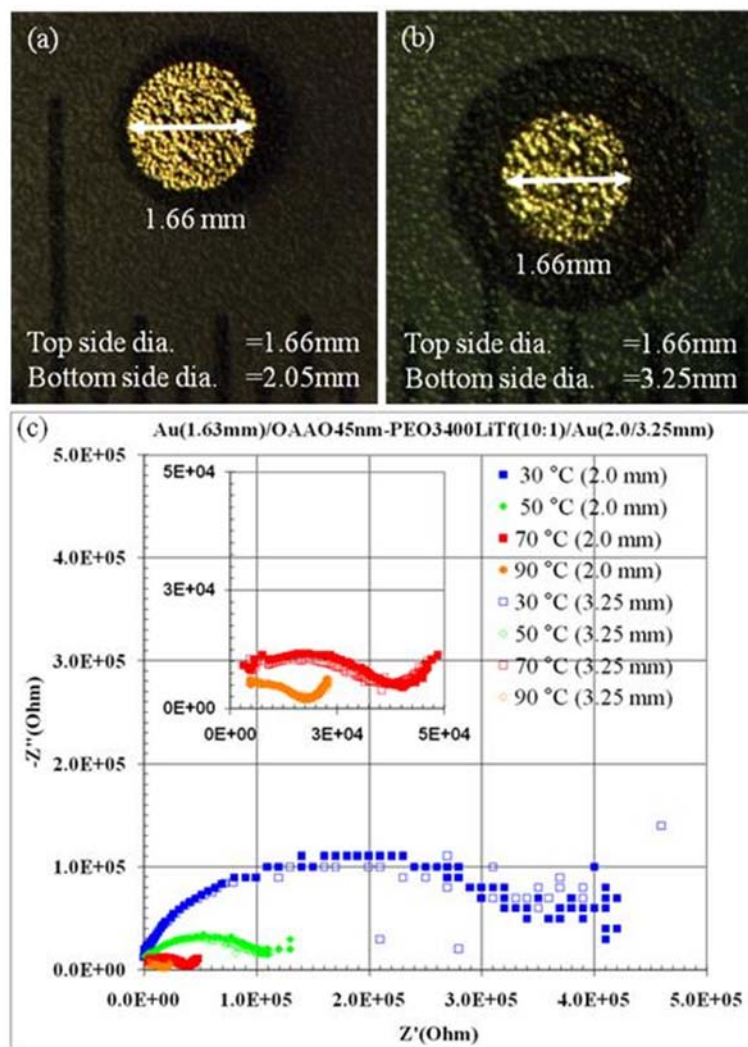


**Figure 4.10** Bulk resistance for different gold contact areas: (a) Measured the same O-AAO-PEO:LiTf (10:1) sample with different contact configurations Top (Bot.) contact  $\phi=1.66$  (2.05) mm , (b) Top (Bot.) contact  $\phi=1.66$  (3.25) mm, (c) Nyquist plots of AC-impedances of different gold contact configurations measured at 30 °C, 50 °C, 70 °C and 90 °C; closed symbols for Au(1.63mm)/O-AAO45nm-PEO:LiTf(10:1)/Au(2.0mm) and open symbols for Au(1.63mm)/O-AAO45nm-PEO:LiTf(10:1)/Au(3.25mm).

#### 4.6.1 Determination of ionic conductivity in nano-pores

The electrical contact area of the nano pores filled electrolyte was obtained by multiplying the porosity factor ( $P$ ) of the AAO film, as calculated from the pore dimensions (see figure 4.11), and the actual Au coated area ( $A$ ) on

the film for electrical measurements. The bulk conductivity was calculated from the usual Ohm's law equation:  $\sigma = l / [R (PA)]$ ; where,  $l$  is the film thickness and  $R$  is the geometric bulk resistance obtained from the Nyquist plot.

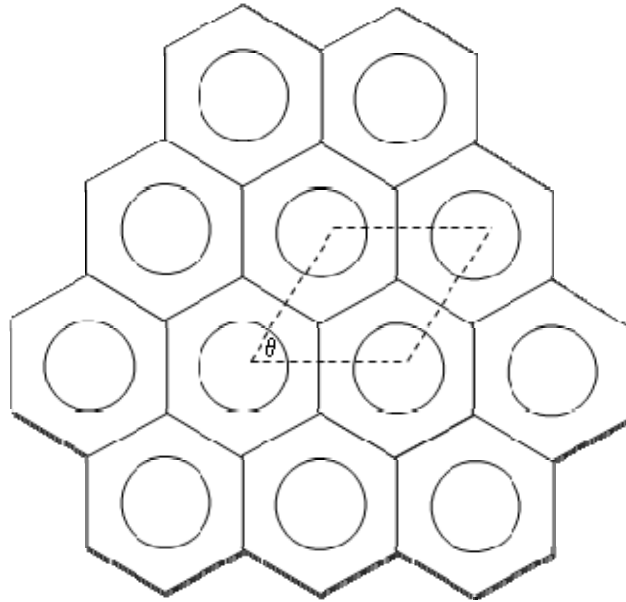


**Figure 4.11** Schematic diagram for pore dimensions of AAO porosity calculation; circle depicts as pore and hexagonal boundary shows the outer dimension of a single pore.

$$\text{Area of single pore} = \pi (d/2)^2$$

$$\text{Area of a unit cell} = \text{Pore distance(C-C)}^2 \times \sin(\theta)$$

$$\text{Porosity} = [\text{pore area} / \text{pore cell area}] \times 100$$

$$\text{Porosity} = [\pi \times (d/2)^2 / \text{Pore distance(C-C)}^2 \times \sin(\theta)] \times 100$$

In the next chapter, the results obtained from above characterization methods for the PEO and PEO:LiTf (10:1) bulk, and confined systems are presented and discussed.

## Chapter 5: Results and Discussion

### 5.1 Introduction

The results and discussions for our study of polymer materials in confined structures are presented. This involves the sections addressing: the AC-impedance and conductivity; the FTIR and FT-Raman; and the x-ray measurements; followed by a discussion summarizing the results. An important aspect of this work was the large number of confined structures (including templates with pore sizes of: 200, 45, 41, 30, 26, 22, and 18 nm) that were necessary to discriminate between areal versus perimeter effects in these confined structures. Furthermore to understand the details of the organizational behavior of polymer materials in confined structures, we needed to study both PEO and PEO:LiTf(10:1) in all template sizes (PEO:LiTf(30:1) in a few) with all the tools possible (AC-impedance, plan- and cross-sectional view SEM, FTIR and FT-Raman, and x-ray diffraction). This means we analyzed many samples with many techniques. In the sections that follow, we only present the highlights. Details are included in appendices covering each technique. Before starting the individual sections, a brief synopsis of each section is presented in the paragraph below.

In the AC-impedance and ionic conductivity section, presents Arrhenius plots of the conductivity versus temperature. These plots show: the expected activation energy for the bulk PEO:LiTf(10:1) films with the freezing/melting at

~59 °C; the PEO in 200-nm pore-diameter Anodisc with the expected melting and expected liquid activation energy, but with significantly lower solid activation energy (higher conductivity); and that the AAO-confined structures notably have no clear melting and the Arrhenius plots can be fit with a single line with a low activation energy. Associated with this latter behavior, the AAO-confined structures have a room-temperature conductivity 100× that of the bulk polymer-electrolyte (when normalized for porosity). Plotting the room-temperature conductivity per pore versus pore radius shows this enhanced conductivity is an area and not a perimeter effect. This indicates that the effect is due to the “bulk” structure of the polymer electrolyte in the pore and not the polymer-electrolyte/template interface. To investigate this polymer electrolyte structure we characterize the samples with IR spectroscopy and WAXS. Because the PEO:LiTf polymer electrolyte is more complex than the PEO polymer alone it was characterized both using these techniques.

In the FTIR and FT-Raman spectroscopy section, the transition moments of the various normal modes are assigned as either perpendicular or parallel to the chain axis as explained by factor group symmetry. The pure PEO vibrations have the  $D(4\pi/7)$  factor group, while those of crystalline  $P(EO)_3:LiTf$  have the  $C(2\pi/2)$  factor group. Therefore, it is possible to assign the transition moments of the various normal modes as either perpendicular or parallel to the chain axis. In the case presented here using a shorter-chain polymer, it is difficult to assess the

polymer alignment within the confined structures. The data is consistent however with alignment of the polymer chain with the pore direction.

In the x-ray section, the WAXS patterns are discussed. With WAXS one can determine the alignment of the crystalline phases of the polymer materials and calculate the percent crystallinity of the PEO. However, we were only able to determine the percent crystallinity of bulk samples, because in the WAXS patterns of the confined structures, the usual amorphous halo of PEO phase is obscured by the broad crystalline peaks associated with the AAO. The WAXS patterns of the bulk and Anodisc samples showed the usual random polycrystalline order. For the AAO-confined structures, the initial on-axis WAXS patterns showed little crystalline polymer material, however, when they were tilted at  $10^\circ$  to look for alignment of the polymer chain with the pore axes, the diffraction peaks associated with the appropriate planes strongly diffracted showing the azimuthal pattern expected for polymer chains aligned to the pore axis. The same result was observed for the PEO:LiTf confined in the PEO. However, this polymer-chain alignment effect was not observed for PEO confined in Anodisc.

## **5.2 AC-impedance and ionic conductivity**

In this section, I present the AC-impedance data from Nyquist plots, followed by Arrhenius plots of the conductivity with temperature, followed by a plot of the conductance per pore versus pore diameter. As expected, the bulk

PEO:LiTf(10:1) film shows the usual activation energies with melting/freezing at  $\sim 59^\circ$ , the PEO:LiTf(10:1) in 200-nm pore-diameter Anodisc shows the melting, and the AAO-confined structures notably have no clear melting and the Arrhenius plots can be fit with a single line with a low activation energy. Associated with this latter behavior, the AAO-confined structures have a room-temperature conductivity  $100\times$  that of the bulk polymer-electrolyte.

### **5.2.1 Nyquist plots for AC-impedances for the bulk PEO:LiTf(10:1) polymer electrolyte and confined systems**

Figure 5.2.1 shows the Nyquist plots for AC-impedances for the bulk PEO:LiTf(10:1) polymer electrolyte; figure 5.2.2 shows the PEO:LiTf(10:1) polymer electrolyte confined in 30 nm (a) and 45 nm (b) nanopores in the temperature range  $30^\circ\text{C}$  to  $90^\circ\text{C}$  (only 30, 50, 70,  $90^\circ\text{C}$  are spectra are shown for clarity). Similar plots were made for the 18, 22, 26, 41 and 200 nm pore samples. The diameter of the semi-circle gives the geometric resistance of the electrolyte films.



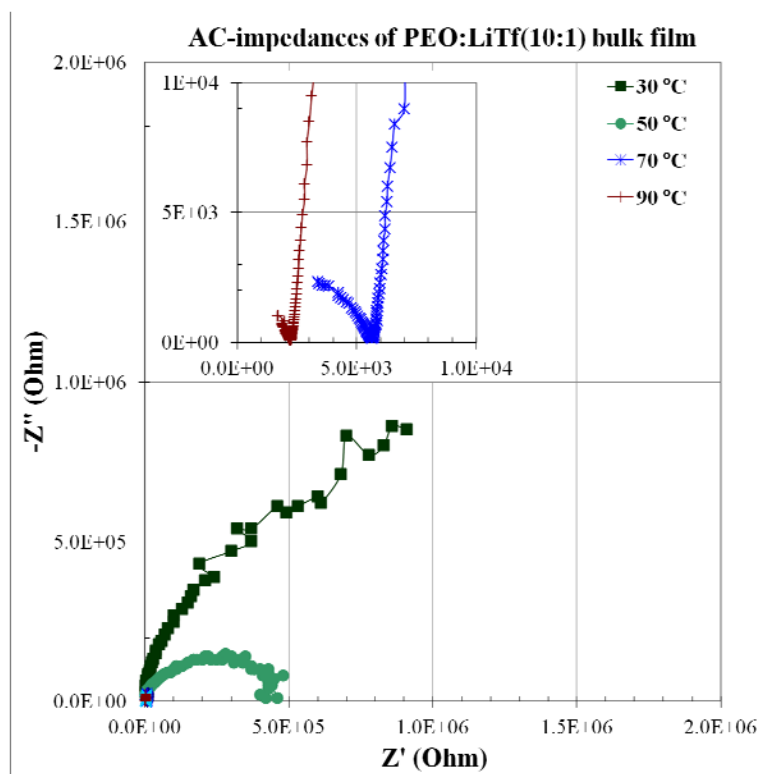


**Figure 5.2.1** Nyquist Plots: for AC-impedances in the frequency range 1 kHz -10 MHz for the bulk PEO:LiTf(10:1) polymer electrolyte for the temperatures 30, 50, 70, and 90 °C, respectively (70 and 90 °C (inset)).

For these geometric resistances, the capacitance values were in the range 1 to 2 pF  $\text{cm}^{-1}$ . For the 30–90 °C temperature range, there are two order-of-magnitude variations in the conductivity. An accurate determination of the diameter is greatly aided by taking the impedance scans throughout this temperature range and carefully observing the trends with temperature. This approach allowed a confident determination of the accurate resistances even when the half-circles are not complete to the origin (at low frequency) or the half-circle does not completely return to the x-axis (at high frequencies). Reproducible data for each temperature indicated that the electrical contact was good.

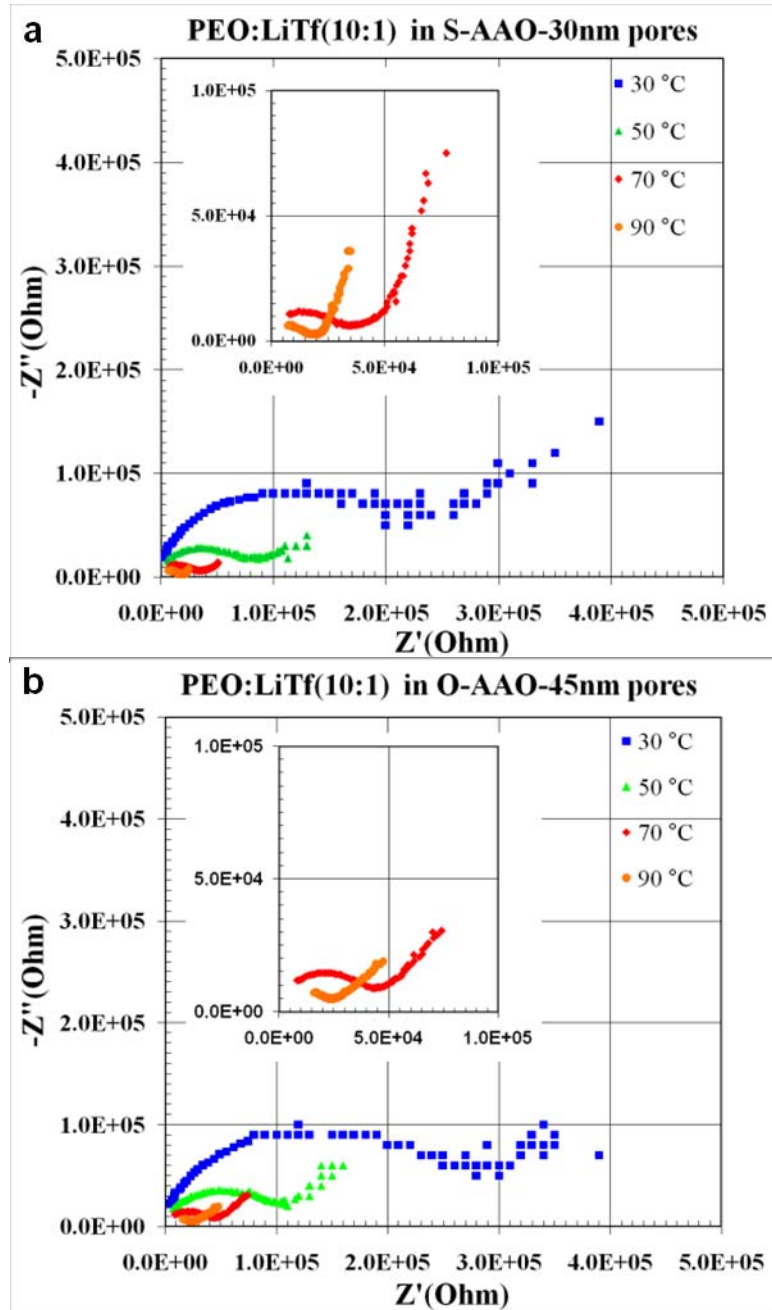


**Figure 5.2.2** Nyquist plots for AC-impedances in the frequency range 1 kHz -10 MHz for the PEO:LiTf(10:1) polymer electrolyte confined in 30nm (a) and 45nm (b) pores for the temperature range 25 – 90 °C, respectively (70 and 90 °C (inset)).

### 5.2.2 Ionic conductivities of bulk PEO:LiTf(10:1) polymer electrolyte and confined systems

All temperature-dependent conductivities of the fabricated films are shown in the Arrhenius plots, see figure 5.2.3. The data for the porous templates is plotted as measured, taking into account the area of the gold contacts (~2 mm diameter) (open), and corrected for the measured porosity of the templates (solid). The porosity was measured using pore diameters and spacing from plan- and cross-sectional-view SEM images, like those shown in figure 3.3. Porosity values are shown in the legend as percent in parentheses. Arrhenius plots for bulk and Anodisc samples show the expected discontinuous behavior associated with melting of the polymer electrolyte, similar to that for the 12:1 reference data [49]. However, data for samples confined in pores less than 50 nm in diameter are linear over the entire 30 to 90 °C temperature range. The activation energy for the bulk [Anodisc] samples is  $51 \pm 0.3$  [ $52 \pm 0.3$ ] kJ/mole for 60 to 90 °C (liquid) and  $107 \pm 0.3$  [ $60 \pm 0.3$ ] kJ/mole for 30-50 °C (solid phase). The activation energies for the AAO confined samples is  $39 \pm 0.2$  kJ/mole for 30-90 °C.

It is remarkable that the ionic conductivity is enhanced by a factor of ~100 in the nanopore-confined electrolyte compared to the solid phase region below the melting temperature of the bulk PEO polymer. The bulk electrolyte film conductivity follows the Arrhenius relation with two activation energies for above and below the melting temperatures of the PEO polymer.

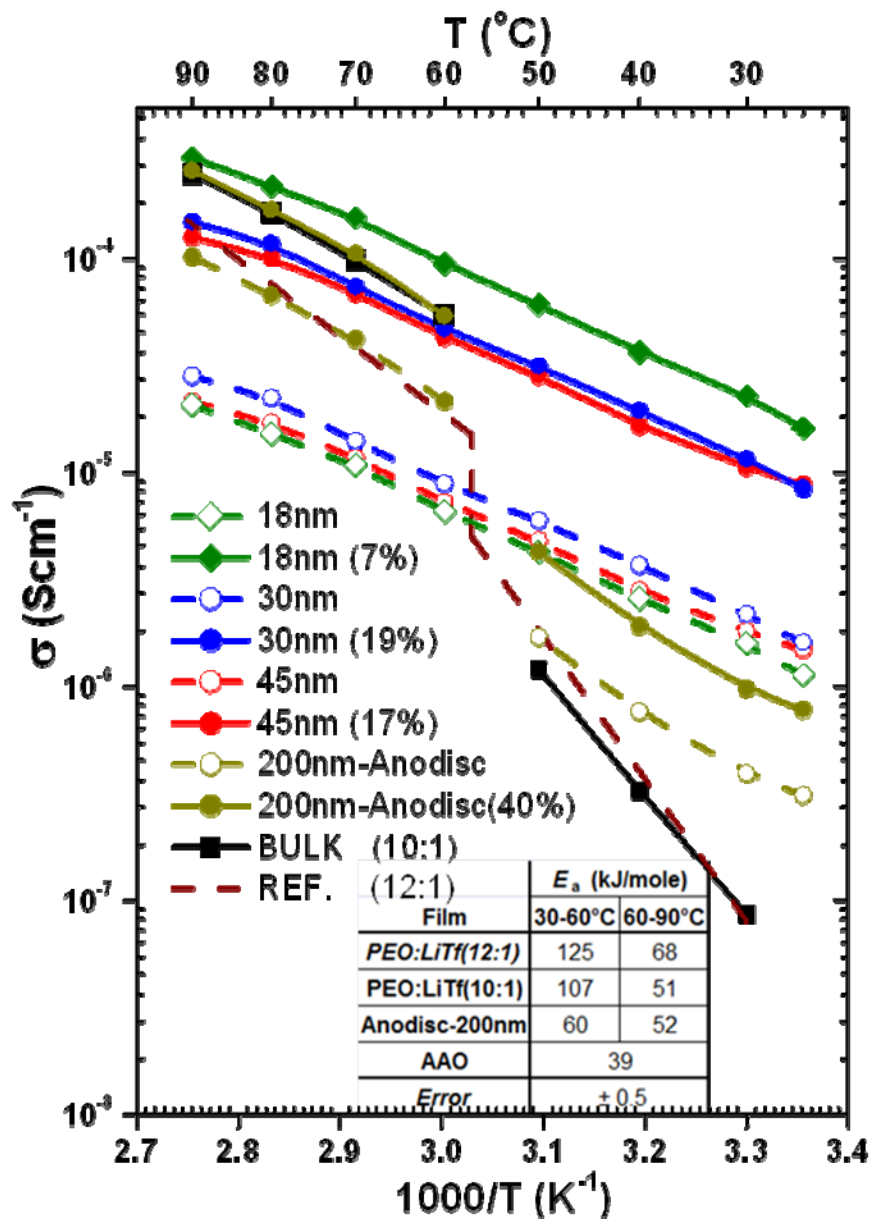


**Figure 5.2.3** Arrhenius plots for the bulk and confined PEO:LiTf(10:1) polymer electrolyte. Bulk and confined in 200 (Anodisc), 45, 30, and 18 nm diameter pores. Open symbols are as measured, solid symbols are normalized for template porosity. A table of activation energies is shown inset.

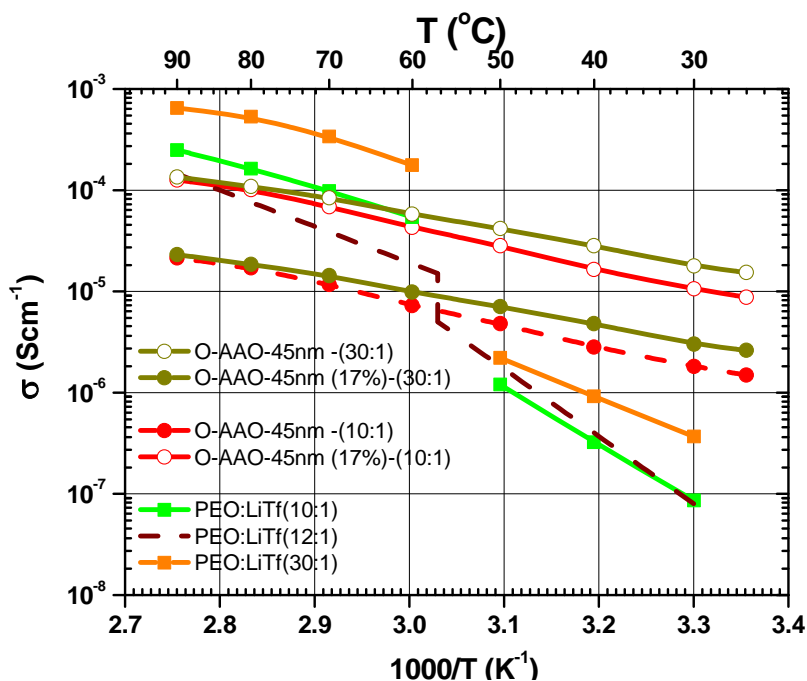


**Figure 5.2.4** Arrhenius plots for the bulk and confined PEO:LiTf(10:1), PEO:LiTf(30:1) polymer electrolytes in 45 nm pores. Solid symbols are as measured, open symbols are normalized for template porosity.

The effect on melting temperature suppression of the confined PEO:LiTf(30:1) polymer electrolyte was also studied for this work. Figure 5.2.4 shows the Arrhenius plots for the PEO:LiTf(30:1) confinement in 45 nm diameter O-AAO pores and compared with the bulk and the PEO:LiTf(10:1) confined in 45 nm O-AAO pores. From this behavior, it can be seen that the ionic conductivity enhancement due to the nanometer scale confinement originates from the ordered polymer chains arrangement induced on the nanoscale which favors ionic conduction.

This significant enhancement of the ionic conductivity indicates that the polymer electrolyte confined in the nanopores undergoes a change in the structural properties of the polymer host material, which opens up non-resistive

ionic transport paths. In general, single Arrhenius behavior for ionic conductivities from ambient temperatures up to higher temperatures is observed in solid amorphous electrolytes. Accordingly, the above semi-crystalline PEO:LiTf(10:1) polymer electrolyte confined in the nanopores appears to have undergone a structural change favor of ionic conduction.

### **5.2.3 Conductance (30 °C) per Pore vs. Pore Diameter**

In this study, it is important to show that the enhancement of the ionic conductivity is not due to surface effects. The low-temperature (30 °C) conductance per pore versus pore diameter is shown in Figure 5.2.5 for the porous samples. Also included are lines modeling the conductance per pore for the conductivity of  $8.6 \times 10^{-8}$  (solid line) and  $9.0 \times 10^{-6}$  (dotted)  $\text{S}\cdot\text{cm}^{-1}$ , representing the conduction associated with the measured conductivity of the pores in a solid or extrapolated for a liquid, respectively. These lines represent uniform conduction over the area (slope 2), whereas the dash-dotted line represents conduction confined to the skin (perimeter) of a pore (slope 1). As shown, this low-temperature conductance per pore for the AAO-confined polymer electrolyte is more than two orders of magnitude greater than that modeled using the measured unconfined low-temperature solid conductivity and remains higher than that modeled using the measured liquid conductivity extrapolated to 30 °C. The line representing uniform conduction over the area is best fit by that for area (slope 2) indicating that this effect is not a skin effect.

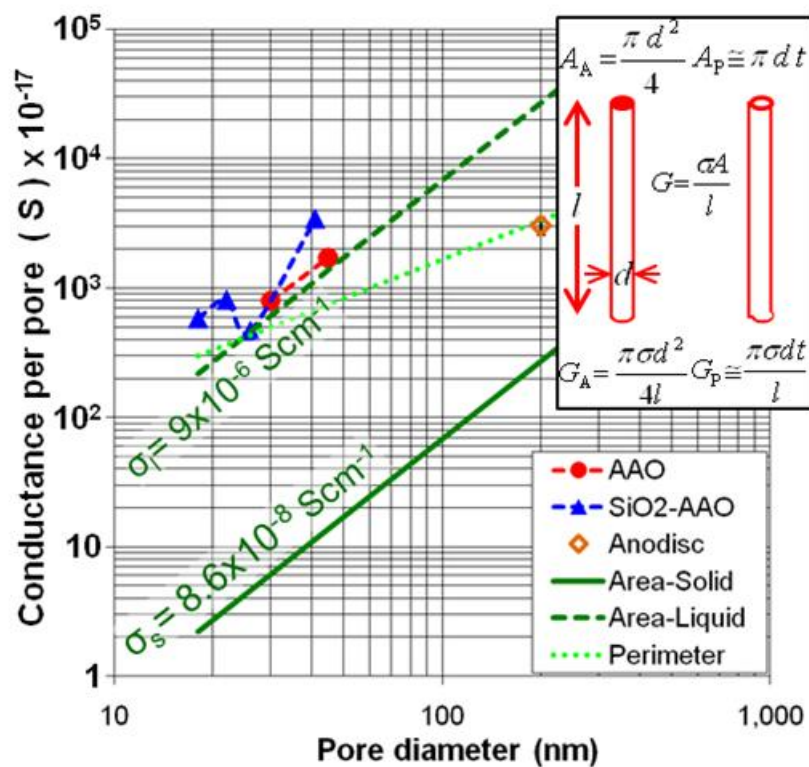


**Figure 5.2.5** Conductance per pore vs. pore diameter for: as-prepared AAO (red circles); SiO<sub>2</sub>-coated AAO (blue triangles); and Anodisc (orange diamond) at 30°C. Also plotted are lines for conductance per pore for conductivity typical of solid PEO:LiTf (10:1) at 30 °C (solid line), for conductivity of liquid PEO:LiTf (10:1) extrapolated to 30°C (dashed), and for conduction only for a constant skin depth around the pore perimeter (dotted). Inset shows diagrams and expressions for conductance,  $G_A$  and  $G_P$ , of a single pore for conduction over the entire cross-sectional area ( $A_A$ ) or a skin depth of thickness  $t$  ( $A_P$ ), respectively; with pore diameter  $d$ , length  $l$ , and conductivity  $\sigma$ .

Finally, it is important to realize that our enhanced conductivity is not simply due to a depressed melting temperature of the confined polymer electrolyte resulting in liquid-like behavior extending to room temperature. The activation energy of our confined electrolyte at low temperature is substantially lower than that of the liquid and similar to that observed for one of the latest synthesized high-conductivity crystalline polymer electrolytes (*e.g.* 44 kJ/mole for

P(EO)<sub>8</sub>:NaAsF<sub>6</sub>) [34], with channels deduced from x-ray measurements. Our low activation energy persists even at temperatures well above the usual polymer electrolyte melting temperature. This indicates that not only are ordered chains aligned in the pore direction at room temperature, this ordering persists to 90 °C (30 °C above the usual melting temperature and about 20 °C above the equilibrium melting temperature [121,122]). Even at such high temperatures, the conductivity involves the ordered chains rather than only being facilitated by the local segmental motion in the usual liquid-like conduction. In some ways, our confined electrolyte polymer is behaving more like a liquid crystal, with aligned channels, which result in our observed enhanced conductivity.

### **5.3 Analysis of FTIR and Raman spectra**

In this section, the FTIR and Raman spectra for the bulk and confined PEO and PEO:LiTf(10:1) samples are presented. A lot of spectra were taken and carefully analyzed. Ultimately, because of a shorter-chain polymer was used, it is difficult to assess the polymer alignment within our confined structures; however the data is consistent with alignment of the polymer chain with the pore direction.

From the X-ray analysis, pure PEO<sub>3400MW</sub> consists of crystalline and amorphous phases, while PEO:LiTf(10:1) is more complex with crystalline phases of both the pure PEO and the 3:1 PEO:LiTf compound [49]. The vibrational modes of both pure PEO and the 3:1 crystalline PEO:LiTf compound P(EO)<sub>3</sub>:LiTf are usually described in terms of a infinite, perfect, helical chain



[118]. The pure PEO vibrations are characterized by the  $D(4\pi/7)$  factor group and those of crystalline  $P(\text{EO})_3:\text{LiTf}$  in terms of the  $C(2\pi/2)$  factor group (see appendix 1 for character tables) [119]. Therefore, it is easy to assign the transition moments of the various normal modes as either perpendicular or parallel to the chain axis. However, in this work a low molecular weight polymer ( $\text{PEO}_{3400\text{MW}}$ ) with approximately 76 repeat units in a chain was used to confine in the nanopores. Considering this, it is difficult to draw conclusions about polymer chain alignment confined to the nanoscale on the vibrational spectroscopic data of short chain polymers.

Figure 5.3.1 shows spectra of the  $\text{PEO}_{3400\text{MW}}$  polymer and  $\text{PEO}:\text{LiTf}(10:1)$  electrolyte bulk films and those films confined in 18, 26, 30, 41, 45 nm and 200 nm diameter pores for the spectral region  $4000\text{-}1200\text{ cm}^{-1}$ . The broad peak at frequency  $3445\text{ cm}^{-1}$  in the bulk films is due to the O-H stretching of OH end groups of the polymer. This peak appears with less intensity in confined systems probably due to the combination of OH stretching of both the polymer and the OH bonded to the surface of the AAO. The relative absorbance intensity of the OH stretch in the AAO samples is very low since they were annealed at  $1000\text{ }^\circ\text{C}$  in dry nitrogen and the spectra were taken in moisture free conditions. According to the normal coordinate treatment and factor-group analysis [117], the  $\text{CH}_2$  stretching vibrations results in two parallel bands with  $A_2$  symmetry and four perpendicular bands with  $E_1$  symmetry. According to this assignment, for an infinitely long PEO chain polymer, these parallel modes appear at  $2888\text{ cm}^{-1}$  and

2859  $\text{cm}^{-1}$  and normal bands appear at 2885  $\text{cm}^{-1}$  with shoulder bands at 2945, 2825 and 2805  $\text{cm}^{-1}$ . However these bands are not distinctive due to the weak intensity and complicated broadness of the peak around 2880  $\text{cm}^{-1}$  in this region, especially when unpolarized light is used.

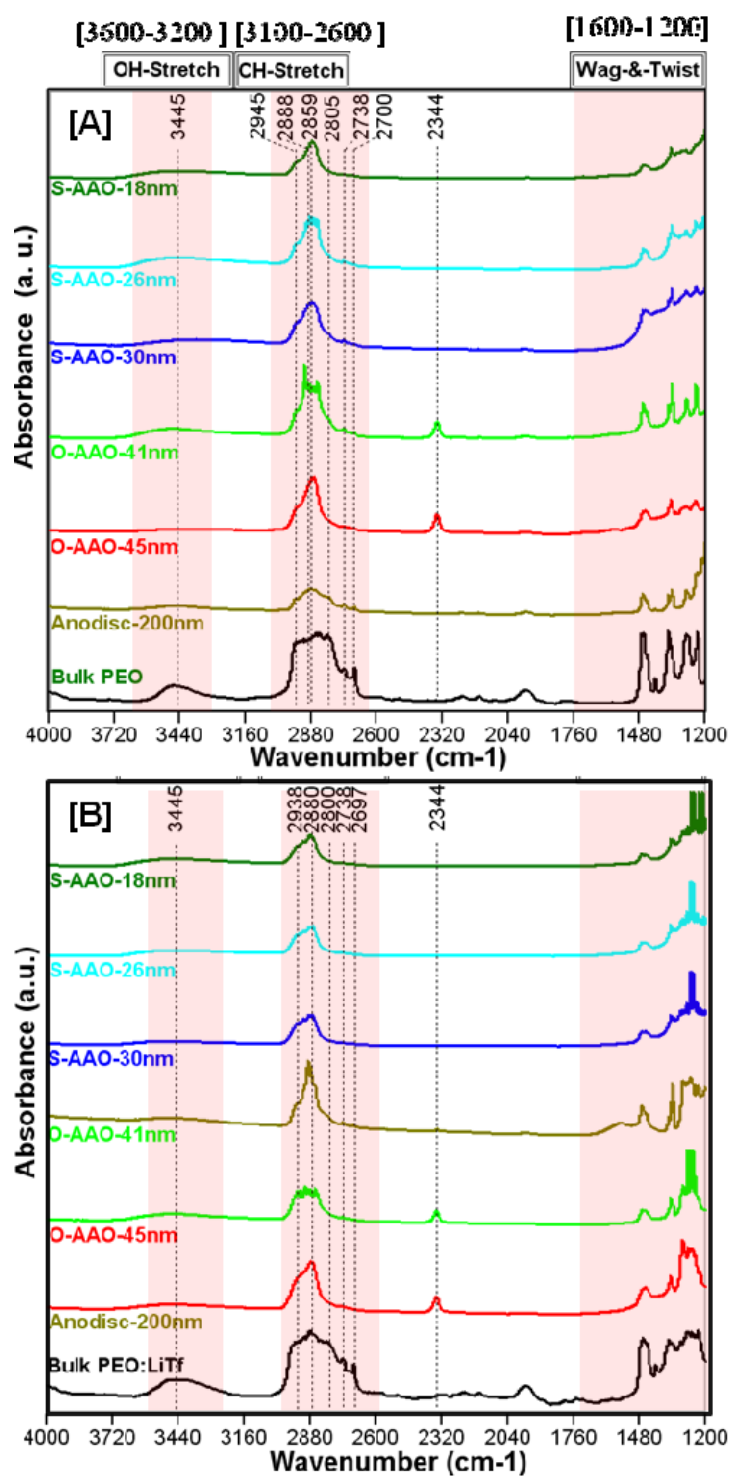


**Figure 5.3.1** FTIR spectra (4000-1200 cm<sup>-1</sup>) of PEO [A] and PEO:LiTf(10:1) [B] bulk films and confined in: Anodisc (200 nm), 45nm pores O-AAO, 30nm pores S-AAO, 41, 26, 18 nm pores coated with SiO<sub>2</sub> layers on S- and O-AAO pores respectively.

In figures 5.3.1 spectra were taken using unpolarized IR and the CH<sub>2</sub> stretching modes from parallel and perpendicular bands overlap except for the overtone frequencies at 2738 (parallel) and 2700 (perpendicular) cm<sup>-1</sup> in the bulk films. Nevertheless, this complex CH<sub>2</sub> broad band begins to be resolved when the polymer is confined in the nanopores. The band at 2885 cm<sup>-1</sup> is attributed to a vibration where transition moment is perpendicular to the chain axis. Besides this assignment, we can observe that the 2945 and 2805 cm<sup>-1</sup> peaks are distinctive in the nanopore spectra, indicating that the confined polymer responds to the perpendicular electric field of the IR beam propagating along the pore axes. However, the overtone peak intensities at 2738 and 2700 cm<sup>-1</sup> disappeared in PEO:LiTf(10:1) confined systems, although these bands have a fair amount of intensity in the pure PEO confined samples.

The polymer peaks below the 1200 cm<sup>-1</sup> region are not observable due to the interference with the strong Al-O vibrational modes in the template structure, whereas the vibrational modes in the spectral region from 1420 to 1220 cm<sup>-1</sup> are seen in figure 5.3.2 and discussed in detail.

The vibrations from 1420 to 1220 cm<sup>-1</sup> contain modes that are primarily a mixture of CH<sub>2</sub> wagging and CH<sub>2</sub> twisting motions. In this spectral region, the bands of the pure PEO are more clearly resolved in the bulk sample (Figure 5.3.2[A]), with a stronger band 1360 cm<sup>-1</sup> and a weaker band at 1343 cm<sup>-1</sup>. It is remarkable to note that these intensities are reversed in the Anodisc spectrum, in sharp contrast to the behavior observed in the P(EO)<sub>3</sub>:LiTf spectra. The transition

moment of the doubly degenerate mode underlying the  $1360\text{ cm}^{-1}$  band is perpendicular to the chain direction in an infinite, helical chain; consequently, the mode would be observed in all chain orientations. In the spectrum of the 45 nm diameter nanopore sample, the intensity of the band at  $1343\text{ cm}^{-1}$  relative to the  $1360\text{ cm}^{-1}$  band increases even more than in the Anodisc; this relative increase appears to be preserved in all other nanopore spectra.

Further analysis of this spectral region reveals that the characteristic crystalline peak at  $1280\text{ cm}^{-1}$  in bulk films due to  $\text{CH}_2$  twisting shows up in all the pore samples. The  $1234\text{ cm}^{-1}$  peak intensity with a shoulder band at  $1241\text{ cm}^{-1}$  dominates in the Anodisc samples, while at this intensity disappears in the nanopores samples. This peak disappearance causes the  $1241\text{ cm}^{-1}$  peak to dominate in the nanopore samples. The absorbance at frequency  $1370\text{ cm}^{-1}$  is almost insignificant in the confined system while the strong peak due to the wagging vibrations at  $1413\text{ cm}^{-1}$  completely vanishes or the absorbance is not significant in the confined systems.

In the PEO:LiTf spectra, (figure 5.3.2[B]), there is a broad feature from about  $1330$  to  $1370\text{ cm}^{-1}$  in the bulk sample which is resolved in the Anodisc spectrum into distinct bands at  $1360$ ,  $1350$ , and  $1343\text{ cm}^{-1}$ . However, the strong  $1343\text{ cm}^{-1}$  band essentially disappears in the 45 nm sample and all other nanopore samples. The marked intensity decrease is consistent with an alignment of the polymer chains parallel to the pore direction, since the transition moment of the mode is parallel to the polymer chain axis (in an infinite helical chain).

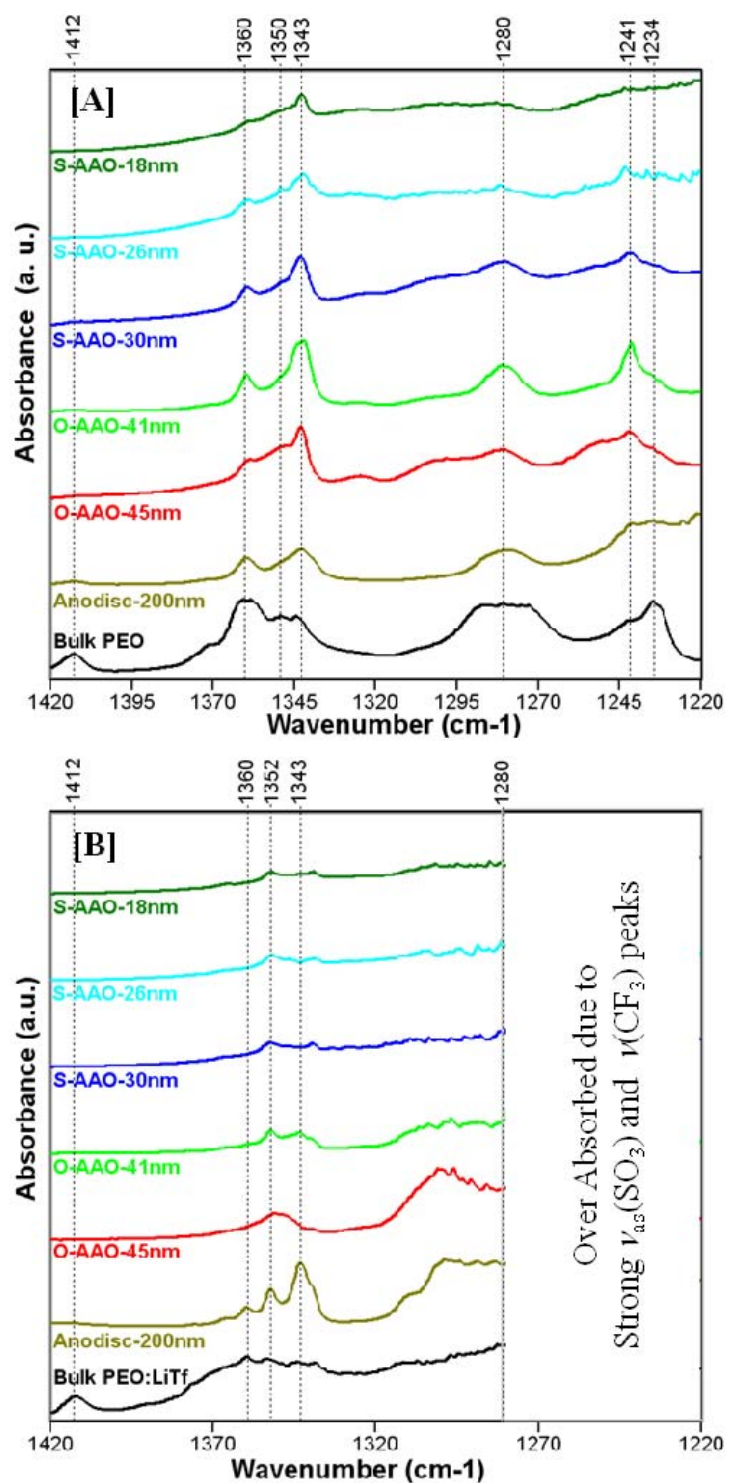


**Figure 5.3.2** FTIR spectra (1420-1220 cm<sup>-1</sup>) of PEO [A] and PEO:LiTf(10:1) [B] bulk films and confined in: Anodisc (200 nm), 45nm pores O-AAO, 30nm pores S-AAO, 41, 26, 18 nm pores coated with SiO<sub>2</sub> layers on S- and O-AAO pores respectively.

This conclusion follows from the propagation of the IR beam in the direction of the pore axis in all spectral measurements in this study. The weak intensity of the  $1352\text{ cm}^{-1}$  band (assigned to the amorphous PEO phase) is barely detectable in the nanopore spectra, consistent with an increased degree of crystallinity in the pores relative to the Anodisc. The weak  $1360\text{ cm}^{-1}$  band in the Anodisc spectrum disappears in the nanopore spectra.

Remembering that the IR beam propagates in the direction of the pore axis in all spectral measurements in this study there are at least two possible explanations for these observations. First, the deviation from a perfect helical chain structure is greater in PEO than in the  $\text{P(EO)}_3\text{:LiTf}$  compound, with the consequence that the directions of transition moments are not strictly parallel or perpendicular to the chain direction. Second, in the Anodisc, there appears to be a slight but measureable preferential orientation of the pure polymer perpendicular to the pore axis, and this preferential orientation seems to be preserved in all nanopore samples.

Figure 5.3.3 shows the Raman spectra of PEO and  $\text{PEO:LiTf(10:1)}$  bulk polymer materials and confined in the nanopores. The relative vibrational peak intensities of PEO and  $\text{PEO:LiTf(10:1)}$  confined in AAO nanopore systems compared to the bulk PEO and  $\text{PEO:LiTf(10:1)}$  films are very low and appear on the AAO characteristic fluorescence background spectrum. The Raman spectra of nanopore templates are shown in appendix 1. The regional magnifications of the spectra are needed to carry out the spectral peak analysis.

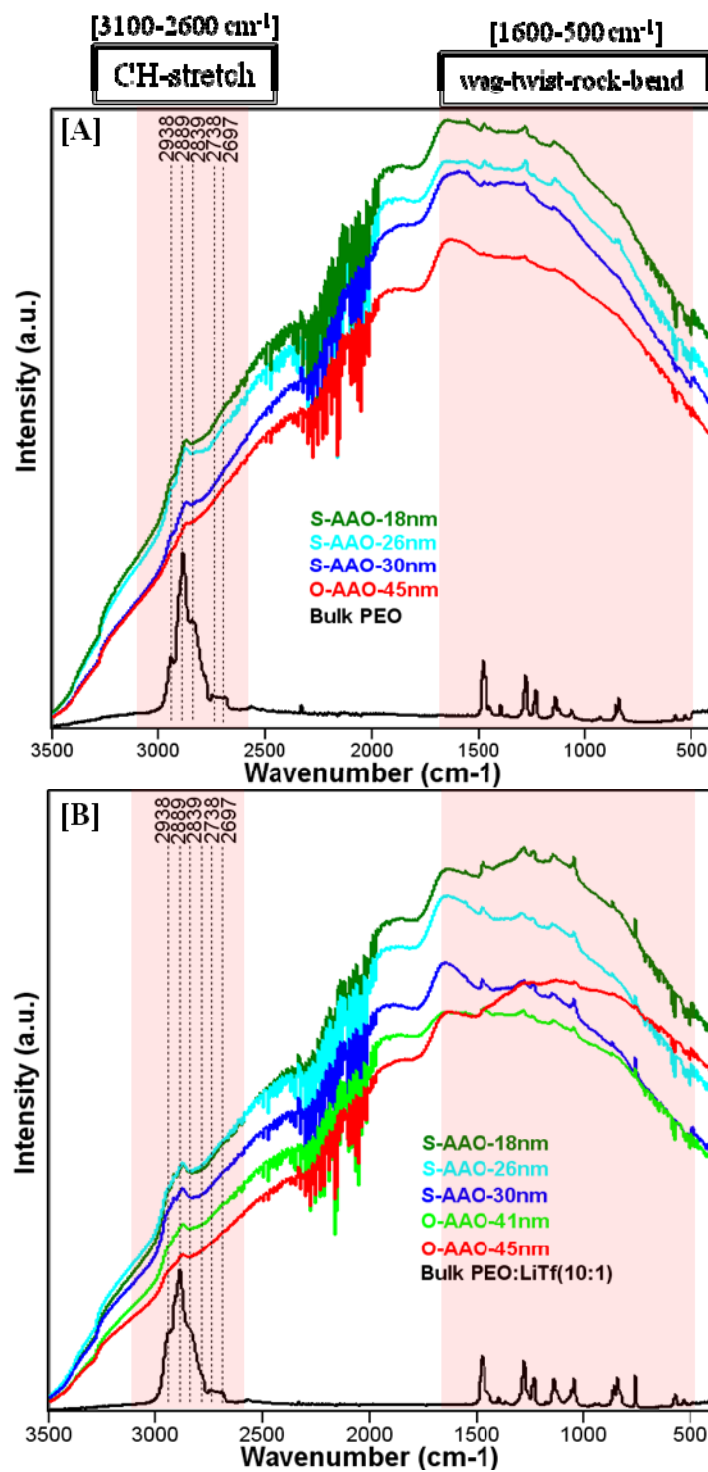


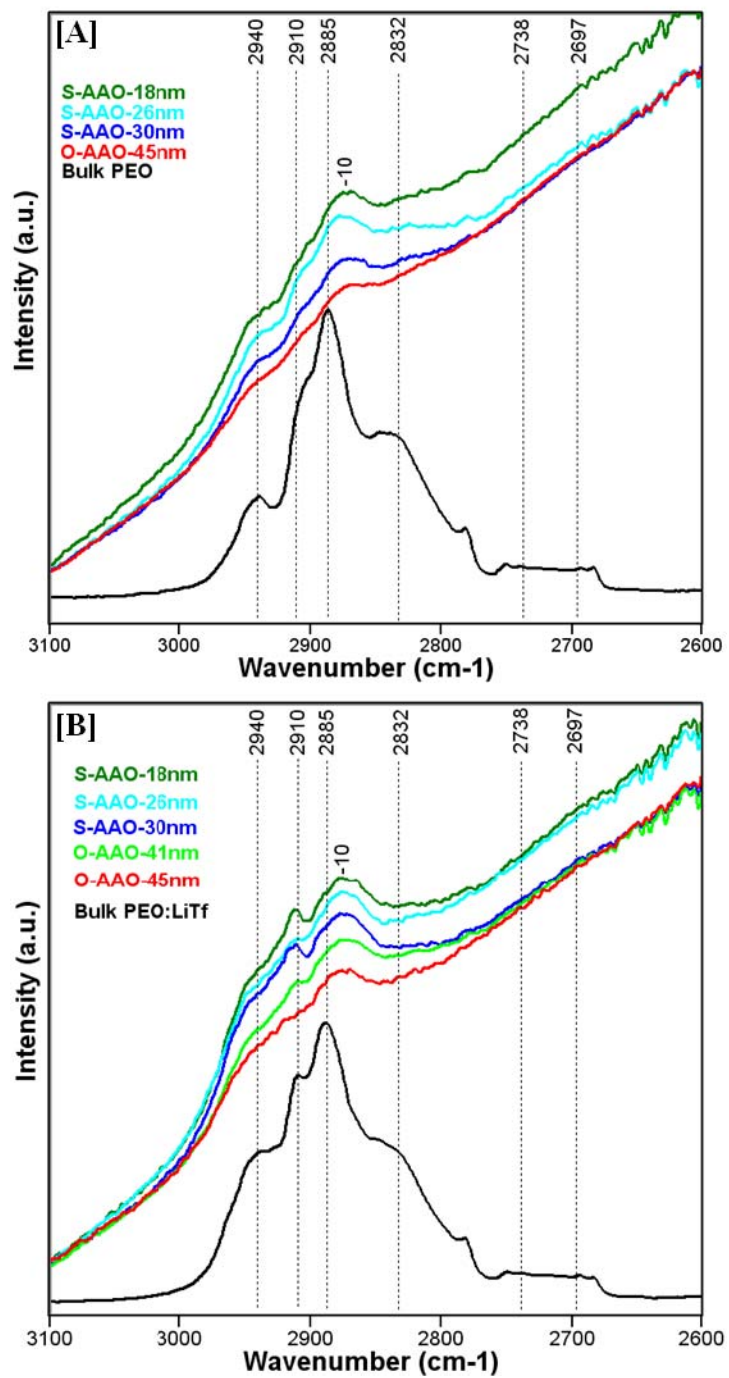
**Figure 5.3.3** Raman spectra in the spectral region (3500-400) cm<sup>-1</sup> for PEO [A] and PEO:LiTf(10:1) [B] polymer bulk films and those films confined in 18, 26, 30, 45nm pores.



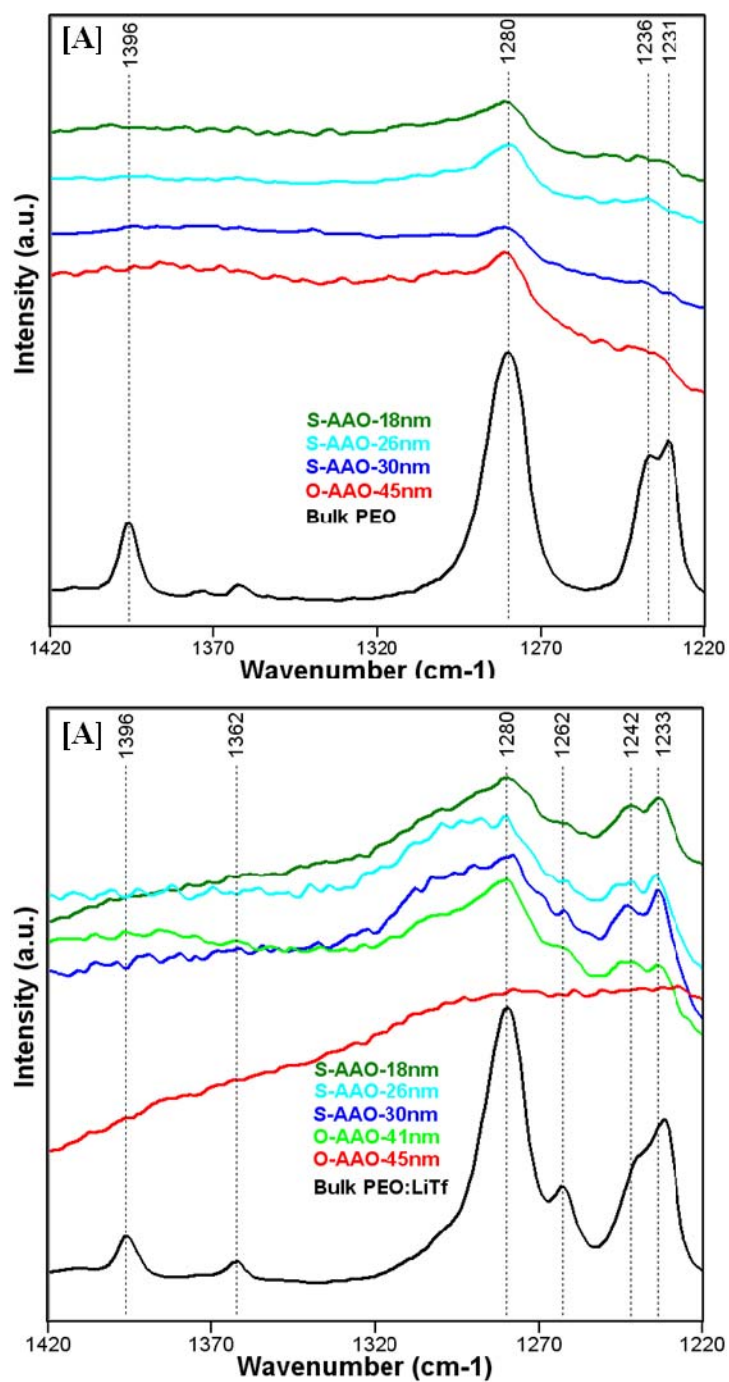
Comparing with the FTIR spectra, the Raman spectra of bulk films show a broad intensity band of the CH<sub>2</sub> stretching mode centered at 2889 cm<sup>-1</sup> and shoulder peaks at 2938 cm<sup>-1</sup> and 2839 cm<sup>-1</sup> as shown in figures 5.3.4. However, all these peaks merge and make a broad, very low intensity peak in the AAO template spectrum. The overtone peak intensities at 2738 and 2697 cm<sup>-1</sup> are insignificant in the polymer -confined template systems.

Figure 5.3.5[A] shows the Raman spectra in the region 1420-1220 cm<sup>-1</sup> for the bulk and confined PEO. In the pure bulk PEO spectra, the peaks at 1231, 1236 and 1280 cm<sup>-1</sup> are due to a mixture of  $\tau_s(\text{CH}_2)$  and  $\tau_{as}(\text{CH}_2)$  vibrations that dominate the characteristic modes of the crystalline phase. Comparing with PEO:LiTf(10:1) in figure 5.3.5[B], the peak at 1280 cm<sup>-1</sup> indicates that the bulk phase in PEO:LiTf(10:1) sample is composed primarily of crystalline PEO.

The peaks at 1231 and 1236 cm<sup>-1</sup> have moved to 1233 and 1242 cm<sup>-1</sup> in the PEO:LiTf(10:1) material. The peak at 1263 cm<sup>-1</sup> in PEO:LiTf(10:1) is due to the antisymmetric SO<sub>3</sub> stretching vibrations, where the intensities are much smaller in the confined systems with no peak shifting. The peak at 1396 cm<sup>-1</sup> in the spectra of both bulk films is due to a mixture of CH<sub>2</sub> wagging and C-C stretching vibrations: The intensities of these vibrations are almost vanish or are insignificant in the confined nano pore spectra, where this IR spectral frequency is 1412 cm<sup>-1</sup>. The  $\tau(\text{CH}_2)$  mode has bands at 1231 and 1236 cm<sup>-1</sup> in the bulk phase that show a dramatic intensity reduction in the confined systems, indicating that the PEO undergoes a structural change in the nanopores.



**Figure 5.3.4** Raman spectra in the spectral region (3100-2600) cm<sup>-1</sup> for PEO [A] and PEO:LiTf(10:1) polymer bulk films and those films confined in 18, 26, 30, 45nm pores.



**Figure 5.3.5** Raman spectra in the spectral region (1420-1220) cm<sup>-1</sup> for PEO [A] and PEO:LiTf(10:1) [B] polymer bulk films and those confined in 18, 26, 30, 45nm pores.

Figure 5.3.6 shows the bending and rocking vibrational frequencies. The peak at  $761\text{ cm}^{-1}$  is due to the symmetric bending deformation of  $\text{CF}_3$ ,  $\delta_s(\text{CF}_3)$ , of the  $\text{CF}_3\text{SO}_3^-$  ion associated with  $\text{Li}^+$ . The spectral observation at  $761\text{ cm}^{-1}$  of PEO:LiTf(10:1) bulk film and the confined systems show that the ionic association in PEO:LiTf(10:1) polymer electrolytes is not affected by confinement in the nanopores. Peaks at  $831$ ,  $844$  and  $860\text{ cm}^{-1}$  are primarily  $\text{CH}_2$  asymmetric rocking vibrations,  $\rho_{\text{as}}(\text{CH}_2)$ , of the pure polymer backbone in the crystalline phase. The frequencies of the bands in figure 5.3.6 do not shift but the weak intensities are only slightly above the nanopore template background. In figure 5.3.6 [B] the pure PEO crystalline peaks still appear in the bulk PEO:LiTf(10:1) electrolyte and the electrolyte confined in the nanopores, which indicates that the intensities of the peaks at  $844$  and  $860\text{ cm}^{-1}$  are very low and the crystalline PEO chains still dominate in the confined systems. The peak at  $870\text{ cm}^{-1}$  in the PEO:LiTf(10:1) electrolyte is due to the  $\rho_{\text{as}}(\text{CH}_2)$  of O-C-C-O torsional vibrations and originates in the O:Li(3:1) crystallite domains.

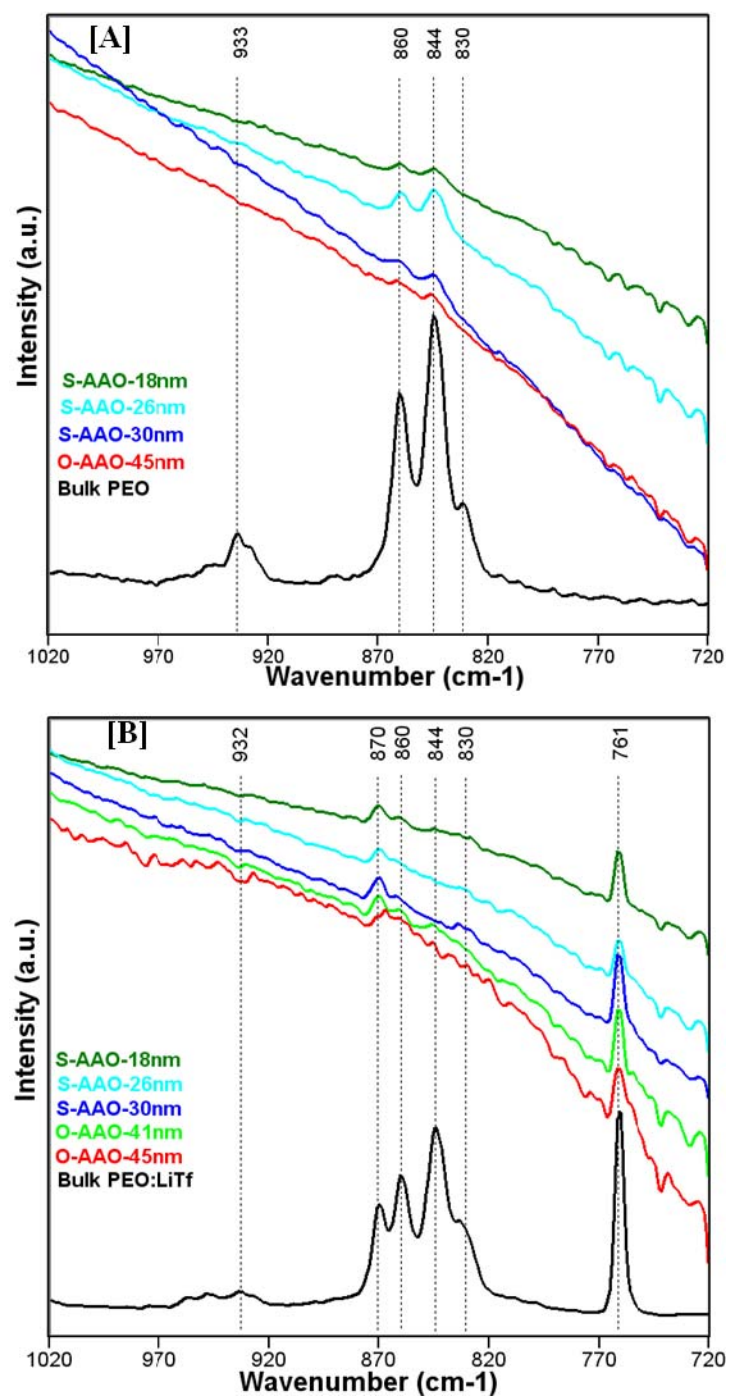


**Figure 5.3.6** Raman spectra in the spectral region (950-750) cm<sup>-1</sup> for PEO [A] and PEO:LiTf(10:1) polymer bulk films and those confined in 18, 26, 30, 41, and 45nm pores.

#### 5.4 WAXS patterns and structural analysis

In this x-ray section, the WAXS patterns are presented and discussed. In short, the WAXS patterns of the bulk and Anodisc samples showed the usual random polycrystalline order. For the PEO-confined structures, the initial on-axis WAXS patterns showed little crystalline polymer material, however, when they were tilted at  $10^\circ$  to look for alignment of the polymer chain with the pore axes, the diffraction peaks associated with the appropriate planes strongly diffracted showing the azimuthal pattern expected for polymer chains aligned with the pore axis. The same result was observed for the PEO:LiTf(10:1) confined in the AAO.

The WAXS patterns for PEO and PEO:LiTf bulk samples are shown in figure 5.4.1. These bulk samples show the azimuthal symmetry expected of a random polycrystalline polymer.

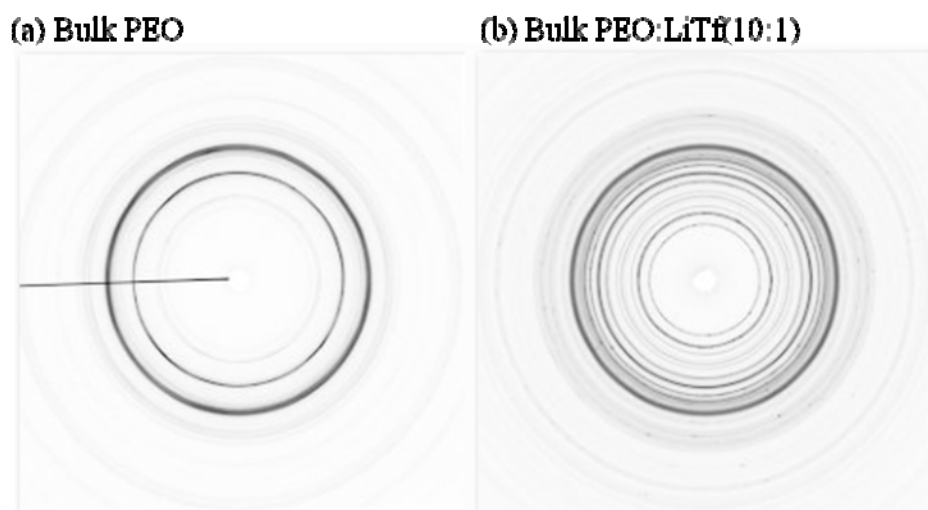


**Figure 5.4.1** WAXS patterns of bulk PEO (a) and PEO:LiTf(10:1) (b).

The corresponding intensity versus two theta profiles taken from line cuts at  $\psi=0$  are shown in figure 5.4.2. In this study, the strongest PEO peaks at  $2\theta=19.2^\circ$  from the (120) plane and  $23^\circ$  from multiple (hk2) and (hk4) planes are analyzed.

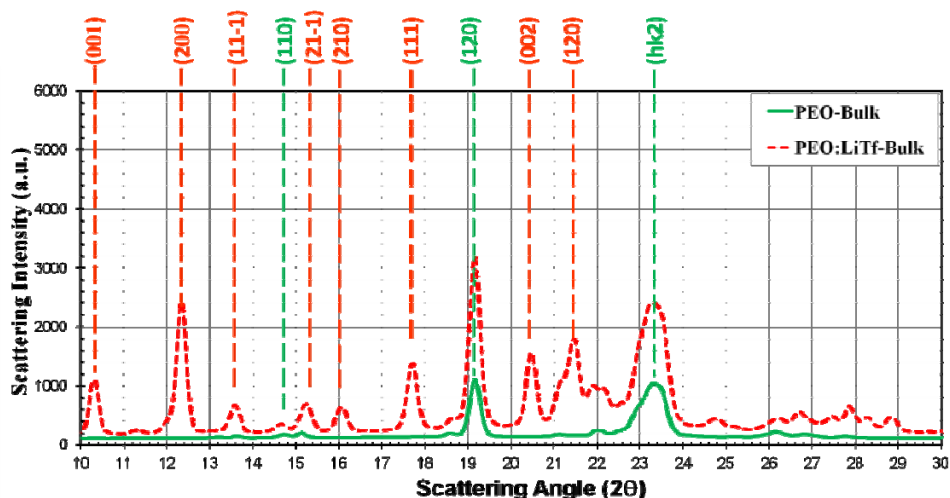


**Figure 5.4.2** Intensity versus  $2\theta$  profiles of bulk PEO (green) and PEO:LiTf(10:1) (red).

Figure 5.4.3 shows the Ewald constructions for the PEO plane reflections when the c-axis of the polymer chains are parallel and tilted  $10^\circ$  to the x-ray beam. The d-spacings and reflection angles for both PEO and the  $P(\text{EO})_3\text{:LiTf}$  crystal plane reflections were calculated using the equation for a monoclinic lattice system (see Appendix 2 for equation and the tables, Table A2.1 and Table A2.2). These d-spacings are very important in the evaluation of the crystal structure.

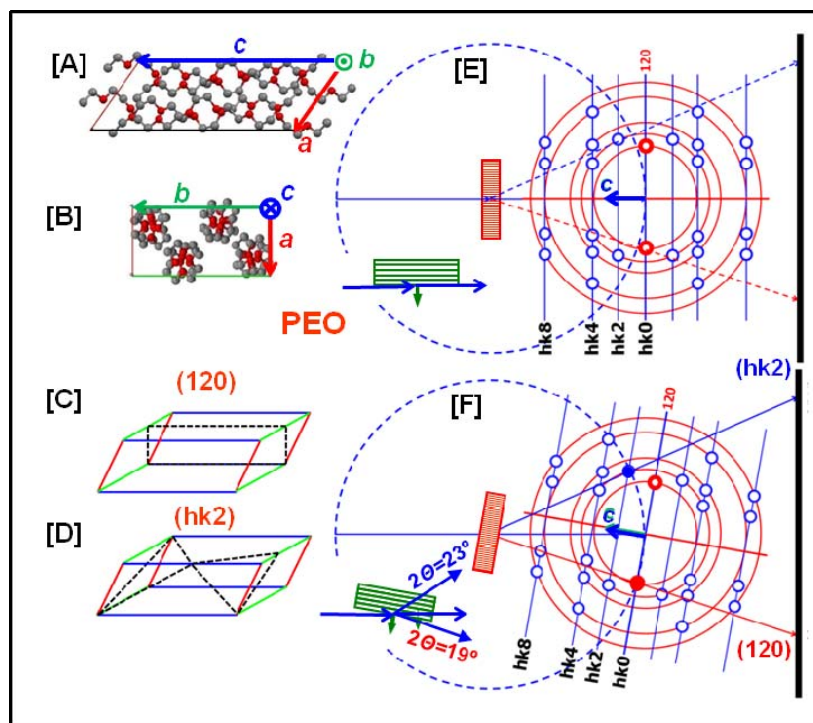


**Figure 5.4.3** Ewald constructions of untitled [E] and 10° tilted [F] PEO. Inset figure [A] is showing the PEO crystal looking through the b-axis and inset [B] shows the PEO crystal looking through the c-axis. [C] and [D] show the (120) and (*hkl*) planes in the lattice.

It is important to compare and analyze the WAXS patterns of PEO and PEO:LiTf-filled and empty nanopore templates to the bulk PEO and PEO:LiTf (figure 5.4.4). All of these WAXS patterns were taken with the x-ray beam normal to the sample surface where the template pore axes are parallel to the beam.



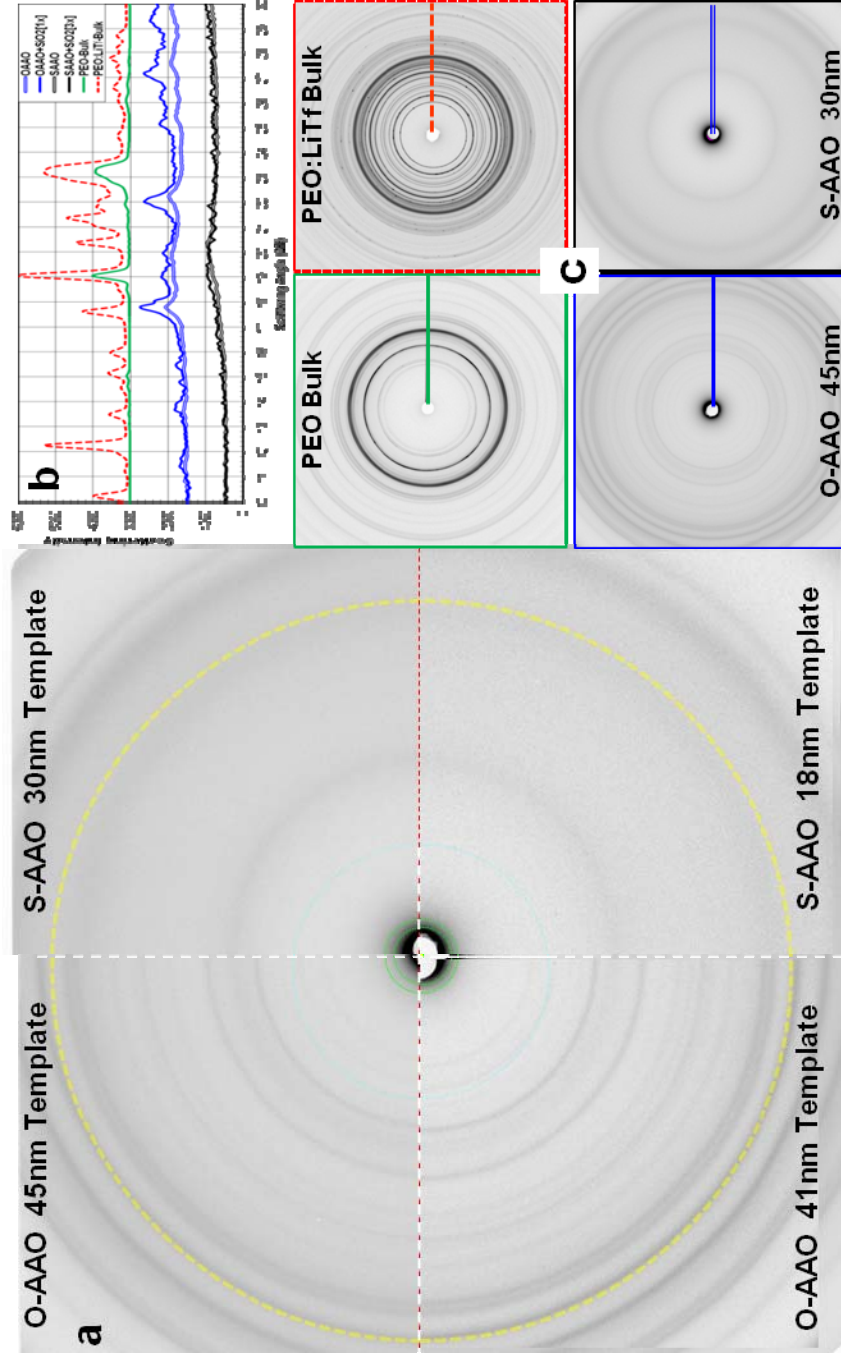


**Figure 5.4.4** WAXS of empty pores and bulk PEO and PEO:LiTf a) WAXS pattern of coated and uncoated AAO, as labeled. b) Line profiles from WAXS patterns of various bulk PEO and PEO:LiTf and PEO-filled AAO and empty AAO. c) WAXS patterns for bulk PEO and PEO:LiTf and empty AAO, as labeled.

As shown in the figures 5.4.4(a.b.c), the WAXS patterns of the PEO-filled AAO samples are very different from the bulk PEO sample. In the WAXS patterns of the PEO-filled AAO samples, with templates porosity taken into account, the intensities of the prominent  $19.2^\circ$  and  $23^\circ$  peaks are much reduced compared to the bulk (figure 5.4.4(b)). This indicates the confined polymer morphology is very different in the AAO pores. The reduced intensities can be due to a reduced amount of the crystalline phase or preferred orientation. To test these two possibilities we oriented the PEO-filled nano pore samples at  $10^\circ$  ( $\sim 19.2^\circ/2$ ) in anticipation of the polymers partly aligning along the pore direction. WAXS patterns taken in this sample orientation showed pronounced peaks for  $19.2^\circ$  and  $23^\circ$  reflections as expected. Comparison of WAXS patterns of untilted and 10 degree tilted PEO-filled S-AAO-30nm pore sample along with empty pore template and PEO bulk film WAXS patterns are shown in the figure 5.4.5. Figure 5.4.6 summarizes this situation where this effect for the 30nm pore diameters is most pronounced while the 45 nm diameter pore sample shows less effect. (WAXS patterns of untilted and 10 degree tilted PEO-filled O-AAO-45nm pore sample are shown in figure A2.1, Appendix 2).

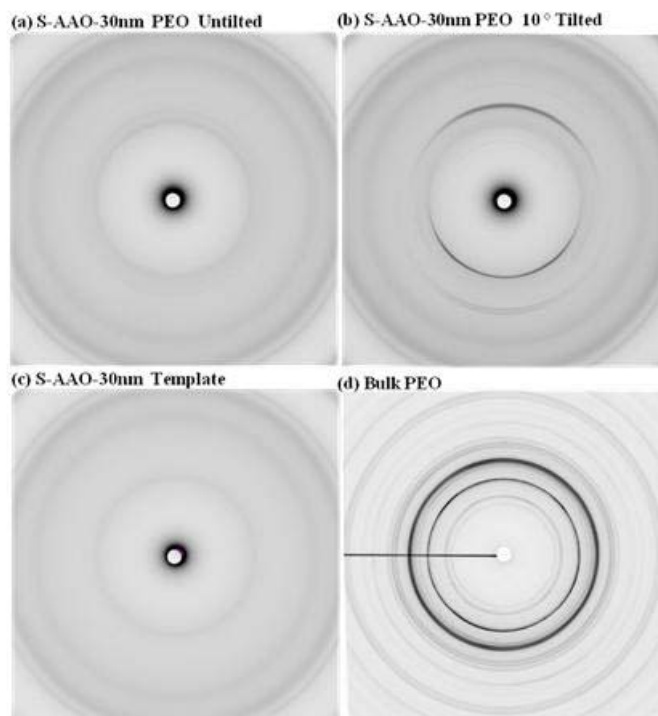


**Figure 5.4.5** WAXS patterns for unilted PEO filled 30 nm pores (a), 10° tilted PEO filled 30 nm pores (b), S-AAO-30nm template (c), Bulk PEO (d).

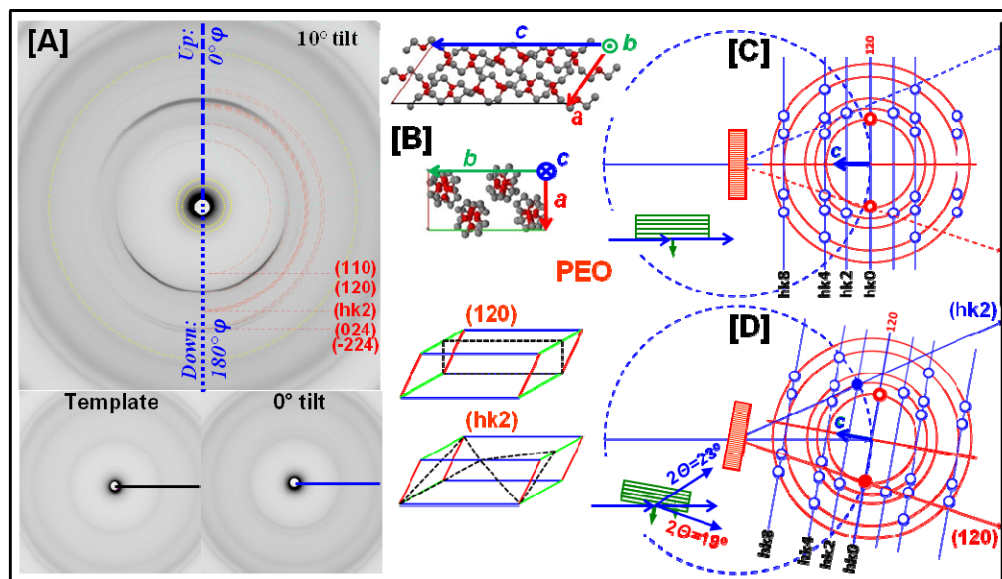


**Figure 5.4.6** WAXS patterns for 10° tilted PEO filled 30 nm pores (top), template (bottom left), and unilted PEO filled 30 nm pores (bottom right) [A]. View of PEO crystal looking through b and c axes [B]. Ewald constructions of unilted [C] and 10° tilted [D] orientations.

Intensity versus two theta profiles are plotted as shown in figure 5.4.7 to quantitatively show the (120) and (hk2) peak intensities enhancements (intensities are corrected for porosity). The (120) peak is prominent in the 10°-tilt lower ( $\varphi=180^\circ$ ) line cut profile and not present in the upper ( $\varphi=0^\circ$ ) line cut profile and less than 1/10 (1/4) the size in the 0°-tilt (bulk PEO) line profile.

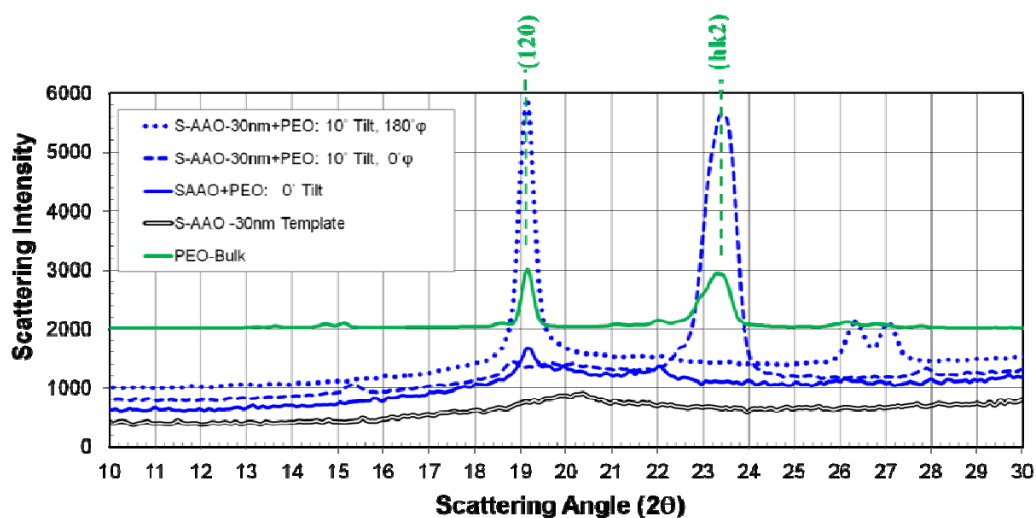


**Figure 5.4.7** Intensity versus two theta profiles for PEO in 30 nm pores 10° tilted and untilted.

The Ewald constructions for the 0° and 10° tilt angles are shown in figure 5.4.6[C & D] which illustrates the behavior of the (120) peak. Here, the Ewald construction is for the PEO *c*-axis (polymer chain axis) directed along the pore axis. For the 0° tilt construction, the (120) and (hk2) reciprocal lattice points are not on the Ewald sphere (so there is no diffraction) and for the 10° tilt the (120), by design, and the (hk2) points are on the sphere resulting in strong diffraction. This indicates that the PEO polymer is ordered in the nano pores with the chain

direction (*c*-axis) aligned with the pore and an inter-chain separation equivalent to that of the crystal (the (120) planes are parallel to the *c*-axis).

PEO chains alignment in the nano pore scale is not surprising, given that simulations of confined polymers in pores with minimal interaction (“slippery-walls” -reflecting neutral repulsion of the walls) predict the chain axis aligned to the walls [113]. Although for the other AAO pore diameters, the 10° tilt WAXS patterns do not show as strong (120) diffraction peaks. This means the polymer chains are not in crystalline registry in these pores. However, it is likely that the simulations of Ma *et al.* support the conclusion that the polymer chains are aligned in the pore.

The situation is more complicated, but similar, for PEO:LiTf(10:1). Again the WAXS patterns of the PEO:LiTf(10:1)-filled AAO samples are very different than for the bulk PEO:LiTf(10:1) sample (and the PEO:LiTf(10:1)-filled Anodisc sample), see figure 5.4.8 (WAXS patterns of untilted and 10 degree tilted PEO:LiTf(10:1)-filled O-AAO-45nm pore sample are shown in figure A2.2, Appendix 2). In the WAXS patterns of the samples taken at in the usual normal orientation (tilt= 0°), with porosity taken into account, the prominent PEO and P(EO)<sub>3</sub>:LiTf peak intensities are much reduced compared to the bulk. Again as mentioned earlier, this indicates that the confined polymer electrolyte morphology is very different in the AAO pores. So that in anticipation of polymers aligning in the pore direction, we oriented the PEO:LiTf-filled samples at 10° (~19.2°/2) and we see the WAXS patterns have very different azimuthal symmetry.

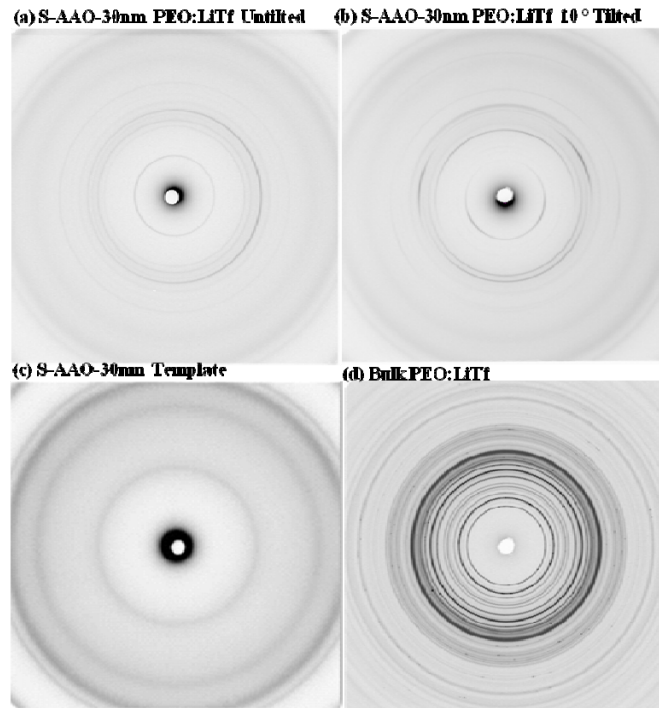


**Figure 5.4.8** WAXS patterns for untitled PEO:LiTf(10:1) filled 30 nm pores (a), 10° tilted PEO:LiTf(10:1) filled 30 nm pores (b), S-AAO-30 nm template (c), Bulk PEO:LiTf(10:1) (d).

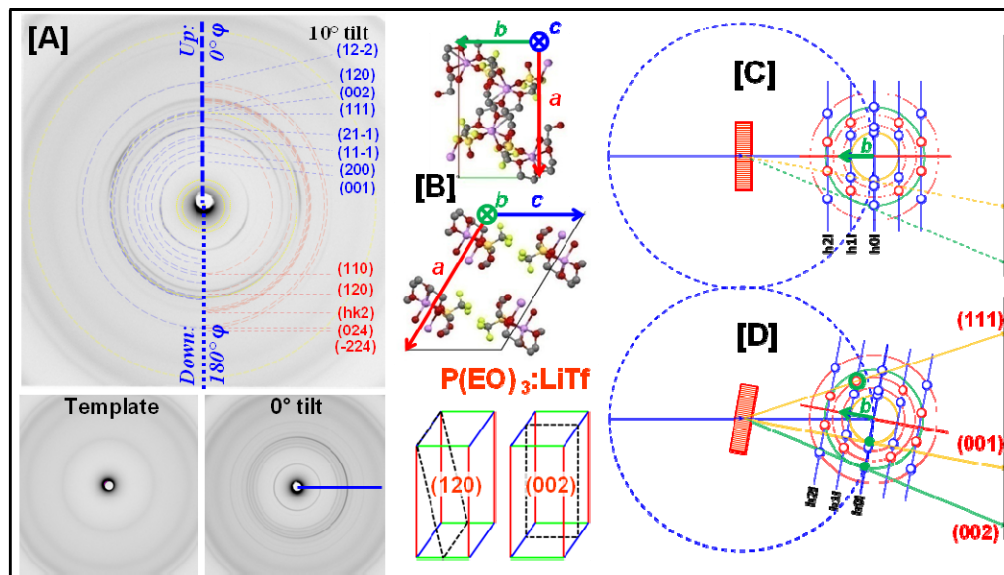


**Figure 5.4.9** (A) WAXS patterns for 10° tilted PEO:LiTf(10:1) filled 30 nm pores (top), template (bottom left), and untitled PEO:LiTf(10:1) filled 30 nm pores (bottom right). Ewald constructions of untitled [C] and 10° tilted [D] orientations.

Focusing on the peaks associated with PEO: the (120) peak (at  $19.2^\circ$ ) and the peak at  $23^\circ$  are more pronounced than in the untilted pattern with the same azimuthal orientation as observed for the PEO-filled pores as shown in figure 5.4.9. Again, this clearly indicates that the PEO component of the polymer electrolyte is ordered, as in the PEO-filled AAO case, with the polymer chain along the axis of the pore.

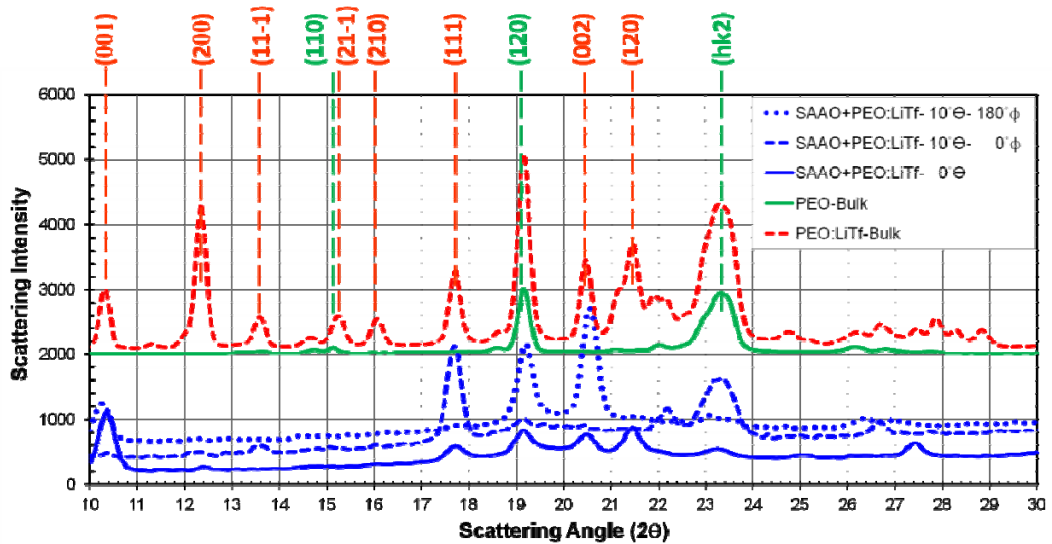


**Figure 5.4.10** Intensity versus two theta profiles for PEO:LiTf (10:1) in 30 nm pores  $10^\circ$  tilted and untilted.

Focusing on the peaks associated with  $P(\text{EO})_3\text{:LiTf}$ : the intensity of the (002) peak (at  $20.6^\circ$ ) in the  $10^\circ$ -tilt lower ( $\varphi=180^\circ$ ) line profile is nearly 20% larger than that of the bulk film and about 20x that of the upper ( $\varphi=0^\circ$ ) profile; the intensity of the (111) peak (at  $17.7^\circ$ ) in the upper ( $\varphi=0^\circ$ ) line profile is 25% larger than that of the bulk film and more than 10x that of the lower ( $\varphi=0^\circ$ ) line profile (figure 5.4.10). Ewald constructions for the  $0^\circ$  and  $10^\circ$  tilt angles (Figure (5.4.9[C & D])) illustrate the behavior of the (002) and (111) peaks. Here the

Ewald construction is for the P(EO)<sub>3</sub>:LiTf **b**-axis (polymer chain axis) directed along the pore axis. In the 0° tilt construction the (002) reciprocal lattice point is not on the Ewald sphere (no diffraction), and in the 10° tilt the (002) point is on the sphere, resulting in strong diffraction. The (111) point in the 0° tilt construction is not on the sphere, while in the 10° tilt orientation the (111) point is nearer to the sphere, resulting in increased diffraction. The behavior of these reflections indicates that the P(EO)<sub>3</sub>:LiTf polymer is ordered in the 30 nm pores, not only with the chain direction (**b**-axis) aligned with the pore, but the inter-chain separation is that of the crystal (the (002) planes are parallel to the **b**-axis). Thus in the PEO:LiTf electrolyte both the PEO and P(EO)<sub>3</sub>:LiTf phases are ordered with their respective chain directions aligned to the pore directions.

It is also interesting to investigate the differences between the AAO-confined (pores < 50 nm) and the Anodisc-confined (pores ~ 200 nm) polymer and polymer electrolyte. X-ray shows the polymer electrolyte in the Anodisc is polycrystalline at room temperature, and conductivity shows the usual melting discontinuity behavior also seen for the bulk. The untilted and 10° tilted WAXS patterns for the PEO:LiTf(10:1)-filled 200nm diameter pores Anodisc sample compared to the bulk PEO:LiTf(10:1) is shown in figure 5.4.11. The filled Anodisc film also shows the same cylindrical symmetry with relative peak heights nearly identical to the bulk polycrystalline films as shown in the inset figure [C]. This directly shows that most of the PEO:LiTf in the Anodisc (200 nm pores) are



in randomly oriented microcrystals, as in the bulk. Figure 5.4.11[C] shows the complete images used in figure 5.4.11 [A].

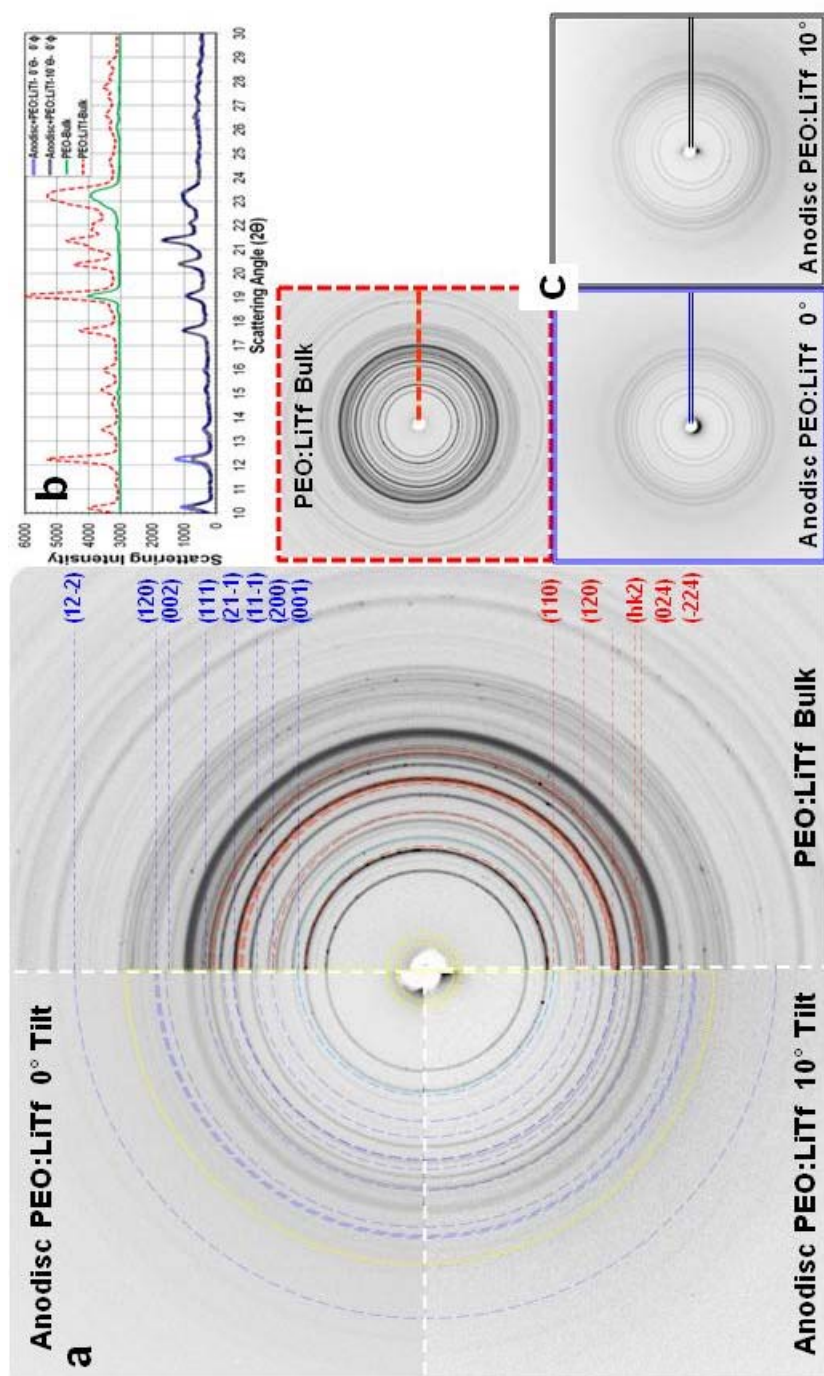


**Figure 5.4.11** WAXS patterns of bulk PEO:LiTf and Anodisc-filled PEO:LiTf. [A] WAXS patterns of Anodisc-filled and bulk PEO:LiTf, [B] Line profiles from WAXS patterns of various bulk PEO and PEO:LiTf and PEO-filled AAO and empty AAO, [C] WAXS patterns of bulk PEO:LiTf and anodisc-filled PEO:LiTf at 0° and 10° tilt, as labeled.

## 5.5 Summary and Conclusions

Below I recap the key results for each set of measurements. From the AC-Impedance measurements, the PEO:LiTf(10:1) bulk sample freezes/melts as expected at  $\sim 59$  °C as does the Anodisc-confined sample; however the AAO-confined sample does not show the usual phase change and it has a low activation energy. This latter behavior leads to conductivity that is  $100\times$  that of the bulk electrolyte. In addition, the conductance versus diameter plot indicates that this high conductivity is an area effect not a perimeter effect. The FTIR and Raman scans are consistent with the polymer-chains in the AAO-confined PEO and PEO:LiTf(10:1) samples showing some degree of alignment in the pore direction. The WAX patterns directly show that the AAO-confined PEO and PEO:LiTf(10:1) are preferentially aligned with the polymer chain aligned with the pore. while the bulk and Anodisc-confined PEO and PEO:LiTf(10:1) show no preferential alignment.

It is interesting to investigate the differences between the AAO-confined (pores  $< 50$  nm) and the Anodisc-confined (pores  $\sim 200$  nm) polymer and polymer electrolyte. X-ray shows the polymer electrolyte in the Anodisc is polycrystalline at room temperature, and conductivity shows the usual melting discontinuity behavior also seen for the bulk. X-ray shows the polymer electrolyte in the AAO is ordered with the polymer chain tending to be aligned along the pore axis for both the pure PEO and P(EO)<sub>3</sub>:LiTf phases. The conductivity does not show the usual melting behavior, and the Arrhenius plot is

linear through the temperature range where the bulk (and Anodisc confined) electrolyte melt. Recent work shows similar results for polymer confinement in pores less than about 50 nm, where confined polymers had depressed melting temperatures [123, 124]. For example, poly(vinylidene fluoride) (PVDF) shows pronounced ordering confined in 35 nm pores versus a bulk system; and poly(ethylene) shows homogeneous nucleation for  $d > 50$  nm [123] and heterogeneous nucleation (at the pore wall) for  $d < 50$  nm, [124] resulting in very different crystal morphologies for these two situations. This latter finding, involving nucleation at the pore wall for sufficiently confined structures, also is consistent with our results, where for  $d < 50$  nm the confined electrolyte interacts with the pore wall to form the ordered structures observed. This effect of the pore wall also explains why we still observe a conductivity enhancement for the Anodisc-confined polymer electrolyte (the conductivity per pore is about 10x that of the bulk conductivity and the activation energy is intermediate between the bulk solid and AAO-confined values). For an intermediate pore size, heterogeneous nucleation at the pore wall would lead to ordered polymer-electrolyte structures adjacent to the pore walls, resulting in a more conductive outer layer in the pore. For a skin that is 100x more conductive than the normal bulk conductivity of the core (values in line with our measurements), a 10 nm skin thickness would result in the 10x increase in pore conductance observed. Therefore, it is not surprising that a 10 nm ordered skin in a 200 nm pore might

escape detection using x-ray diffraction, particularly if the ordering is not sufficient to show crystalline registry.

It is important to realize that our enhanced conductivity is not simply due to a depressed melting temperature of the confined polymer electrolyte resulting in liquid-like behavior extending to room temperature. The activation energy of our confined electrolyte at low temperature is substantially lower than that of the liquid and similar to that observed for one of the latest synthesized high-conductivity crystalline polymer electrolytes (*e.g.* 44 kJ/mole for P(EO)<sub>8</sub>:NaAsF<sub>6</sub>) [22], with channels deduced from x-ray measurements (see Figure 5.4.6[B] and 5.4.9[B]). Our low activation energy persists even at temperatures well above the usual polymer electrolyte melting temperature. This indicates that not only are ordered chains aligned in the pore direction at room temperature, this ordering persists to 90°C (30 °C above the usual melting temperature and about 20 °C above the equilibrium melting temperature [121,122]). Even at such high temperatures the conductivity involves the ordered chains rather than only being facilitated by the local segmental motion in the usual liquid-like conduction. In some ways, our confined electrolyte polymer is behaving more like a liquid crystal, where there are aligned channels, which result in our observed enhanced conductivity.

In summary, since their first discovery in the 1970s, polymer electrolytes have been actively studied because they have properties important for many device applications. Even now detailed mechanisms of conductivity are still not

completely understood, so that different methods to enhance conductivity are still being explored. We demonstrated two orders of magnitude higher conductivity in the nanoscale confined structures versus bulk films. Using x-ray characterization we show that this increased conductivity is associated with ordered PEO polymer chains aligned with the template pore direction. The activation energy of the AAO-confined polymer electrolyte is found to be smaller than the unconfined melt and about half that of the unconfined solid. This result indicates that not only is the room-temperature confined polymer ordered but that this order persists at temperatures where the nano-confined polymer electrolyte is expected to be a liquid.

## Bibliography

- [1] Y. Ito, K. Kanehori, K. Miyauchi, T. Kudo, *J. mater. Sci.* 1845-1849, **22**, 1987.
- [2] H. Zhang, S. Kulkarni, and S. L. Wunder, *J. Phys. Chem. B*, 3583-3590, **111**, 2007.
- [3] D.C. Bassett, *Polymer*, 3384-3387, **48**, 2007.
- [4] J.E. Weston and B.C.H. Steele, *Solid State Ionics*, 75-79, **7**, 1982.
- [5] Y.W. Kim, W. Lee, and B. K. Choi, *Electrochimica Acta*, 1473-1477, **45**, 2000.
- [6] F. Croce, L. Persi, B. Scrosati, F. Serraino-Fiory, E. Plichta, M. A. Hendrickson. 2457-2461, **46**, 2001.
- [7] F. Capuano, F. Croce, and B. Scrosati, *J. Electrochem. Soc.* 1918-1922, **138(7)**, 1991.
- [8] F. Croce, L. Settimi, B. Scrosati, D. Zane. *J. New. Mat. Electrochem. Systems*, 3-9, **9**, 2006.
- [9] M. Marcinek, A. Bac, P. Lipka, A. Zalewska, G. Zukowska, R. Borkowska, W. Wiezorek, *J. Phys. Chem. B*, 11088-11093, **104**, 2000.
- [10] L. S. Schadler, L.C. Brinson, and W. G. Sawyer, *Nanocomposite Materials*, 50-58, 2007.
- [11] Y. Tominaga, M. Morita, S. Asai and M. Sumita, *e-Journal of Soft Materials*, 14-19, **1**, 2005.
- [12] H. -W. Chen, F. -C, Chang, *Polymer*, 9763-9769, **42**, 2001.
- [13] C. M. Burba, R. Frech, and B. Grady, *Electrochimica Acta*, 1548-1555, **53**, 2007.
- [14] D. Golodnitsky, E. Livshits, Yu. Rosenberg, I. Lapidés, E. Peled, *Solid State Ionics*, 265-273, **147**, 2002.
- [15] J.E. Weston and B.C.H. Steele, *Solid State Ionics*, 347-354, **2**, 1981.

- [16] G. B. Appetecchi, F. Croce, L. Perci, F. Ronci, B. Scrosati, *Electrochimica Acta*, 1481-1490, **45**, 2000.
- [17] D. Golodnitsky, E. Livshits, R. Kovarsky, E. Peled, S. H. Chung, S. Suarez, and S. G. Greenbaumd, *Electrochemical and Solid-State Letters*, A412-A415, **7 -11**, 2004.
- [18] P. W. Majewski, M. Gopinadhan, W. -S. Jang, J. L. Lutkenhaus, and C. O. Osuji, *J. Am. Chem. Soc.*, 17516–17522, **132**, 2010.
- [19] Y. G. Andreev, P. G. Bruce, *Electrochimica Acta*, 1417-1423, **45**, 2000.
- [20] Y. G. Andreev, P. G. Bruce, *J. Phys.:Cond. Mat.* 8245-8255, **13**, 2001.
- [21] Z. Gadjourova, Y. G. Andreev, D. P. Tunstall and P. G. Bruce, *Nature*, 520-523, **412**, 2001.
- [22] C. Zhang, S. Gamble, D. Ainsworth, A. M. Z. Slawin, Y. G. Andreev and P. G. Bruce, *Nature Materials*, 580-584, **8**, 2009.
- [23] A. M. Christie, S. J. Lilley, E. Staunton, Y. G. Andreev and P. G. Bruce, *Nature*, 50-53, **433**, 2005.
- [24] A. Liivat, D. Brandell and J. O. Thomas, *J. Mater. Chem.*, 3938-3946, **17**, 2007.
- [25] K. Shin, S. Obukhov, J. -T. Chen, J. Huh, Y. Hwang, S. Mok, P. Dobriyal, P. Thiyagarajan, T. P. Russell, *Nature Materials*, 961-965, **6**, 2007.
- [26] H. Wang, J. K. Keum, A. Hiltner, E. Baer, *Macromolecules*, 7055-7066, **42**, 2009.
- [27] K. Shin, E. Woo, Y. G. Jeong, C. Kim, J. Huh, K., -W. Kim, *Macromolecules*, 6617-6623, **40**, 2007.
- [28] H. Wu, W. Wang, H. Yang, Z. Su. *Macromolecules*, 4244-4249, **40**, 2007.
- [29] J. Martin, C. Mijangos, A. Sanz, T. A. Ezquerro, A. Nogales, *Macromolecules*, 5395-5401, **42**, 2009.
- [30] H. Wu, W. Wang, Y. Huang, C. Wang, Z. Su, *Macromolecules*, 7755-7758, **41**, 2008.

- [31] S. Nojima, Y. Ohguma, S. Namiki, T. Ishizone, *Macromolecules*, 1915-1918, **41**, 2008.
- [32] F. Vullum, D. Teeters, A. Nytén, J. Thomas, *Solid State Ionics*, 2833–2838, **177**, 2006.
- [33] M. Castriota and D. Teeters, *Ionics*, 220-225, **11**, 2005.
- [34] W. H. Meyer, *Adv. Mater.*, 439-448, **10(6)**, 1998.
- [35] D. E. Fenton, *Polymer*, 589, **14**, 1973.
- [36] P. V. Wright, *Br. Polym. J.* 319-327, **7**, 1975.
- [37] C. Berthier, W. Gorecki, M. Minier, M. B. Armand, J. M. Chamagno and P. Rigaud, *Solid State Ionics*, 91-95, **11**, 1983.
- [38] M. Armand, *Adv. Mater.* 278-286, **6(7)**, 1990.
- [39] M. A. Ratner and D. F. Shriver, *Chem. Rev.*, 109-124, **88**, 1988.
- [40] J. Y. Song, Y. Y. Wang, and C. C. Wan, *J. Power Sour.*, 183-197, **77**, 1999.
- [41] J. L. Acosta and E. Morales, *Solid State Ionics*, 85-90, **85**, 1996.
- [42] B. Scrosati, “Lithium Polymer Electrolytes”, “Advances in Lithium-Ion Batteries”, Kluwer Academic-Plenum Publishers, 2002.
- [43] J. –M. Tarascon and M. Armand, 359-367, **414**, 2001.
- [44] D. Golodnitsky, E. Livshits, A. Ulus and E. Peled, *Polym. Adv. Technol.*, 683-689, **13**, 2002.
- [45] P. G. Bruce, *Solid State Ionics*, 752-760, **179**, 2008.
- [46] R. H. Boyd and W. –B. Liao, *Macromolecules*, 2246-2249, **19**, 1986.
- [47] Y. Takahashi, I. Sumita, and H. Tadokoro, *J. Polymer Sci.*, 2113-2122, **11**, 1973.
- [48] P. Lightfoot, M. A. Mehta, and P. G. Bruce, *Science*, 883-885, **262**, 1993.



- [49] C. D. Robitaille and D. Fauteux, *J. Electrochem. Soc.*, 315-325, **133(2)**, 1986.
- [50] J. D. Edwards and F. Keller, Formation of anodic coatings on aluminum, *Trans. Electrochem. Soc.*, 135-144, **79**, 1941.
- [51] J. D. Edwards and F. Keller, The structure of anodic oxide coatings, *Trans. Am. Inst. Mining Met. Engrs*, **1710**, 1944.
- [52] F. Keller, M. S. Hunter, and D. L. Robinson, *J. Electrochemical Soc.* 411-419, **100(9)**, 1953.
- [53] J. W. Diggle, T.C. Downie, and C. W. Goulding, Anodic oxide films on aluminum, *Chem. Rev.*, 365-405, **69**, 1969.
- [54] T. P. Hoar and J. Yahalom, *J. Electrochemical Soc.*, 614-621, **110(6)**, 1963.
- [55] V. P. Parkhutik and V.I. Shershulsky, *J. Phys. D: Appl. Phys.*, 1258-1263, **25**, 1992.
- [56] J. Choi, R. B. Wehrspohn, and U. Gosele, *Electrochimica Acta*, 2591-2595, **50**, 2005.
- [57] K. Nielsch, J. Choi, K. Schwirn, R. B. Wehrspohn, and U. Gosele, *Nano Lett.*, 677-680, **2**, 2002.
- [58] N.-Q. Zhao, X. -X. Jiang, C. -S Shi, J. -J. Li, Z. -G. Zhao, X. -W. Du, *J Mater Sci.*, 3878-3882, **42**, 2007.
- [59] A. P. Li, F. Muller, A. Birner, K. Nielsch, and U. Gosele, *J. Appl. Phys.*, 6023-6026, **84(11)**, 1998.
- [60] A. P. Li, F. Muller, and U. Gosele, *Electrochem. and Solid-State Lett.*, 131-134, **3(3)**, 2000.
- [61] G. Xiong, J. W. Elam, H. Feng, C. Y. Han, H. -H Wang, L. E. Iton, L. A. Curtiss, M. J. Pellin, M. Kung, H. Kung, and P. C. Stair, *J. Phys. Chem. B*, 14059-14063, **109**, 2005.
- [62] A. L. Lipson, D. J. Comstock, and M. C. Hersam, *Small*, 2807-2811, **5(24)**, 2009.
- [63] H. Masuda, and K. Fukuda, *Science*, 1466-1468, **268(5216)**, 1995.

- [64] H. Masuda, H. Asoh, M. Watanabe, K. Nishio, M. Nakao, and T. Tamamura, *Adv. Mater.* 189-192, **13(3)**, 2001.
- [65] J. Yan, G. V. R. Rao, M. Barela, D. A. Brevnov, Y. Jiang, H. Xu, G. P. Lopez, and P. B. Atanassov. *Adv. Mater.*, 2015-2017, **15(23)**, 2003.
- [66] W. Lee, R. Ji, U. Goselle, and K. Nielsch, *Nature Materials*, 741-747, **5**, 2006.
- [67] H. Masuda and F. Hasegawa, S. Ono, *J. Electrochemical Soc.*, **144(5)**, 1997.
- [68] S. -Z. Chu, K. Wada, S. Inoue, M. Isogai, and Atsuo Yasumori, *Adv. Mater.* 2115-2119, **17**, 2005.
- [69] H. Masuda, K. Yasui, Y. Sakamoto, M. Nakao, T. Tamamura, and K. Nishio, *Jpn. J. Appl. Phys.* L1267–L1269, **40**, 2001.
- [70] N. Kouklin, L. Menon, and S. Bandyopadhyay, *Appl. Phys. Lett.*, **80(9)**, 2002.
- [71] M. Jung, S. Mhoa, H. L. Park, *Appl. Phys. Lett.*, 133121-3, **88**, 2006.
- [72] P. Banerjee, I. Perez, L. H. -Lecordier, S. B. Lee, and G. W. Rubloff, *Letters-Nature Nanotechnology*, 292-296, **4**, 2009.
- [73] M. Vázquez, M. Hernández-Vélez, K. Pirola, A. Asenjo, D. Navas, J. Velázquez, P. Vargas, and C. Ramos, *Eur. Phys. J. B.* 489–497, **40**, 2004.
- [74] A. Holtzel, U. Tallarek, *J. Sep. Sci.*, 1398-1419, **30**, 2007.
- [75] R. Gasparac, P. Kohli, M. O. Mota, L. Trofin, and C. R. Martin, *Nano Lett.*, 513-516, **4(3)**, 2004.
- [76] C. R. Martin, *Chem. Mater.*, 1739-1746, **8**, 1996.
- [77] H. Masuda and M. Satoh, *Jpn. J. Appl. Phys.* L126-L129, **35**, 1996.
- [78] L. Vila, P. Vincent, L. D. -De Pra, G. Pirio, E. Minoux, L. Gangloff, S. D. -Champagne, N. Sarazin, E. Ferain, R. Legras, L. Piraux, and P. Legagneux. *Nano Lett.*, 521-524, **4(3)**, 2004.

- [79] T. Ohgai, X. Hoffer, A. Fabian, L. Gravier and J. -P Ansermet, *J. Mater. Chem*, 2530–2534, **13**, 2003.
- [80] M. D. Dickey, E. A. Weiss, E. J. Smythe, R. C. Chiechi, F. Capasso, and G.M. Whitesides, *American Chemical Society*, 800-508, **2(4)**, 2008.
- [81] G. Duan, W. Cai, Y. Li, B. Cao, Z. Li, Y. Luo, *J Phys Chem B.*, 15729-33, **110(32)**, 2006.
- [82] H. H. Wang, C. Y. Han, G. A. Willing, and Z. Xiao, *Mat. Res. Soc. Symp. Proc.* 107-112, **775**, 2003.
- [83] Y. Kanamori, K. Hane, H. Sai, and H. Yugami, *Appl. Phys. Lett.*, 142-143, **78(2)**, 2001.
- [84] M. Nakao, S. Oku, T. Tamamura, K. Yasui, and H. Masuda, *Jpn. J. Appl. Phys.* 1052-1055, **38**, 1999.
- [85] A. Kolmakov, Y. Zhang, G. Cheng, and M. Moskovits, *Adv. Mater.* 997-1000, **15(12)**, 2003.
- [86] S. Liu, Q. Pu, L. Gao, C. Korzeniewski, and C. Matzke. *Nano Letters*, 1389-1393, **5(7)**, 2005.
- [87] L. Liu, X. Chen, W. Lu, A. Han, and Y. Qiao, *Phys. Rev. Lett.*, 184501-1-4, **102**, 2009.
- [88] H. Mukaibo and T. Momma, T. Osaka et al. (eds.), *Chapter-2, Electrochemical Nanotechnologies*, 2010.
- [89] H. Matsuura and K. Fukuhara, *J. Poly. Sci: Part B: Polymer Physics*, 1383-1400, **24**, 1986.
- [90] H. Matsuura and T. Miyazawa, *J. Poly. Sci: Part A-2*, 1735-1744, **7**, 1969.
- [91] H. Matsuura, M. Hiraishi, and T. Miyazawa, *Spectrochimica Acta*, 2299-2304, **28A**, 1972.
- [92] K. Machida and T. Miyazawa, *Spectrochimica Acta*, 1865-1873, **20**, 1964.
- [93] H. Matsuura, T. Miyazawa, and K. Machida, *Spectrochimica Acta*, 771-779, **29A**, 1973.

- [94] M.A.K.L. Dissanayake and Roger Frech, *Macromolecules*, 5312-5319, **28**, 1995.
- [95] D. R. Macfarlane, P. Meakin, A. Bishop, D. McNaughton, J. M Rosalie, M. Forsyth, *Electrochimca Acta*, 2333-2337, **40(13)**, 1995.
- [96] J. Maxfield and I. W. Shepherd, *Polymer*, 505-509, **16**, 1975.
- [97] R. Frech, S. Chintapalli, P. G. Bruce, C. A. Vincent, *Macromolecules*, 808-813, **32**, 1999.
- [98] R. Frech and W. Huang, *Macromolecules*, 1246-1251, **28**, 1995.
- [99] A. Brodin and P. Jacobsson, *Ukr. J. Phys.* 259-265, **54(3)**, 2009.
- [100] H. Tadokoro, T. Yasumoto, S. Murahashi, I. Nitta, *J. Polymer Sci.* 266-269, **44**, 1960.
- [101] H. Tadokoro, Y. Chatani, T. Yoshihara, S. Tahara, S. Murahashi, *Macromol. Chem.*, 109-127, **73**, 1964.
- [102] Y. Takahashi and H. Tadokoro, *Macromolecules*, 672-675, **6(5)**, 1973.
- [103] E. Bortel, s. Hodorowicz, and R. Lamot, *Macromol.Chem.* 2491-2498, **180**, 1979.
- [104] J. C. Machado, G. G. Silva, F. C. De Oliveira, R. L. Lavall, J. Rieumont, P. Licinio, D. Windmoller. *J Poly. Sci.:Part B: Polymer Physics*,2400-2409, 2007.
- [105] L.E. Alexander, "X-ray diffraction methods in polymer science", John Wiley and Sons Inc., 1969.
- [106] L. Zhu, S. Z. D. Cheng, B. H. Calhoun, Q. Ge, R. P. Quirk, E. L. Thomas, B. S. Hsiao, F. Yeh, and B. Lotz, *J. Am. Chem. Soc.* 5957-5967, **122**, 2000,
- [107] M. S. Whittingham, *Electrochimca Acta*, 575-583, **20**, 1975.
- [108] C. W. Hass, *J. Solid State Chem.*,155-157, **7**, 1973.
- [109] T. Caruso, S. Capoleoni, E. Cazzanelli, R. G. Agostino, P. Villano, s. Passerini, *Ionics*, 36-43, **8**, 2002.

- [110] J. Evans, C. A. Vincent, P. G. Bruce, *Polymer*, 2324-2328, **28**, 1987.
- [111] F. Bellucci, M. Valentino, T. Monetta, L. Nicodemo, J. Kenny, L. Nicolais, J. Mijovic, *J. Poly. Sci.: Part B: Poly. Phys.*, 2519-2527, **32**, 1994.
- [112] J. R. Mac Callum and C. A. Vincent, "Polymer Electrolyte Reviews-1", Elsevier Science Publishers Ltd, 1987.
- [113] J. Goldstein, D. Newbury, D. Joy, C. Lyman, P. Echlin, E. Lifshin, L. Sawyer, and J. Michael, "Scanning Electron Microscopy and X-Ray Microanalysis", Third Edition, Springer, 2003.
- [114] E. Barsoukov, J. R. Macdonald, "Impedance spectroscopy", A John Wiley & Sons, Inc., Publication, 1987.
- [115] N. I. Kovtyukhova, T. E. Mallouk, *Adv. Mater.*, 780-785, **15(10)**, 2003.
- [116] F. Buyukserina, C. R. Martin, *Applied Surface Science*, 7700-7705, **256**, 2010.
- [117] Y. Ma and G. Reiter, *Macromolecules*, 5159-5164, **39**, 2006.
- [118] T. Miyazawa, K. Fukushima, and Y. Ideguchi, *J. Chem. Phys.*, 2764-2776, **37**, 1962.
- [119] T. Yoshihara, H. Tadokoro, and S. Murahashi, *J. Chem. Phys.*, 2902-2911, **41**, 1964.
- [120] M. Tremayne, P. Lightfoot, M. A. Mehta, and P. G. Bruce, K. D. M. Harris, K. Shankland, C. J. Gilmore, G. Bricogne, *J. Solid State Chem*, 191-196, **100**, 1992.
- [121] C. P. Buckley and A. J. Kovacs, *Colloid and Polymer Science*, 695-715, **254**, 1976.
- [122] L. Mandelkern and G. M. Stack, *Macromolecules*, 871-878, **17**, 1984.
- [123] M. Steinhart, P. Goring, H. Dernaika, M. Prabhakaran, U. Gosele, *Physical Review Letters*, 027801-(1)-027801-(4), **97**, 2006.
- [124] L. J. Dunne and George Manos, "Adsorption and Phase Behavior in Nanochannels and Nanotubes", P(257-272), 2009.

## Appendix 1: Complementary tables and figures for FTIR and FT-Raman spectra

**Table A1.1.** Molecular vibrational frequencies of Poly(ethylene oxide), (PEO), for mid Infra-Red(IR) region, A and C depicts for amorphous and crystalline phases, and; br-broad, s-small, m-medium, sh-shoulder, vs-very small, w-weak.

Poly(ethylene oxide)-Vibration mode	Symbol	IR (cm <sup>-1</sup> )	Strength	Phase (Cryst./Amorph.)	Refs
OH stretch	$\nu(\text{OH})$	3440-80	br	A, C	[91]
CH <sub>3</sub> asymmetric stretch	$\nu_{\text{as}}(\text{CH}_3)$	2973	s	A, C	[90-92]
CH <sub>2</sub> asymmetric stretch	$\nu_{\text{as}}(\text{CH}_2)$	2950	m	C	[91]
CH <sub>2</sub> asymmetric stretch	$\nu_{\text{as}}(\text{CH}_2)$	2930	sh	A	[90, 92]
CH <sub>2</sub> asymmetric stretch	$\nu_{\text{as}}(\text{CH}_2)$	2939	sh	C	[93]
CH <sub>2</sub> symmetric stretch	$\nu_{\text{s}}(\text{CH}_2)$	2922	sh, s	A, C	[90, 93]
CH <sub>2</sub> symmetric stretch	$\nu_{\text{s}}(\text{CH}_2)$	2890	vs	C	[93]
CH <sub>2</sub> symmetric stretch	$\nu_{\text{s}}(\text{CH}_2)$	2885	vs	A, C	[90, 93]
CH <sub>2</sub> symmetric stretch	$\nu_{\text{s}}(\text{CH}_2)$	2880	s	A, C	[90, 93]
CH <sub>2</sub> symmetric stretch	$\nu_{\text{s}}(\text{CH}_2)$	2865	s	A, C	[90,92-93]
CH <sub>2</sub> symmetric stretch	$\nu_{\text{s}}(\text{CH}_2)$	2800	sh	C	[93]
bending overtones		2740	w	A C	[91, 93]
bending overtones		2730	sh	A	[91]
bending overtones		2695	w	C	[91,93]
CH <sub>2</sub> scissor		1485	sh	A	[90,91]
CH <sub>2</sub> scissor		1470	m	C	[90,91,93]
CH <sub>2</sub> scissor		1463	m	A, C	[90-93]
CH <sub>3</sub> asymmetric deformation	$\delta_{\text{as}}(\text{CH}_3)$	1457	m	A, C	[90,91,93]
CH <sub>3</sub> deformation	$\delta_{\text{s}}(\text{CH}_3)$	1453	m, w	A, C	[90,91,93]
CH <sub>2</sub> wagging	$\omega(\text{CH}_2)$	1412-18	w	C	[90,91,93]
CH <sub>2</sub> wagging	$\omega(\text{CH}_2)$	1385	w	C	[90,91,93]
CH <sub>2</sub> wagging	$\omega(\text{CH}_2)$	1374	vw	C	[90,91,93]
CH <sub>2</sub> wagging	$\omega(\text{CH}_2)$	1361	m	C	[90,91,93]
CH <sub>2</sub> wagging	$\omega(\text{CH}_2)$	1352	m	A	[90, 92]
CH <sub>2</sub> asymmetric wagging	$\omega_{\text{as}}(\text{CH}_2)$	1345	s	C	[90,91,93]
symmetric and asymmetric CH <sub>2</sub> twisting	$\tau_{\text{s}}(\text{CH}_2) + \tau_{\text{as}}(\text{CH}_2)$	1325	w	A	[90, 92]
symmetric and asymmetric CH <sub>2</sub> twisting	$\tau_{\text{s}}(\text{CH}_2) + \tau_{\text{as}}(\text{CH}_2)$	1300	w	A	[90, 92]
CH <sub>2</sub> twisting	$\tau_{\text{s}}(\text{CH}_2)$	1296	m	A	[90,91]
symmetric and asymmetric CH <sub>2</sub> twisting	$\tau_{\text{s}}(\text{CH}_2) + \tau_{\text{as}}(\text{CH}_2)$	1283	w, m	A, C	[90,91,93]
CH <sub>2</sub> twisting	$\tau_{\text{s}}(\text{CH}_2)$	1252	m	A	[90, 92]
symmetric and asymmetric CH <sub>2</sub> twisting	$\tau_{\text{s}}(\text{CH}_2) - \tau_{\text{as}}(\text{CH}_2)$	1235		C	[90,91,93]
CH <sub>3</sub> rocking	$\rho(\text{CH}_3)$	1198	w	C	[93]
CH <sub>3</sub> rocking	$\rho(\text{CH}_3)$	1160	sh	C	[93]
combination of CC and CO stretch	$\nu_{\text{s}}(\text{CC}) - \nu_{\text{as}}(\text{COC})$	1149	m, s	A, C	[93]
CO stretch and CH <sub>2</sub> rocking	$\nu(\text{C-O}) + \rho(\text{CH}_2)$	1144	m	C	[89,93]
CO stretch and CH <sub>2</sub> rocking	$\nu(\text{C-O}) + \rho(\text{CH}_2)$	1140	sh	A	[90, 92]
CO stretch and CH <sub>2</sub> rocking	$\nu(\text{C-O}) + \rho(\text{CH}_2)$	1113	vw	C	[89,93]
CO stretch and CH <sub>2</sub> rocking	$\nu(\text{C-O}) + \rho(\text{CH}_2)$	1110	vw	A	[90, 92]
COC ass-stretch and CH <sub>2</sub> symmetric rocking	$\nu_{\text{as}}(\text{COC}) + \rho_{\text{s}}(\text{CH}_2)$	1062	m	C	[89,90,93]
O-CH <sub>3</sub> stretch	$\nu(\text{O-CH}_3)$	1030	m	C	[93]
CC stretch and CH <sub>2</sub> rocking	$\nu(\text{C-C}) + \rho(\text{CH}_2)$	992	w	A	[90, 92]
CC stretch and CH <sub>2</sub> rocking	$\nu(\text{C-C}) + \rho(\text{CH}_2)$	961	sh	C	[90,93]
CC stretch and CH <sub>2</sub> rocking	$\nu(\text{C-C}) + \rho(\text{CH}_2)$	954	sh	C	[93]
C-C stretch and CH <sub>2</sub> rocking	$\nu(\text{C-C}) + \rho(\text{CH}_2)$	948	m	A, C	[91-93]
CC stretch and CH <sub>2</sub> rocking	$\nu(\text{C-C}) + \rho(\text{CH}_2)$	938	m	C	[93]
C-C stretch and CH <sub>2</sub> rocking	$\nu(\text{C-C}) + \rho(\text{CH}_2)$	934	w	C	[89,93]
CH <sub>2</sub> rocking, COC stretching	$\rho(\text{CH}_2), \nu(\text{COC})$	857	m	C	[93]
COC stretching, CH <sub>2</sub> rocking	$\nu(\text{C-O}), \rho(\text{CH}_2)$	856	m	A, C	[93]
CH <sub>2</sub> rocking, COC stretching	$\rho(\text{CH}_2), \nu(\text{COC})$	844	s	C	[89,93]
CH <sub>2</sub> rocking, COC stretching	$\rho(\text{CH}_2), \nu(\text{COC})$	828		C	[89,93]

**Table A1.2.** Molecular vibrational frequencies of Poly(ethylene oxide), (PEO), for FT-Raman (mid IR- region). A and C depicts for amorphous and crystalline phases, and; br- broad, s-small, m-medium, sh-shoulder, vs-very small, w-weak.

Poly(ethylene oxide)-Vibration mode	Symbol	Raman (cm <sup>-1</sup> )	Strength	Phase (Cryst./Amorph.)	Refs
OH stretch	$\nu(\text{OH})$	3340	w, br,	A, C	[90, 92]
CH <sub>2</sub> asymmetric stretch	$\nu_{\text{as}}(\text{CH}_2)$	2978	sh	A, C	[90, 92]
CH <sub>2</sub> asymmetric stretch	$\nu_{\text{as}}(\text{CH}_2)$	2941	sr	A, C	[90, 92]
CH <sub>2</sub> asymmetric stretch	$\nu_{\text{as}}(\text{CH}_2)$	2937	s	A, C	[90, 92]
CH <sub>2</sub> symmetric stretch	$\nu_{\text{s}}(\text{CH}_2)$	2883	s	A, C	[90, 92]
CH <sub>2</sub> symmetric stretch	$\nu_{\text{s}}(\text{CH}_2)$	2876	s	A, C	[90, 92]
CH <sub>2</sub> symmetric stretch	$\nu_{\text{s}}(\text{CH}_2)$	2825	m	A, C	[90, 92]
CH <sub>2</sub> scissor	$\delta_{\text{s}}(\text{CH}_2)$	1487	s	C	[96]
CH <sub>2</sub> scissor	$\delta_{\text{as}}(\text{CH}_2)$	1473	s, sh	A, C	[89,96]
CH <sub>2</sub> scissor	$\delta_{\text{s}}(\text{CH}_2)$	1452	m	A	[96]
CH <sub>2</sub> scissor	$\delta_{\text{s}}(\text{CH}_2)$	1448	m	C	[96]
CH <sub>2</sub> wagging and C-C stretch	$\omega_{\text{s}}(\text{CH}_2)+\nu(\text{C-C})$	1398	w	A, C	[89,96]
CH <sub>2</sub> wagging and C-C stretch	$\omega_{\text{s}}(\text{CH}_2)+\nu(\text{C-C})$	1372	vw	A	[96]
CH <sub>2</sub> wagging and C-C stretch	$\omega_{\text{s}}(\text{CH}_2)+\nu(\text{C-C})$	1364	w	C	[96]
symmetric and asymmetric CH <sub>2</sub> twisting	$\tau_{\text{s}}(\text{CH}_2)+\tau_{\text{as}}(\text{CH}_2)$	1298	s	A	[96]
symmetric and asymmetric CH <sub>2</sub> twisting	$\tau_{\text{s}}(\text{CH}_2)+\tau_{\text{as}}(\text{CH}_2)$	1285	s	A	[96]
symmetric and asymmetric CH <sub>2</sub> twisting	$\tau_{\text{s}}(\text{CH}_2)+\tau_{\text{as}}(\text{CH}_2)$	1283	vs	C	[96]
CH <sub>2</sub> twisting	$\tau_{\text{s}}(\text{CH}_2)$	1248	m	A	[96]
CH <sub>2</sub> twisting	$\tau_{\text{s}}(\text{CH}_2)$	1239	w	C	[96]
CH <sub>2</sub> asymmetric twisting	$\tau_{\text{as}}(\text{CH}_2)$	1234	m	C	[96]
CH <sub>2</sub> asymmetric twisting	$\tau_{\text{as}}(\text{CH}_2)$	1230	vw	A	[96]
COC asymmetric stretch	$\nu_{\text{s}}(\text{COC})$	1143	m	C	[96]
COC asymmetric stretch	$\nu_{\text{s}}(\text{COC})$	1139	s	A	[96]
COC stretch	$\nu_{\text{s}}(\text{COC})$	1127	m	C	[96]
COC stretch	$\nu_{\text{s}}(\text{COC})$	1123	sh	A	[96]
COC stretch	$\nu_{\text{s}}(\text{COC})$	1116	vw	A	[96]
COC stretch	$\nu_{\text{s}}(\text{COC})$	1112	vm	C	[96]
CO stretch and CH <sub>2</sub> rocking	$\nu_{\text{s}}(\text{CC})-\nu_{\text{s}}(\text{COC})$	1075	sh	C	[96]
COC stretch and CH <sub>2</sub> asymmetric rocking	$\nu_{\text{s}}(\text{COC})+\rho_{\text{as}}(\text{CH}_2)$	1065	m	C	[96]
COC stretch and CH <sub>2</sub> asymmetric rocking	$\nu_{\text{s}}(\text{COC})+\rho_{\text{as}}(\text{CH}_2)$	1061	vw	A	[96]
COC ass-stretch and CH <sub>2</sub> symmetric rocking	$\nu_{\text{as}}(\text{COC})+\rho_{\text{s}}(\text{CH}_2)$	1041	m	A	[96]
COC ass-stretch and CH <sub>2</sub> symmetric rocking	$\nu_{\text{as}}(\text{COC})+\rho_{\text{s}}(\text{CH}_2)$	948	w	C	[96]
COC ass-stretch and CH <sub>2</sub> symmetric rocking	$\nu_{\text{as}}(\text{COC})+\rho_{\text{s}}(\text{CH}_2)$	943	w	A	[96]
	$\nu(\text{O-CH}_3)$	936	w	C	[96]
CH <sub>2</sub> asymmetric rocking		884	w	A	[96]
CH <sub>2</sub> rocking, COC stretch		862	m	C	[96]
CC stretch and (CH <sub>2</sub> ) rocking	$\nu(\text{C-C})+\rho(\text{CH}_2)$	851	s	A	[96]
CH <sub>2</sub> rocking	$\rho(\text{CH}_2)$	846	vs	C	[96]
CH <sub>2</sub> rocking	$\rho(\text{CH}_2)$	834	sh	C	[96]
CH <sub>2</sub> rocking	$\rho(\text{CH}_2)$	832	sh	A	[96]
CH <sub>2</sub> rocking	$\rho(\text{CH}_2)$	810	w	C	[96]

**Table A1.3.** Molecular vibrational frequencies of PEO:LiTf polymer electrolytes in mid Infra-red(IR) region. A and C depicts for amorphous and crystalline phases, and; br-broad, s-small, m-medium, sh-shoulder, vs-very small, w-weak.

PEO:LiTf-Vibration mode	Symbol	IR (cm <sup>-1</sup> )	Strength	Phase (Cryst./Amorph.)	Refs
OH stretch	$\nu(\text{OH})$	3440-80	br	A, C	[90-92]
CH <sub>3</sub> asymmetric stretch	$\nu_{\text{as}}(\text{CH}_3)$	2973	s	A, C	[91]
CH <sub>2</sub> asymmetric stretch	$\nu_{\text{as}}(\text{CH}_2)$	2950	m	C	[90, 92]
CH <sub>2</sub> asymmetric stretch	$\nu_{\text{as}}(\text{CH}_2)$	2930	s	A	[93]
CH <sub>2</sub> asymmetric stretch	$\nu_{\text{as}}(\text{CH}_2)$	2939	sh	C	[90, 93]
CH <sub>2</sub> symmetric stretch	$\nu_{\text{s}}(\text{CH}_2)$	2922	sh, s	A, C	[93]
CH <sub>2</sub> symmetric stretch	$\nu_{\text{s}}(\text{CH}_2)$	2890	vs	C	[90, 93]
CH <sub>2</sub> symmetric stretch	$\nu_{\text{s}}(\text{CH}_2)$	2885	vs	A, C	[90, 93]
CH <sub>2</sub> symmetric stretch	$\nu_{\text{s}}(\text{CH}_2)$	2880	s	A, C	[90,92-93]
CH <sub>2</sub> symmetric stretch	$\nu_{\text{s}}(\text{CH}_2)$	2865	s	A, C	[93]
CH <sub>2</sub> symmetric stretch	$\nu_{\text{s}}(\text{CH}_2)$	2800	sh	C	[91, 93]
overtones		2740	w	A C	[91]
overtones		2730	w	A	[91,93]
overtones		2695	w	C	[91, 93]
CH <sub>2</sub> scissor		1470	m	C	[90,91,93]
CH <sub>2</sub> scissor		1463	m	A, C	[90-93]
CH <sub>3</sub> asymmetric deformation	$\delta_{\text{as}}(\text{CH}_3)$	1457	m	A, C	[90,91,93]
CH <sub>3</sub> deformation	$\delta_{\text{s}}(\text{CH}_3)$	1453	m, w	A, C	[90,91,93]
CH <sub>2</sub> wagging	$\omega(\text{CH}_2)$	1412-18	w	C	[90,91,93]
CH <sub>2</sub> symm wagging and CC symm stretch	$\omega(\text{CH}_2)+\nu(\text{C-C})$	1367	s	C	[94]
CH <sub>2</sub> wagging	$\omega(\text{CH}_2)$	1361	m	C	[90,91,93,94]
CH <sub>2</sub> wagging	$\omega(\text{CH}_2)$	1385	w	C	[90,91,93]
CH <sub>2</sub> wagging	$\omega(\text{CH}_2)$	1374	vw	C	[90,91,93]
CH <sub>2</sub> wagging	$\omega(\text{CH}_2)$	1352	m	A	[90, 92]
CH <sub>2</sub> antiwagging	$\omega_{\text{as}}(\text{CH}_2)$	1345	m	C	[90,91,93,94]
CH <sub>2</sub> antiwagging	$\omega_{\text{as}}(\text{CH}_2)$	1340	m	C	[90,91,93,94]
assymmetric and symmetric CH <sub>2</sub> twisting	$\tau_{\text{s}}(\text{CH}_2)+\tau_{\text{as}}(\text{CH}_2)$	1325	w	A	[90, 92]
SO <sub>3</sub> asymmetric stretch	$\nu_{\text{as}}(\text{SO}_3)$	1308			[94,95]
assymmetric and symmetric CH <sub>2</sub> twisting	$\tau_{\text{s}}(\text{CH}_2)+\tau_{\text{as}}(\text{CH}_2)$	1300	w	A	[90, 92]
SO <sub>3</sub> asymmetric stretch	$\nu_{\text{as}}(\text{SO}_3)$	1288	sh	C	[94,95]
assymmetric and symmetric CH <sub>2</sub> twisting	$\tau_{\text{s}}(\text{CH}_2)+\tau_{\text{as}}(\text{CH}_2)$	1283	s	A, C	[90,91,93,94]
SO <sub>3</sub> asymmetric stretch	$\nu_{\text{as}}(\text{SO}_3)$	1270			[90, 92]
SO <sub>3</sub> asymmetric stretch	$\nu_{\text{as}}(\text{SO}_3)$	1272			[90, 92]
SO <sub>3</sub> asymmetric stretch	$\nu_{\text{as}}(\text{SO}_3)$	1262		C	[90, 92]
SO <sub>3</sub> asymmetric stretch	$\nu_{\text{as}}(\text{SO}_3)$	1265		A	[90, 92]



**Table A1.4.** Molecular vibrational frequencies of PEO:LiTf polymer electrolytes for FT-Raman ( in mid IR region). A and C depicts for amorphous and crystalline phases, and; br-broad, s-small, m-medium, sh-shoulder, vs-very small, w-weak.

PEO:LiTf-Vibration mode	Symbol	IR (cm <sup>-1</sup> )	Strength	Phase (Cryst./Amorph.)	Refs
SO <sub>3</sub> asymmetric stretch	$\nu_{as}(\text{SO}_3)$	1257		A	[90, 92]
CH <sub>2</sub> twisting	$\tau_s(\text{CH}_2)$	1252	m	A	[90, 92]
CH <sub>2</sub> asymmetric twisting	$\tau_{as}(\text{CH}_2)$	1244	sh	C	[90,91,93,94]
CF <sub>3</sub> symmetric stretching	$\nu_s(\text{CF}_3)$	1233	s	A, C	[97,98]
assymmetric and symmetric CH <sub>2</sub> twisting	$\tau_s(\text{CH}_2)-\tau_{as}(\text{CH}_2)$	1235	s	C	[90,91,93,94]
CH <sub>3</sub> rocking	$\rho(\text{CH}_3)$	1198	w	C	[93]
CF <sub>3</sub> symm stretching	$\nu_s(\text{CF}_3)$	1179	sh	C	[94]
combination of CO and CC symmetric stretch	$\nu_s(\text{CC})-\nu_{as}(\text{COC})$	1149	m, s	A, C	[93]
CO stretch and CH <sub>2</sub> rocking	$\nu(\text{C-O})+\rho(\text{CH}_2)$	1144	m	C	[89,93]
CO stretch and CH <sub>2</sub> rocking	$\nu(\text{C-O})+\rho(\text{CH}_2)$	1140	sh	A	1,3
CO stretch and CH <sub>2</sub> rocking	$\nu(\text{C-O})+\rho(\text{CH}_2)$	1113	vw	C	[89,93,94]
CO stretch and CH <sub>2</sub> rocking	$\nu(\text{C-O})+\rho(\text{CH}_2)$	1110	vw	A, C	[90, 92,94]
COC stretch and CH <sub>2</sub> symmetric rocking	$\nu_{as}(\text{COC})+\rho_s(\text{CH}_2)$	1062	m	C	[89,90,93,94]
SO <sub>3</sub> asymm stretch	$\nu_{as}(\text{SO}_3)$	1062	sh	A, C	[94,95]
O-CH <sub>3</sub> stretch	$\nu(\text{O-CH}_3)$	1030	m	C	[93]
SO <sub>3</sub> symm stretch	$\nu_s(\text{SO}_3)$	1033	w		[94,95]
SO <sub>3</sub> symm stretch	$\nu_s(\text{SO}_3)$	1045	s	C	[94,95]
SO <sub>3</sub> symm stretch	$\nu_s(\text{SO}_3)$	1043			[94,95]
SO <sub>3</sub> symm stretch	$\nu_s(\text{SO}_3)$	1040			[94,95]
CC stretch and CH <sub>2</sub> rocking	$\nu(\text{C-C})+\rho(\text{CH}_2)$	992	w	A	[90, 92]
CH <sub>2</sub> assymmetric rocking	$\rho_{as}(\text{CH}_2)$	969			[94]
CH <sub>2</sub> rocking, CC stretching		961	sh	C	[90,93,94]
CH <sub>2</sub> rocking, CC stretching		954	sh	C	[93,94]
CC stretch and CH <sub>2</sub> rocking	$\nu(\text{C-C})+\rho(\text{CH}_2)$	948	m	A, C	[90, 92,93]
CH <sub>2</sub> rocking, CC stretching		938	m	C	[93]
CH <sub>2</sub> rocking, CC stretching		934	w	C	[89,93]
CH <sub>2</sub> rocking, COC stretching	$\rho(\text{CH}_2), \nu(\text{COC})$	857	s	C	[93,94]
CH <sub>2</sub> rocking, COC stretching	$\nu(\text{C-O}), \rho(\text{CH}_2)$	856	m	A, C	[93]
CH <sub>2</sub> rocking, COC stretching	$\rho(\text{CH}_2), \nu(\text{COC})$	844	s	C	[89,93,94]
primary CH <sub>2</sub> ass-rock for O-C-C-O torsion		834			
CH <sub>2</sub> rocking, COC stretching	$\rho(\text{CH}_2), \nu(\text{COC})$	828		C	[89,93,94]
CF <sub>3</sub> symmetric deformation	$\delta_s(\text{CF}_3)$	761	s	A, C	[94]
CF <sub>3</sub> symmetric deformation	$\delta_s(\text{CF}_3)$	757	w	A, C	[94]
CF <sub>3</sub> symmetric deformation	$\delta_s(\text{CF}_3)$	753	w	A, C	[94]

**Table A1.5** Character table for PEO under the factor group  $D(4\pi/7)$ .

$D(4\pi/7)$	E	$2C^1$	$2C^2$	$2C^3$	$7C_2$	$N^b$	Infrared	Raman
$A_1$	1	1	1	1	1	10	F	A
$A_2$	1	1	1	1	-1	$1-2(T_{  }, R_{  })$	$A(  )$	F
$E_1$	2	$2\cos(\omega)$	$2\cos(2\omega)$	$2\cos(3\omega)$	0	$21-1(T_{\perp})$	$A(\perp)$	A
$E_2$	2	$2\cos(2\omega)$	$2\cos(4\omega)$	$2\cos(6\omega)$	0	21	F	A
$E_3$	2	$2\cos(3\omega)$	$2\cos(6\omega)$	$2\cos(9\omega)$	0	21	F	F

**Table A1.6.** Character table for PEO:LiTf under the factor group  $C(2\pi/2)$ .

$C(2\pi/2)$	E	$C2(z)$	$\sigma_v(xz)$	$\sigma_v(yz)$	linear, rotations	quadratic
$A_1$	1	1	1	1	z	$x^2, y^2, z^2$
$A_2$	1	1	-1	-1	Rz	xy
$B_1$	1	-1	1	-1	x, Ry	xz
$B_2$	1	-1	-1	1	y, Rx	yz

### A1.1 FTIR spectra of empty nanopores

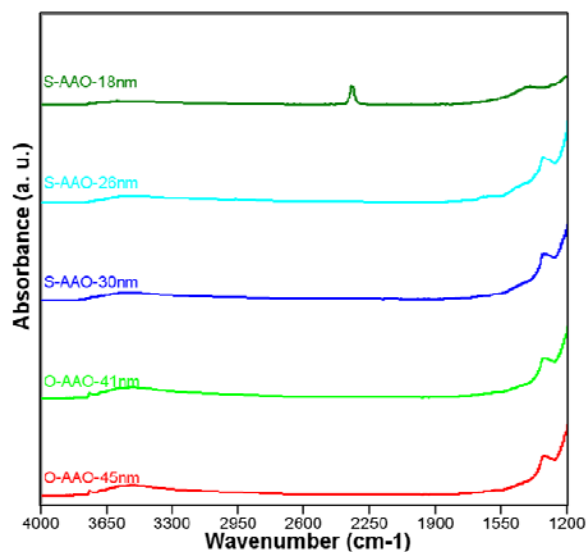


**Figure A1.1** FTIR spectra (4000-1200 cm<sup>-1</sup>) of AAO templates: All templates annealed at 1000 °C for 15h in high purity N<sub>2</sub>; 45 nm pores O-AAO, 30nm pores S-AAO, and 41, 26, and 18 nm pores were obtained by SiO<sub>2</sub> coating on annealed 45 and 30 nm pores respectively.

### A1.2 Raman spectra of empty nanopores

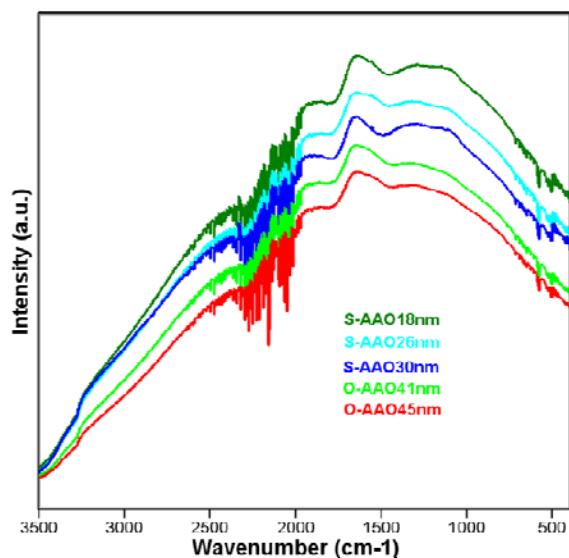


**Figure A1.2** Raman spectra (3500-400 cm<sup>-1</sup>) of AAO templates: All templates annealed at 1000 °C for 15h in high purity N<sub>2</sub>, 45 nm pores O-AAO, and 30nm pores S-AAO. 41, 26, and 18 nm pores were obtained by SiO<sub>2</sub> coating on annealed 45 and 30 nm pores respectively.

## Appendix 2: Supplementary information for WAXS

### A2.1 Equations for lattice interplanar spacing ( $d_{hkl}$ ) calculation

Symbols in equations depict for,

$h, k, l$  - for miller indices

$a, b, c$  - unit cell dimensions in Å units

$\alpha, \beta, \gamma$  - interaxial angles

- I. Cubic lattice ( $a = b = c, \alpha = \beta = \gamma = 90^\circ$ )

$$d = \frac{a}{\sqrt{h^2 + k^2 + l^2}}$$

- II. Tetragonal lattice ( $a = b \neq c, \alpha = \beta = \gamma = 90^\circ$ )

$$d = \left[ \frac{h^2}{a^2} + \frac{k^2}{a^2} + \frac{l^2}{c^2} \right]^{-\frac{1}{2}}$$



Orthorhombic lattice ( $a \neq b \neq c, \alpha = \beta$

$= \gamma = 90^\circ$ )

$$d = \left[ \frac{h^2}{a^2} + \frac{k^2}{b^2} + \frac{l^2}{c^2} \right]^{-\frac{1}{2}}$$



III. Hexagonal lattice ( $a = b \neq c$ ,  $\alpha = \beta = 90^\circ$ ,  $\gamma = 120^\circ$ ) with hexagonal indexing

$$d = a \left[ \frac{4}{3a^2}(h^2 + k^2 + hk) + \frac{l^2}{c^2} \right]^{-\frac{1}{2}}$$



IV. Hexagonal lattice ( $a = b = c$ ,  $\alpha = \beta = \gamma \neq 90^\circ$ ) with rhombohedral indexing

$$d = a \left[ \frac{(h^2 + k^2 + l^2) \sin^2 \alpha + 2(hk + hl + kl)(\cos^2 \alpha - \cos \alpha)}{(1 + 2 \cos^3 \alpha - 3 \cos^2 \alpha)} \right]^{-\frac{1}{2}}$$



V. Monoclinic lattice ( $a \neq b \neq c$ ,  $\beta \neq 90^\circ$ ,  $\alpha = \gamma = 90^\circ$ )

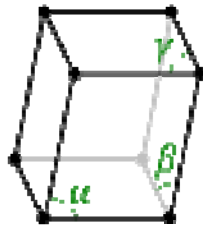
$$d = \left[ \frac{\left(\frac{h^2}{a^2}\right) + \left(\frac{l^2}{c^2}\right) - \left(\frac{2hl \cos \beta}{ac}\right)}{\sin^2 \beta} + \left(\frac{k^2}{b^2}\right) \right]^{-\frac{1}{2}}$$



VI. Triclinic lattice ( $a \neq b \neq c, \alpha = \beta = \gamma \neq 90^\circ$ )

$$d = \frac{\left( \frac{h}{a} \begin{vmatrix} \frac{h}{a} & \cos \gamma & \cos \beta \\ \frac{k}{b} & 1 & \cos \alpha \\ \frac{l}{c} & \cos \alpha & 1 \end{vmatrix} + \left( \frac{k}{b} \right) \begin{vmatrix} 1 & \frac{h}{a} & \cos \beta \\ \cos \gamma & \frac{k}{b} & \cos \alpha \\ \cos \beta & \frac{l}{c} & 1 \end{vmatrix} + \left( \frac{l}{c} \right) \begin{vmatrix} 1 & \cos \gamma & \frac{h}{a} \\ \cos \gamma & 1 & \frac{k}{b} \\ \cos \beta & \cos \alpha & \frac{l}{c} \end{vmatrix} \right)^{-\frac{1}{2}} \begin{vmatrix} 1 & \cos \gamma & \cos \beta \\ \cos \gamma & 1 & \cos \alpha \\ \cos \beta & \cos \alpha & 1 \end{vmatrix}$$

$\alpha, \beta, \gamma \neq 90^\circ$



## A2.2 WAXS of untilted and 10-degree tilted polymer-filled O-AAO-45nm pore samples

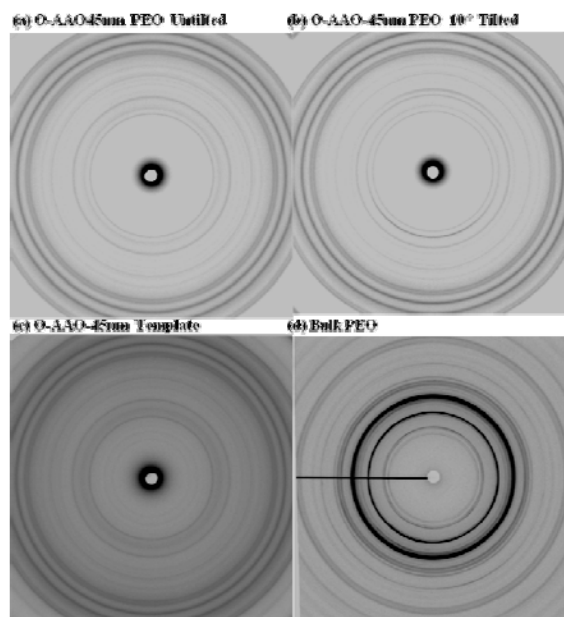


**Figure A2.1** WAXS patterns of untilted and 10 degree tilted PEO-filled O-AAO-45nm pore sample.

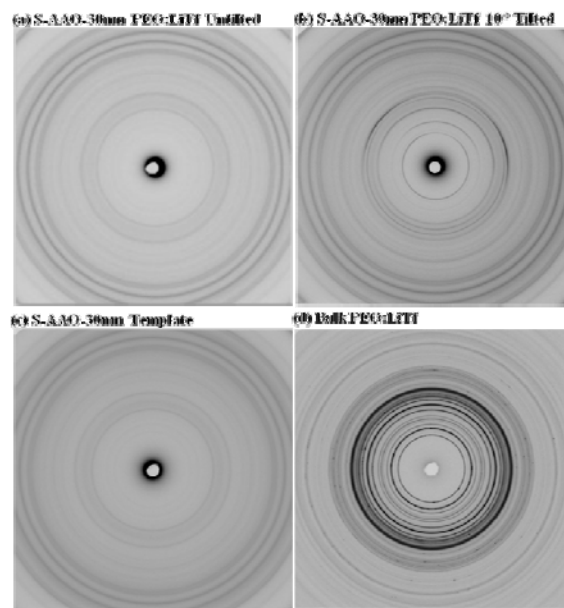


**Figure A2.2** WAXS patterns of untilted and 10 degree tilted PEO:LiTf(10:1)-filled O-AAO-45nm pore sample.

### A2.3 Tables for d-spacings, reflection angles and intensities

**Table A2.1** d-spacings, reflection angles and intensities of PEO helix-crystal.

<i>h</i>	<i>k</i>	<i>l</i>	$2\theta$	<i>d</i> (Å)	Intensity [WINCOL.CIF]
1	1	0	15.1	7.39	678
1	1	1	18.6	6.53	763
1	2	0	<b>19.2</b>	4.13	<b>6102</b>
1	2	1	22.1	3.96	593
0	0	4	22.4	2.16	508
2	0	-2	22.5	3.07	508
1	2	-4	<b>22.8</b>	1.80	<b>1356</b>
1	1	2	<b>23.0</b>	4.25	<b>6102</b>
0	3	2	<b>23.3</b>	2.39	<b>2712</b>
1	3	-2	<b>23.5</b>	2.89	<b>8983</b>
2	1	-2	<b>23.5</b>	2.89	<b>1864</b>
2	1	-5	26.2	1.49	85
0	2	4	<b>26.3</b>	1.93	<b>1610</b>
2	2	-4	<b>26.9</b>	1.68	<b>1864</b>
1	3	1	26.9	2.76	85



**Table A2.2** d-spacings, reflection angles and intensities of P(EO)<sub>3</sub>:LiTf crystal.

<i>h</i>	<i>k</i>	<i>l</i>	$2\theta$	<i>d</i> (Å)	Intensity [WINCOL.CIF]
0	0	1	10.2	14.37	2,959
0	1	1	10.3	8.61	522
2	0	0	12.3	7.19	9,917
1	1	-1	13.5	6.53	2,697
2	1	-1	15.2	3.99	1,701
2	1	0	16.1	5.52	2,241
2	0	-2	17.7	3.07	696
1	1	1	17.7	6.53	6,435
2	1	-2	20.5	2.89	696
0	0	2	20.6	4.31	1,826
0	0	0	20.6	4.31	50
3	1	0	21.2	4.19	1,739
4	0	-1	21.3	2.84	1,043
1	2	0	21.5	4.13	10,000
2	2	-2	27.3	2.50	87
3	1	1	27.5	4.69	174
1	2	-2	27.6	2.78	957



## A2.4.2 Crystalline P(EO)<sub>3</sub>:LiTf and its '.cif' file for powder diffraction

# Mercury 2.4 Output for crystalline P(EO)<sub>3</sub>-LiTf

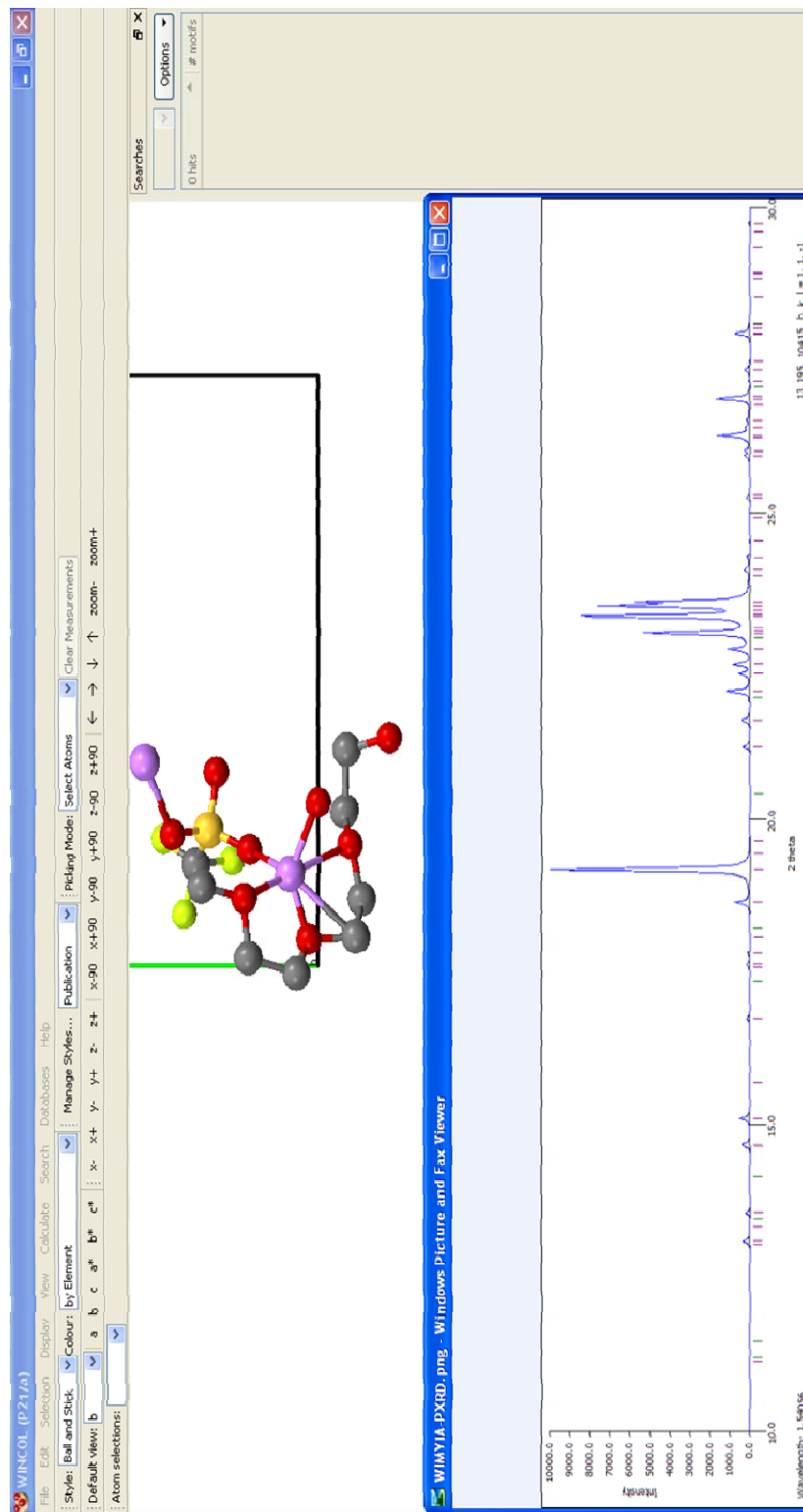


**Figure A2. 4** Mercury 2.4 program interface for crystal structure analysis of P(EO)<sub>3</sub>:LiTf and its powder-diffraction pattern analysis.

## Appendix 3: AC-impedance measurement technique

### A3.1 Introduction

A sinusoidal alternating current is applied across the sample sandwiched in between blocking or non-blocking electrodes. Here blocking electrodes stand for materials that do not undergo chemical reactions with the test material and the non-blocking electrodes interacts with the test material. Figure A3.1 shows the vector diagram (left) and the sinusoidal waveforms of alternating electric current and voltage.

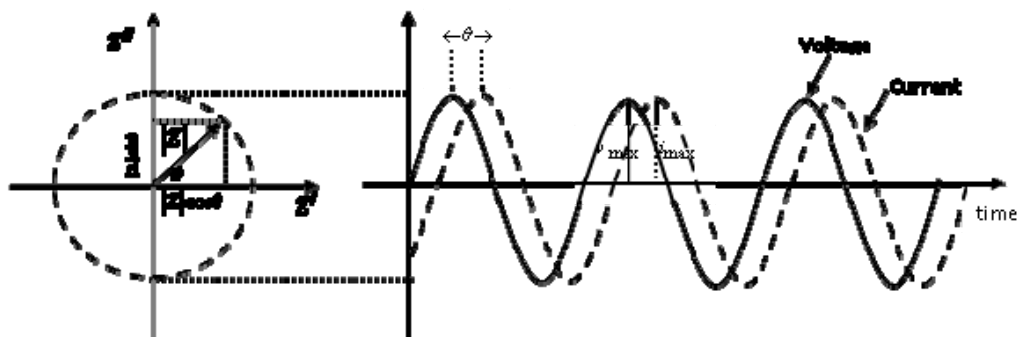


**Figure A3.1** The vector diagram (left) and sinusoidal waveforms of the current (i) and the voltage (v).

In the diagram, “ $\theta$ ” is the phase difference between the voltage and current signals,  $|Z|$  is the corresponding impedance of the test material which is responding to the voltage (v) and the current (i). From the analysis of the vector diagram, the real impedance is represented as  $|Z|\cos\theta$  and the imaginary impedance is  $|Z|\sin\theta$ . An event on vector diagram is represented as

$Z^* = Z' + jZ''$  and  $Z' = |Z| \cos \theta$  and  $Z'' = |Z| \sin \theta$ . By tracing the  $Z'$  and  $Z''$  over a frequency range (typically, mHz - KHz, Hz - MHz, Hz - GHz etc.) the fundamental electrical properties such as resistance,  $R$ , capacitance,  $C$ , admittance,  $Y^*$ , permittivity,  $\epsilon^*$ , electrical modulus,  $M^*$ , etc., of a material can be determined. The table A3-1 shows electrical properties of materials that most investigated by means of the AC-complex impedance spectroscopy.

**Table A3.1** Parameters and derivations of the electrical properties of materials.

PARAMETER	$\rho$	$\sigma$	$M$	$\epsilon$	$\chi$
$\rho = \frac{A}{l} Z =$	-	$= \frac{1}{\sigma}$	$= \frac{M}{j\omega\epsilon_o}$	$= \frac{1}{j\omega\epsilon_o\epsilon_r}$	$\frac{1}{j\omega\epsilon_o(\chi+1)}$
$\sigma = \frac{l}{A} Y =$	$= \frac{1}{\rho}$	-	$= \frac{j\omega\epsilon_o}{M}$	$= j\omega\epsilon_o\epsilon_r$	$= j\omega\epsilon_o(\chi+1)$
$M =$	$= j\omega\epsilon_o\rho$	$= \frac{j\omega\epsilon_o}{\sigma}$	-	$\frac{1}{\epsilon_r}$	$\frac{1}{\chi+1}$
$\epsilon_r = \frac{C}{C_o} =$	$= \frac{1}{j\omega\epsilon_o\rho}$	$= \frac{\sigma}{j\omega\epsilon_o}$	$= \frac{1}{M}$	-	$= \chi+1$
$\chi = \frac{C}{C_o} - 1 =$	$= \frac{1}{j\omega\epsilon_o\rho} - 1$	$= \frac{\sigma}{j\omega\epsilon_o} - 1$	$= \frac{1}{M} - 1$	$= \epsilon_r - 1$	-
$\tan\delta =$	$= \frac{\rho'}{\rho''}$	$= \frac{\sigma'}{\sigma''}$	$= \frac{M''}{M'}$	$= \frac{\epsilon''}{\epsilon'}$	$= \frac{\chi''}{\chi'+1}$

## A3.2 Representation of AC-impedance spectra of a resistor (R), a capacitor (C), and combinations in series and in parallel

### A3.2.1 Resistor (R)

The impedance of a resistor has always only a positive value in the complex plane. If there is not an electrical polarization in the material the sinusoidal signal will be always in phase with current and  $\theta=0$ , which gives  $Z^* = R$ , figure A3.2.

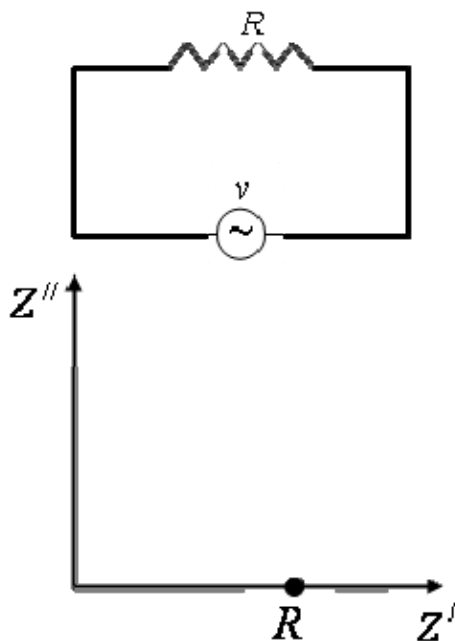


**Figure A3.2** Points for a range of frequencies on the  $Z'$  axis in the complex impedance plane for an ideal resistor, R.

### A3.2.2 Capacitance (C)

Since the capacitor electrodes are electronically charged as positive electrode and negative electrode, it responds to alternating phase differences

between the voltage and the current. The complex impedance of a capacitor,  $Z^* = \frac{-j}{\omega C}$ , which is negative due to the phase difference at  $90^\circ$  between voltage and current. By convention,  $-Z''$  is drawn in the complex plane by the electrochemists for convenience illustration. As shown in the figure A3.3 the capacitance of an ideal capacitor, over a frequency range, lie in a vertical line coincident on the imaginary axis of the complex impedance spectrum.

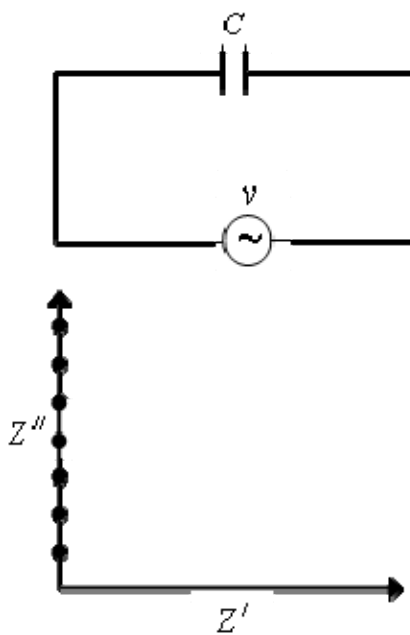


**Figure A3.3** Points for a range of frequencies on the  $Z''$  axis in the complex impedance plane for an ideal capacitor, C.

### A3.2.3 The impedance spectra of combinations of resistors and capacitors in series and parallel

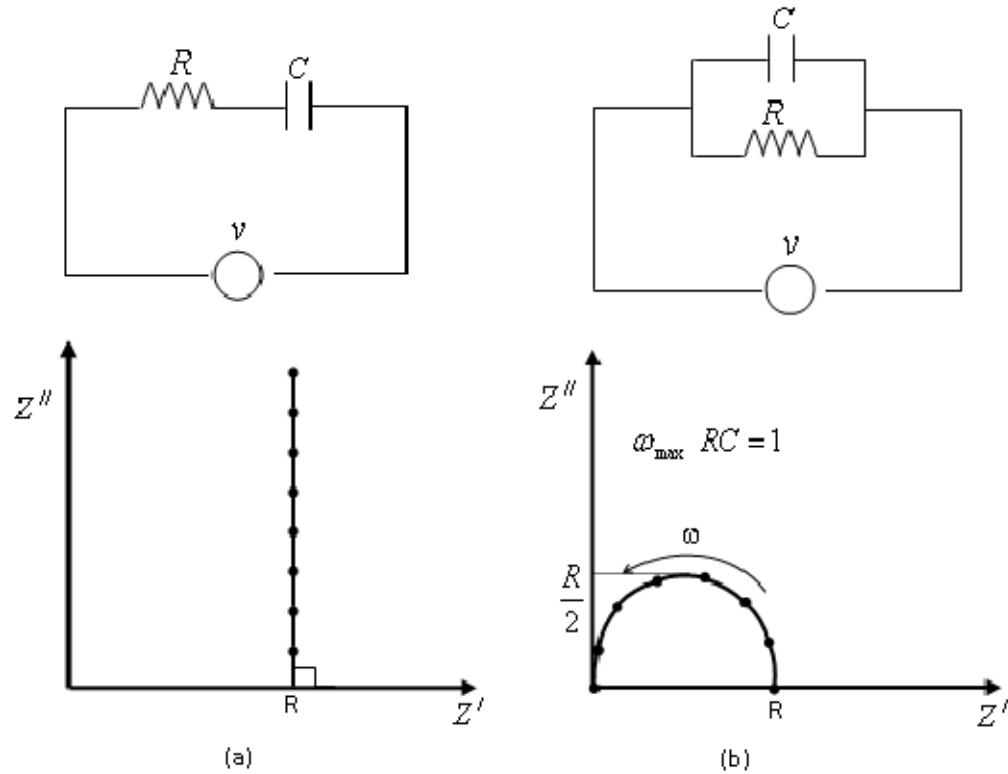


**Figure A3.4** Points for a range of frequencies in the complex impedance plane for combinations of resistors and capacitors in series (a) and parallel (b).

When resistor and capacitor are in series, figure A3.4(a),  $Z_{total}^* = R - \frac{j}{\omega C}$ , where

$Z' = R$ ,  $Z'' = \frac{-j}{\omega C}$  and the  $Z' = R$  is the DC-resistance obtain from the

interception of real axis and  $Z'' = 0$ . In resistor and capacitor are in parallel, figure A3.4(b),



$$\frac{1}{Z_{total}^*} = \frac{1}{R} + \frac{1}{1/j\omega C}$$

$$Z_{total}^* = \frac{R}{[1 + (\omega CR)^2]} - \frac{j\omega R^2 C}{[1 + (\omega CR)^2]}$$

where,  $Z' = \frac{R}{[1 + (\omega CR)^2]}$  and  $Z'' = \frac{\omega R^2 C}{[1 + (\omega CR)^2]}$

The plot of  $Z'$  against  $Z''$  follows a semi-circle with diameter  $R$  providing the geometric resistance of the circuit. In practice 'R' is obtained from the interception of  $Z'$  axis at  $Z'' = 0$ . At the maximum point on the semicircle,

$$\omega = \omega_{max}, \text{ the } Z' = Z'' \text{ and thus } C = \frac{1}{\omega_{max} R}.$$

### A3.3 AC-impedance spectrum of an electrolyte system

The figure A3.5 shows an electronic equivalent circuit for a solid electrolyte sandwiched in between two blocking electrodes, (Pt//Pt), (Au//Au), (Ag//Ag) or (SS//S). The two capacitors on either side of the circuit are representing the electrode double layer capacitances.

In the AC-impedance spectrum, the semi-circle is formed due to the parallel combination of geometrical impedance and geometrical capacitance of the electrodes. The line, called "spike" is the representation of the electrical double layer capacitances and resistance in series with the geometrical impedances. The semi circle deviation and line inclination form an ideal

electrolyte system occur due to the complex dynamic electrical relaxations in the electrolyte electrode interface and the electrode surface effects.

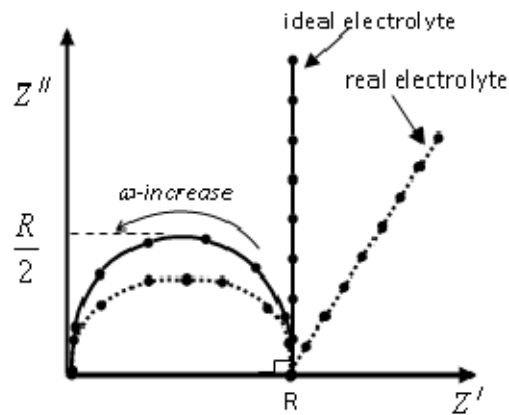
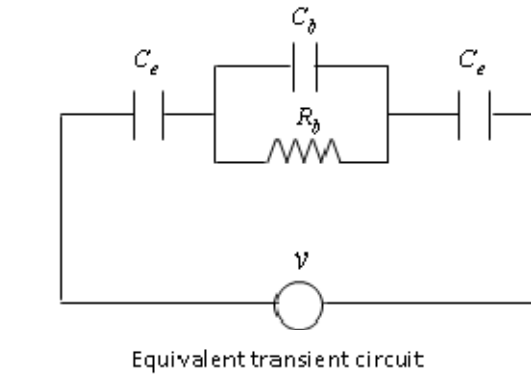


**Figure A3.5** AC-impedance spectrums for an electrolyte (solid line) and ideal electrolyte system (dash line) with blocking electrodes.

## **Appendix 4: Chemical information, sample cleaning procedure, and fabrication of AAO in detail steps.**

### **A4.1 Chemical information for AAO template fabrication**

250  $\mu\text{m}$  thick tempered as rolled Aluminum foil of purity 99.999% purchased from Goodfellow Cambridge limited. Oxalic acid dihydrate from EMD Chemicals Inc, sulfuric acid and perchloric acid (70 %) from Fisher Scientific Inc. , phosphoric acid from Sigma-Aldrich. Mercury Chloride purchased from Spectrum Chemicals Mfg. Corporation. Chromium trioxide (crystals) and degreasing organics trichloroethylene, acetone, and methyl alcohol purchased from Mallinckrodt chemicals. All chemicals are A.C.S grade.

### **A4.2 Chemical information for PEO polymer and PEO:LiTf(10:1) bulk films fabrication**

Average molecular weight ( $M_n$ ) of 3400 g/mol poly(ethylene oxide), (PEO), and lithium trifluoromethanesulfonate, (LiTf), were purchased from Sigma-Aldrich (99.995%,  $M_p = 300$  °C). Anhydrous acetonitrile of A.C.S grade (99.5%) purchased from EMD Chemicals Inc. All chemical bottles were open and used as received in dry nitrogen-filled glovebox.

### **A4.3 Sample cleaning procedure**

For sample cleaning, the following consecutive steps are carried out. First samples are degreased by sonicating in trichloroethylene, acetone, methyl alcohol,

and de-ionized water for 5 minutes each respectively, followed by drying with nitrogen. Finally, samples are UV-ozone cleaned for 30 minutes (PSC-UVT system from Novascan Technologies).

#### **A4.4 Fabrication of AAO in detail steps**

##### **A4.4.1 Cleaning and annealing Aluminum surface**

The following steps are carried out to obtain annealed and cleaned aluminum foils for anodization:

1. A piece of Al foil (15 mm x 20 mm) is cut out from the 0.25 mm thick sheet (Goodfellow Scientific).
2. The Al foil is ultrasonically cleaned for 5 minutes each in TCE, acetone, methanol, and DI water before drying with a dry nitrogen flow on filter paper.
3. The Al foil is then exposed to a UV-Ozone environment at 50 °C for 30 minutes. Both surfaces are exposed to UV when placed in the UV chamber.
4. The samples are annealed in a LINDBERG/BLUE tube furnace by first flushing with high purity N<sub>2</sub> at a flow rate of 1 LPM for 5 minutes before flowing forming gas (20% H<sub>2</sub> and N<sub>2</sub> balance) at 1 LPM and heating at 540 °C for 3 hours. The samples are then allowed to cool down to room temperature while continuing to flow the forming gas until 100 °C at which point an N<sub>2</sub> flow is introduced for 5 minutes to flush out the forming gas.

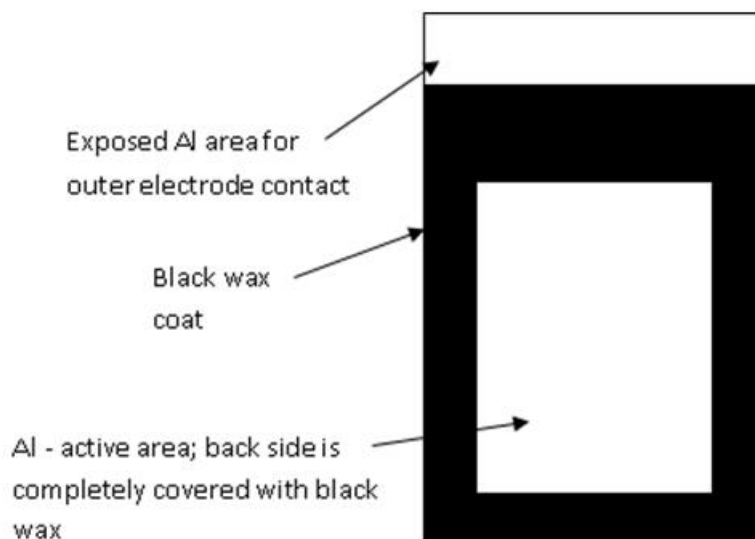
5. After the furnace has cooled down, the Al samples are removed carefully from the glass tube using tweezers.
6. (Optional) At this stage cleaning the annealed Al in a NaOH solution for 5 min can give a better cleaned surface.

#### **A4.4.2 Electro-polishing the AAO surface**

1. The electro polishing solution is made up of 3 parts ethanol and 1 part Perchloric acid.
2. Using a small amount of this solution, the container that the electro-polishing is carried out in is rinsed out along with the magnetic stirrer. The container is filled approximately two-thirds full with the electroplating solution. The container is placed in the center of a copper cooling coil and the temperature of the solution is lowered to 2 °C. There should be enough water or water/ethanol solution in the surrounding bath to allow for good thermal transfer.
3. The sample can now be coated with wax to define an electro-polishing area as shown in figure A4.1. The best temperature to apply the black wax was found to be about 150 °C.
4. The active electro-polished area is measured in square millimeters and the current limit is adjusted so that the current in milliamps is the same as the area in millimeters. The sample is electro-polished for 3 minutes. The current

should remain constant but the voltage will rise. A maximum voltage of between 60 and 120 volts should give a good finish.

5. The electro-polished piece is then removed and rinsed with DI water.
6. It is recommended that the black wax should be removed with TSC at this stage and the surface should be cleaned well as outlined in section A4.3.
7. Black wax is re-coated around the electro-polished area of the Al foil and the sample is now ready for anodization.



**FigureA4.1 Schematic** of a black wax coated aluminum.

#### **A4.4.3 Anodization steps of aluminum**

1. Attach the Platinum cathode (-) and aluminum (anode) sample ready to be anodized to the power supply terminals and then immerse both anode and

cathode into the electrolyte solution (oxalic, sulfuric, phosphoric *etc.*) respectively

2. As an example, for an AAO film anodized in oxalic acid, (O-AAO), the first anodization is carried out for about 15 hours at 40V and a temperature of 2°C.
3. When the anodization is complete, the anodized foil is rinsed with DI water and the black wax is removed with TCE and followed up with the standard cleaning steps. For the two-step anodization process, the first anodic alumina surface is removed by using chemical etching; the anodized sample is placed in a mixture of 50% chromic acid (1.8 wt%) and 50% phosphoric acid (6 wt%) at ~60°C for 4 hours which removes . The first oxide layer and exposes the dimpled aluminum surface underneath.
4. The sample is removed from the acid and cleaned with DI water and dried with dry nitrogen.
5. A new coating of black wax is applied securing the first anodized area. The sample is now ready for the second anodization.
6. The same procedure outlined in steps 1 and 2 is followed but the anodization time is tailored for the desired thickness (typically minutes) while all other conditions remain the same.
7. After the second anodization is complete, the black wax is removed with TCE followed by the rest of the cleaning procedure. The sample is now ready for use.

#### **A4.4.4 Fabrication of AAO of thickness less than 40 $\mu\text{m}$**

- 1) After the AAO film is fabricated on an Al substrate (anodized twice and pore widened if desired), the AAO is protected by covering with a coat of a micro-shield polymer using a paint brush.
  - i) A layer of the micro-shield is applied with a small paint brush. Note that bristle composition is important
    - (1) Good success has been obtained with a brush labeled “Royal 6250 Round size 0”. An important detail is to use a brush that won’t lose its bristles in the solvent (MEK) and can paint an even layer..
    - (2) Another techniques is to apply a microshield drop onto the AAO surface with a dropper filled with diluted microshield. This method was found to give no debris while preventing AAO contact with any tool.
  - ii) An even layer of the microshield should be applied over the AAO surface and extending into the outer area of the AAO region.
  - iii) A micro-shield layer approximately 5-10  $\mu\text{m}$  thick was found to be suitable
  - iv) The micro-shield layer is allowed to dry overnight although typically three hours would be adequate.
- 2) The AAO sample can be used as is or depending on the size, it can be cut into multiple pieces with distinct shapes using a razor blade into Teflon. The pieces should be asymmetric enough that the orientation (*e.g.* which side is



up) is known as shown in figure A4.2. It is useful to note the shapes in a notebook for reference. If the AAO is cut in the following manner, the orientation of the AAO film is known following lift off from the aluminum substrate since this is crucial for the rest of the processing steps.

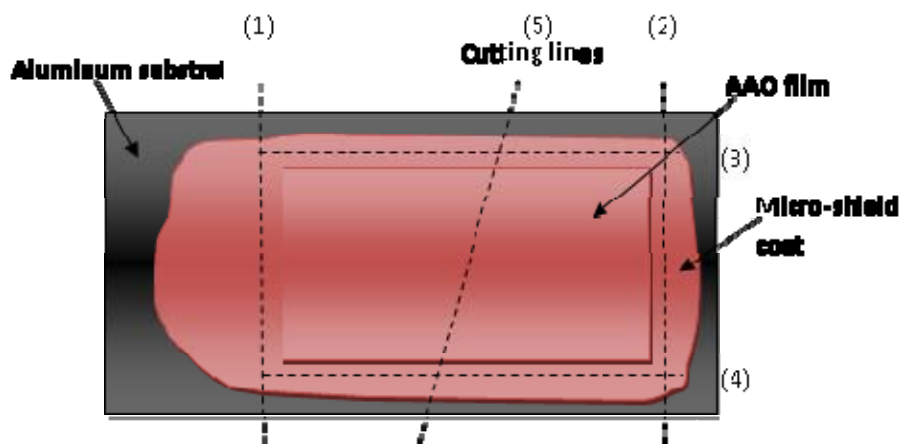


**Figure A4.2** AAO sample cutting lines for smaller sample sizes. Numbers indicate cutting sequence.

#### **A4.4.5 Removal of the aluminum substrate**

- a) A cut AAO sample with the microshield layer up is placed into a saturated  $\text{HgCl}_2$  or  $\text{CuCl}_2$  solution.
  - i) The mercury (copper) forms an amalgam with the Al and the oxide layer with the microshield will float off.
- b) This process takes 15 to 25 minutes (time depends on the sample size). It is complete when the Al/Hg or Al/Cu amalgam falls to the bottom of the beaker/Petri dish, separating from the film. If the solution is to be reused, remove the amalgam quickly to prevent exhaustion of the solution.

- c) The sample can be lifted off the surface of the liquid with flat tip tweezers on to DI water container to remove the  $\text{HgCl}_2$  from the film.

#### **A4.4.6 Removal of oxide barrier layer of AAO templates**

- 1) Two Teflon beakers (or glass) containing DI water and 5 wt.% phosphoric acid, respectively are heated to 30 °C on a hotplate.
  - a) One large Pyrex beaker (5" diameter) is placed directly on the hotplate to serve as a water bath.
  - b) A second beaker filled with the 5 wt. % phosphoric acid to a depth of ~1.5 inches is placed inside the first beaker. ( *e.g.*, a 1.5" tall 1.25" diameter polypropylene beaker filled to the neck )
  - c) The first beaker is filled with water to a depth slightly greater than the depth of the phosphoric acid. Too much water will cause the center beaker to float.
  - d) The hotplate temperature probe should be placed into the water bath so that the probe tip is near to the top of the second beaker solution level. ( *e.g.* near to the area where the AAO is placed)
  - e) A Teflon coated stir rod is added into the 5 wt.% phosphoric acid and the spin speed is set to 300 rpm.
  - f) The solution should be allowed 30 to 45 minutes to equilibrate at 30 °C before step 2 is started.

- g) Using clean flat tip tweezers, lift the AAO film and place on the 5 wt% phosphoric acid at 30 °C. The phosphoric acid solution serves as an etchant to remove the oxide barrier layer, opening the pores of the AAO from the Al substrate side.
  - h) Use a magnetic stirrer to stir the solution at 300 rpm.
  - i) The level of the etchant should be very close to the level of the water bath.
  - j) If the oxide was anodized in oxalic acid, etch for 34 minutes.
    - (a) 28 minutes has also has been used and was found to be better for 500 nm thick or thicker OAAO
  - k) If the oxide was anodized in sulfuric acid, etch for 18 minutes.
    - (a) 8 minutes is better for 500 nm thick films while 10 minutes is used for 10-20 μm thick films
- 2) A clean glass cover slide is used to lift the oxide film from the phosphoric acid solution and placed into the second DI water beaker.
- a) The oxide is left to sit in the DI water for 5 minutes or more.
- 3) If placing on a substrate:
- a) The oxide is lifted out of the water using the desired substrate instead of tweezers.
  - b) For thicker films (> 500 nm), the sample can be dried on filter paper for 1/2 hour. Kimwipes can be used for thicker samples as well.

The use of microshield for the oxide barrier removal of >40 μm thick samples is not good since the microshield remains on the pore walls and is difficult to

remove by chemical or by other means. Therefore, the sample should be self-floated on the etchant or the use of a tape window can be used surrounding the film for support and floated as shown in figure A4.3.

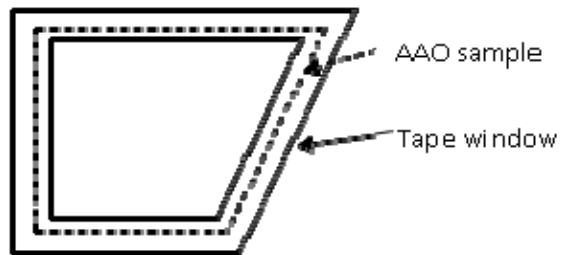


**Figure A4.3** Schematic for applying tape window for thick AAO samples when removing the oxide barrier layer.

#### **A4.5 Solution preparation data for aluminum metal anodization**

The following steps show the amount of chemical weight or volume required for diluted solution preparation:

##### **A – Commercial concentrated solution**

$$\text{Density} = d$$

$$\text{Molar mass} = M$$

$$\text{WT \%} = \alpha$$

1 – Compound mass for 1000 ml of solution

$$m_0 = d * 1000 * \alpha$$

2 – Commercial solution concentration (mole/L)

$$C_0 = m_0 / M$$

##### **B – Dilute solution needed to prepare**

Concentration dilute solution  $C_1$  (mole/L)

What volume  $V_0$  of **concentrated solution** is needed to prepare a  $V_1$  **dilute solution**?

$$V_0 = (V_1 * C_1) / C_0 \text{ weight is } m_1 = (c_1 * M / \alpha)$$

**Example: Sulfuric acid**

Density = 1.83

Molar mass = 98 g.mole<sup>-1</sup>

WT % = 95.5

Concentration of commercial solution: 17.9 M

Concentration solution we want is  $C_1 = 0.3$  M

$$m_0 = 0.3 * 98 * 100 / 95.5 = 30.78 \text{ g for 1 L}$$

Dilute solution

$$V_1 = 500 \text{ ml } m_0 = 15.39 \text{ g } V_0 = (500 * 0.3) / 17.9 = m_0 / 1.83 = 8.4 \text{ ml}$$

- a) Place 8.4 ml of the concentrated solution in graduated cylinder or a weight of 15 g
- b) Take a 600 ml Pyrex glass beaker and fill with 300 ml of DI water
- c) Add 8.4 ml of the concentration solution
- d) Fill the beaker to 500 ml with DI water
- e) Stir well

**Table A4.1.** Solution data for aluminum and titanium metal anodization.

<u>Chemical [Cl]</u>	<u>Use for</u>	<u>How to Mix Up</u>	<u>Notes</u>
0.3 M Oxalic Acid (COOH) <sub>2</sub>	Oxalic Anodization	Place 9.45 g of Oxalic Acid into 250 ml of H <sub>2</sub> O	18.90 g of Oxalic Acid into 500 ml
0.3 M Sulfuric Acid (=2.9 wt %) H <sub>2</sub> SO <sub>4</sub>	Sulfuric Anodization	7.36 g of H <sub>2</sub> SO <sub>4</sub> in 250 ml of H <sub>2</sub> O	8.4ml +up to 500ml DI
1.2 M Sulfuric Acid H <sub>2</sub> SO <sub>4</sub>	Sulfuric Anodization	Add 17 ml of H <sub>2</sub> SO <sub>4</sub> to 183 ml of H <sub>2</sub> O	Used by Moskovits' group to get small unordered pores at about 0°C
1.7 wt % Sulfuric Acid H <sub>2</sub> SO <sub>4</sub>	Sulfuric Anodization	Weigh out an amount of H <sub>2</sub> SO <sub>4</sub> (m). Then add 55.8 x m (in mL) of H <sub>2</sub> O	This is what was typically used here
10 wt% Phosphoric Acid H <sub>3</sub> PO <sub>4</sub>	Phosphoric Anodization	Add 58.54ml into 441.56ml DI water=500ml of 10wt%H <sub>3</sub> PO <sub>4</sub>	(Li et al -1998) an recipe uses 10 wt% Phosphoric at 160V to get max ordering
0.3 M Phosphoric Acid H <sub>3</sub> PO <sub>4</sub>	Phosphoric Anodization	Add 5.1 ml of H <sub>3</sub> PO <sub>4</sub> to 250 ml of H <sub>2</sub> O	(Masuda et al-1995) recipe uses 0.3M Phosphoric at 195V to get max ordering
5 wt % Phosphoric Acid H <sub>3</sub> PO <sub>4</sub>	Barrier Layer and Pore Widening Etch	Add 29.27ml into 470.73ml DI water=500ml of 5wt%H <sub>3</sub> PO <sub>4</sub>	5wt%H <sub>3</sub> PO <sub>4</sub> for Barrier Layer removal
6 wt % Phosphoric Acid H <sub>3</sub> PO <sub>4</sub>	AAO Removal Etch with 6 wt. % Phosphoric Acid (1:1)	Weigh out an amount of H <sub>3</sub> PO <sub>4</sub> (m). Then add 13.2 x m (in mL) of H <sub>2</sub> O	9.18 mL of H <sub>3</sub> PO <sub>4</sub> should weigh 15.15 g, mix with 200 mL DI water
1.8 wt % Chromic Acid	AAO Removal Etch with 6 wt. % Phosphoric Acid (1:1)	Weigh out 1.8g of CrO <sub>3</sub> . Then add 100ml DI water	Add Chromium Trioxide 3.6g into DI=200ml
<b>0.4wt% HydrogenFluoride HF</b>	<b>Ti-Anodization</b>	<b>Add 4.08ml of 49wt%HF into 250ml DI and then add DI up to 500ml</b>	<b>49wt% means 49g of HF in 100ml solution with DI water</b>
0.3 wt % NH <sub>4</sub> F + 2%H <sub>2</sub> O in EthyleneGlycol	Long TiO <sub>2</sub> nanotube growth	Add 10ml DI water into 490ml EG	3.75 mL NH <sub>4</sub> F (40%) should mix in 2% H <sub>2</sub> O:EG

## Appendix 5: SiO<sub>2</sub> deposition on oxide surfaces

### A5.1 Introduction

A uniform single layer of 2 nm thick SiO<sub>2</sub> layer deposition can be done by chemical solution adhesion on the surface. For this research work, the SiO<sub>2</sub> layers deposition were done in the inert glovebox since SiCl<sub>4</sub> decompose vigorously in normal atmosphere. SiO<sub>2</sub> layers were coated on AAO pore walls by solution depositions or following vapor depositions for below 12 nm pore sizes. According to our SEM micrograph observations following the solution deposition, below 12 nm did not show any SiO<sub>2</sub> layer deposition. In this research work, only solution deposition method was used to fabricate SiO<sub>2</sub> coated 41, 26, 22, and 18 nm pore size AAO templates since SEM macrographs showed PEO (3400 Da) molecules could only pull into 18nm pores and not less than 18nm. In general SiO<sub>2</sub> coating steps are taken place as shown in chemical equation below.



Several steps do the SiO<sub>2</sub> coating process; the solutions are vacuum-pulled consecutively through the nanopores. In section A5.2 shows brief steps for each SiO<sub>2</sub> coating for different pore diameter ranges and the “pore diameter” versus “number of layer coating” with different deposition conditions. Figure A5.1

## A5.2 Summary of SiO<sub>2</sub> deposition on AAO pore walls by vacuum-pulling method

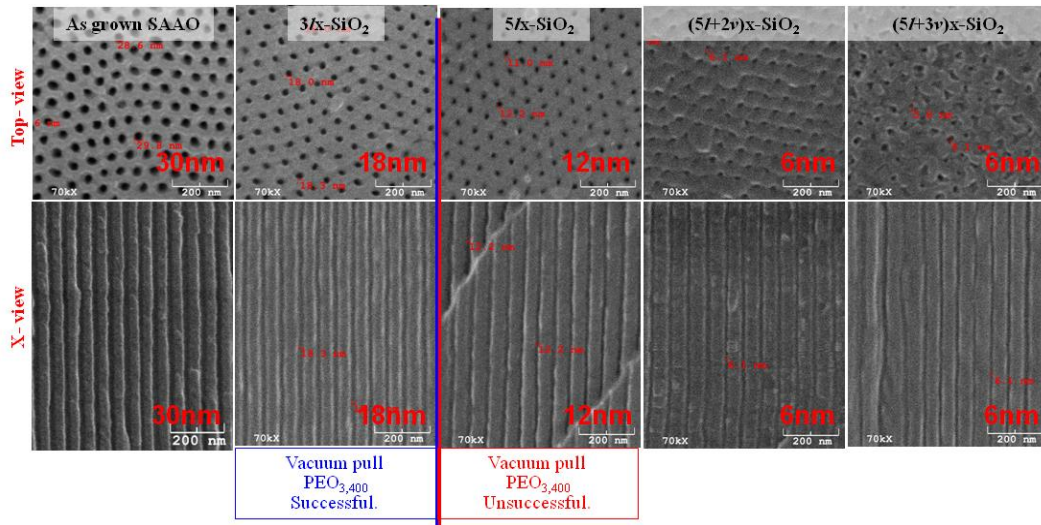
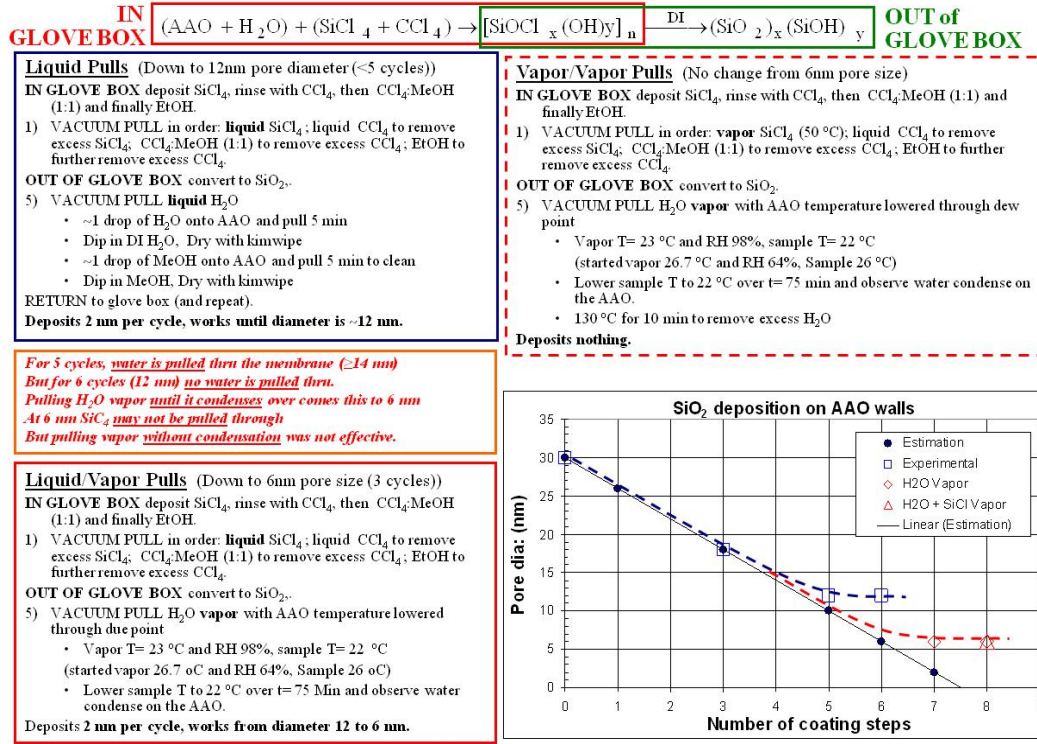
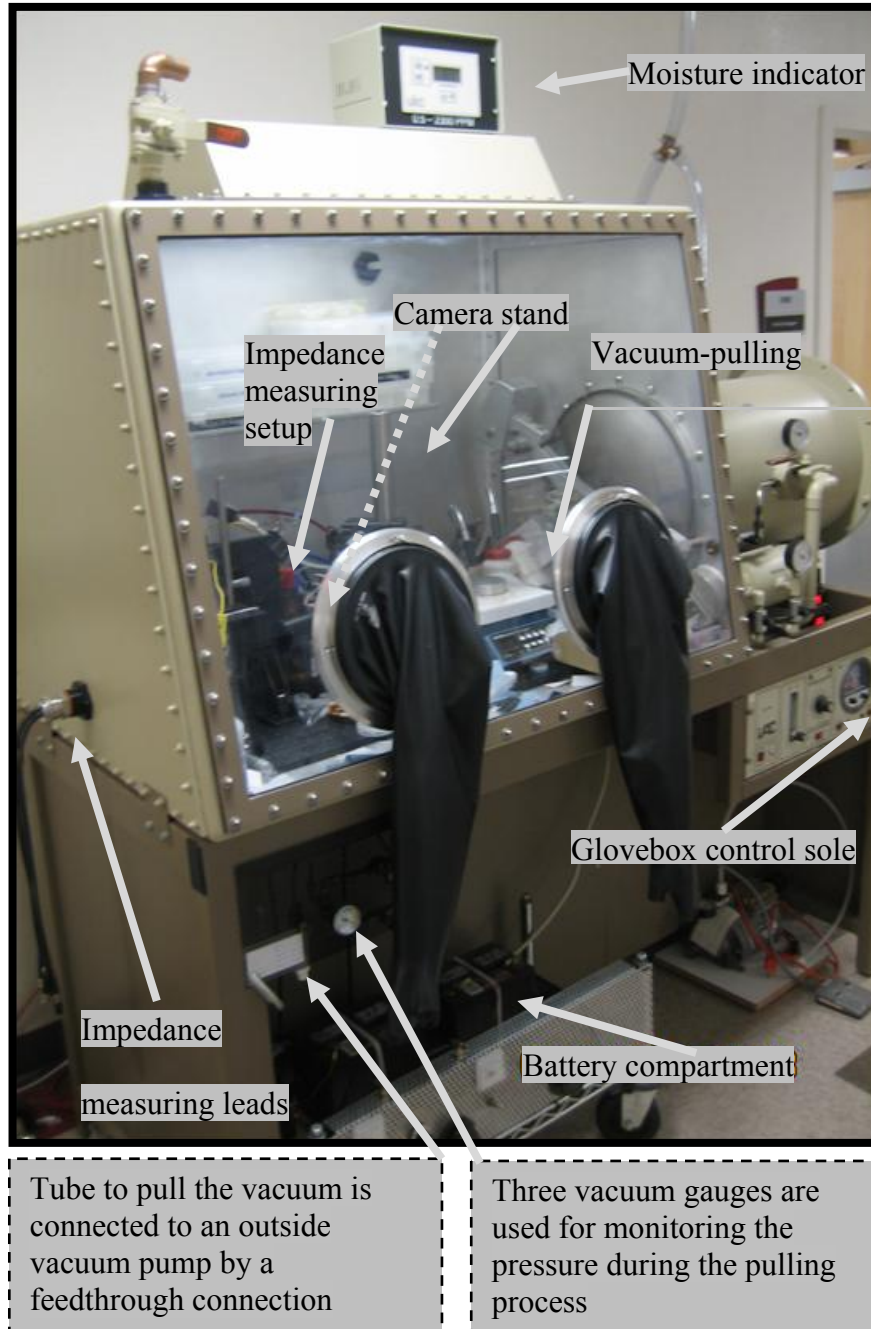


Figure A5.1 SEM micrographs of AAO pore diameter reduced down to 6nm from 30nm original size by coating SiO<sub>2</sub> layers.



## Appendix 6: Supplementary figures

### A6.1 Optical picture of the glovebox set-up



**Figure A6.1** Optical picture of the glovebox set-up used in this research work.

## A6.2. Set-up for AC-impedance measurements of AAO templates

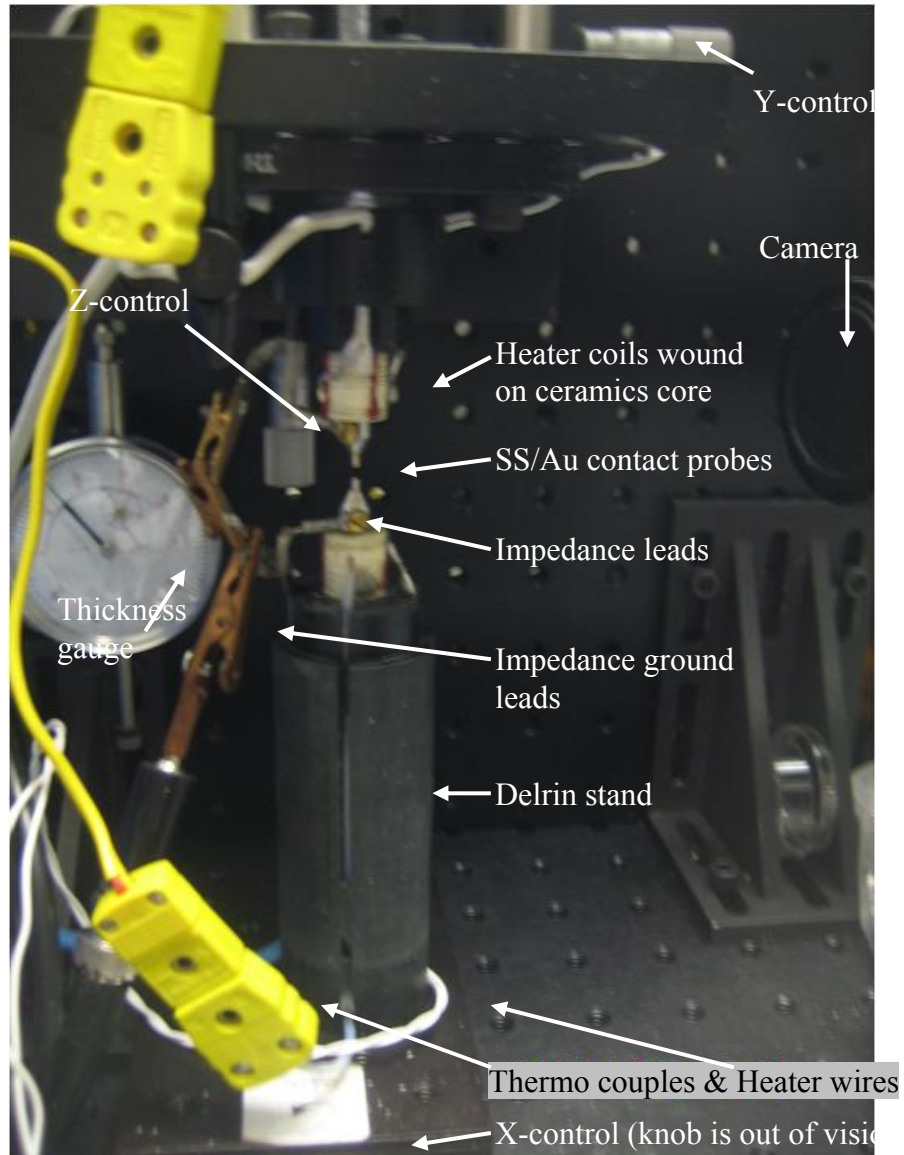


**Figure A6.2** Set-up used for AC-impedance measurements of PEO:LiTf(X:1) filled AAO templates.

# Appendix 7: Study of photo-catalysis using titanium dioxide nanotube layers

## Photo-catalysis using titanium dioxide nanotube layers

K.O. Awitor<sup>a,\*</sup>, S. Rafqah<sup>a</sup>, G. Géranton<sup>a</sup>, Y. Sibaud<sup>a</sup>, P.R. Larson<sup>b</sup>, R.S.P. Bokalawela<sup>b</sup>, J.D. Jernigen<sup>b</sup>, M.B. Johnson<sup>b</sup>

<sup>a</sup> Institut Universitaire de Technologie, Département Mesures Physiques, Université d'Auvergne, 63172 Aubière Cedex, France

<sup>b</sup> Homer L. Dodge Department of Physics and Astronomy, University of Oklahoma, Norman, OK 73019, USA

### ARTICLE INFO

#### Article history:

Received 22 February 2008  
Received in revised form 27 May 2008  
Accepted 30 May 2008  
Available online 11 June 2008

#### Keywords:

Titanium dioxide nanotubes  
Anatase  
Rutile  
Photo-degradation  
Acid orange 7 (AO7)  
Mineralization

### ABSTRACT

Photo-degradation of acid orange 7 in aqueous solution was used as a probe to assess the photo-catalytic activity of titanium dioxide nanotube layers under UV irradiation. The nanotube layers were prepared by anodization of Ti foil in 0.4 wt% hydrofluoric acid solution and then annealed at different temperatures between 300 °C and 600 °C for 1 h. The nanotube layers were characterized using X-ray diffraction and scanning electron microscopy. After the 500 °C anneal, the anatase and rutile mass fractions were measured to be about 55% and 45%, respectively. After annealing at 500 °C, the anatase crystallite size was maximum while the size and shape of the nanotubes remain unaffected. Such TiO<sub>2</sub> nanotube layers showed strong photo-catalytic activity. During UV irradiation, we measured the total disappearance of the organic carbon and the formation of anion species to confirm the total mineralization of the acid orange 7.

© 2008 Elsevier B.V. All rights reserved.

### 1. Introduction

Titanium dioxide (TiO<sub>2</sub>) is a photo-catalytic material with applications in fields such as environmental purification, decomposition of carbonic acid gases, and solar cells [1–7]. Several techniques can be used to prepare TiO<sub>2</sub> thin films, including thermal oxidation of titanium and sputtering [8–13]. TiO<sub>2</sub> nanotube layers grown by anodic oxidation of Ti foils in an appropriate electrolyte provide ordered nanotube arrays with high surface area to volume ratios [14–17]. Such layers have attracted much attention, including recent work on wetting behaviour [18], oxygen adsorption [19], and heterogeneous photo-catalysis [14]. One of the most active research areas has been focused on environmental remediation, including self-cleaning materials. For example, TiO<sub>2</sub>-based photo-catalysts have been used to break down organic compounds in wastewater [1,3,5]. Indeed, many organic pollutants can be degraded and ultimately mineralized using TiO<sub>2</sub> photo-catalysts in the presence of UV radiation [14,20–25]. Recently, there have been studies investigating the degradation of organic solutions using TiO<sub>2</sub> nanotube layers [4,14]. The nanotube layers give rise to a large specific surface area and this should produce a greater photo-catalytic activity for a given sample size. In this work, we assess the photo-catalytic

activity of TiO<sub>2</sub> nanotube layers by monitoring the degradation of an acid orange 7 (AO7) dye solution. The TiO<sub>2</sub> nanotube layers were annealed in an oxygen atmosphere at different temperatures. The study of structural evolution versus annealing temperature performed by X-ray diffraction shows that at 500 °C the anatase and the rutile mass fractions are around 55% and 45%, respectively. At this temperature, the size of the anatase crystallites was maximum and the TiO<sub>2</sub> nanotubes demonstrated strong photo-catalytic activity under UV irradiation. Scanning electron microscopy (SEM) was used to study the nanotube morphology. Finally, we show that the photo-catalytic activity of TiO<sub>2</sub> nanotube layers leads to the total mineralization of AO7.

### 2. Experimental details

To fabricate anodic TiO<sub>2</sub> nanotube layers, we used Ti foil (Goodfellow, 99.6% purity) with a thickness of 0.025 mm. The Ti foils were degreased by successive sonication in trichloroethylene, acetone, and methanol, followed by rinsing with deionized water and blown dry with nitrogen. Anodization was carried out at room temperature (20 °C) in 0.4 wt% HF aqueous solution with the anodizing voltage maintained at 20 V.

The crystalline structure and phase of the TiO<sub>2</sub> nanotube layers were determined using a Scintag XRD X'TRA diffractometer with Cu K $\alpha$  radiation. A JEOL JSM-880 SEM was used for morphological characterization.

\* Corresponding author. Tel.: +33 4 73 17 71 66; fax: +33 4 73 17 71 71.  
E-mail address: awitor@ut.u-clermont1.fr (K.O. Awitor).

Photo-degradation of AO7 in aqueous solution was used as a probe to assess the photo-catalytic activity of TiO<sub>2</sub> nanotube layers. Photo-catalytic experiments were conducted in 15 mL of AO7 solution (from Acros Organics, also called Orange II, CAS# 633-96-5) with a concentration of  $5.0 \times 10^{-5}$  mol/L, placed in a cylindrical Pyrex glass reactor (1.1 cm diameter by 18 cm tall). The surface area of the anodized samples was approximately 6.5 cm<sup>2</sup>. The glass reactor was irradiated with polychromatic fluorescent UV lamps (Philips TDL 8 W (total optical power, 1.3 W), 300 mm long, wavelength range 350–400 nm) in a configuration providing about 2 mW/cm<sup>2</sup> at the sample surface.

The photo-catalytic decomposition of AO7 solution was monitored by the decrease of the solution's absorbance at 254 nm (centered in an absorption band of the AO7 solution), using a Merck high-performance liquid chromatography (HPLC) system. This HPLC system was equipped with a mono-channel (L-7400) UV-vis detector, an automatic injector (L7200) and pump (L7100). Experiments to investigate the decomposition of AO7 under UV irradiation into smaller organic molecules were performed using a reverse phase Interchrom column (Hypersil H<sub>5</sub>C<sub>18</sub>, 150 mm long  $\times$  4.6 mm diameter) to analyze the solution. The flow rate of AO7 solution was 1.0 mL/min and the injected volume was 10  $\mu$ L. The elution was accomplished by water with ammonium acetate ( $25 \times 10^{-3}$  mol/L) and acetonitrile (75/25, v/v) with a flow rate of 1.0 mL/min. We followed the evolution of the 485 nm band of the irradiated solution using a UV-vis and IR spectrometer (Shimadzu UV-2101). The progress of the mineralization of AO7 solution was monitored by measuring the total organic carbon (TOC) using a Shimadzu Model TOC-5050A system, equipped with an automatic sample injector. The calibration curve within the range 1–15 mg/L was obtained by using potassium hydrogen phthalate, K<sub>8</sub>H<sub>5</sub>O<sub>4</sub>, and sodium hydrogen carbonate, NaHCO<sub>3</sub>, for organic and inorganic carbon, respectively. The evolution of nitrate, nitrite and sulphate ion concentrations was obtained as a function of irradiation time

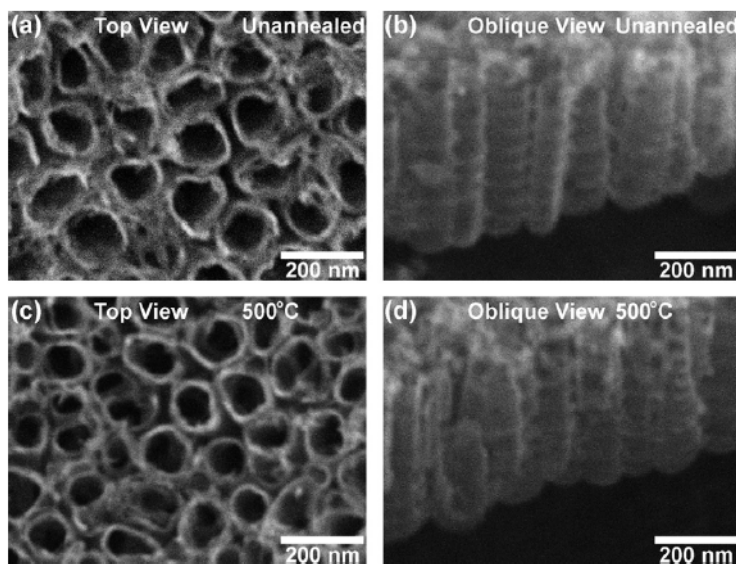
using a Dionex, DX-100, ionic chromatography system. The elution was accomplished using Na<sub>2</sub>CO<sub>3</sub> ( $1.8 \times 10^{-3}$  mol/L)/NaHCO<sub>3</sub> ( $1.7 \times 10^{-3}$  mol/L) with a flow rate of 2.0 mL/min.

### 3. Results and discussion

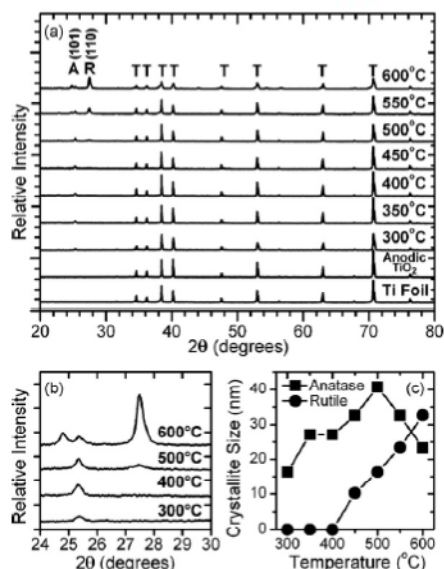
#### 3.1. TiO<sub>2</sub> nanotube layer characteristics

Fig. 1 shows SEM images of the TiO<sub>2</sub> nanotubes obtained by anodizing a Ti foil. We observe ordered nanotube arrays grown on top of the Ti foil with an oxide barrier layer separating the nanotubes from the titanium foil. Fig. 1(a) shows the top down image of the ordered array of TiO<sub>2</sub> nanotubes in the unannealed state approximately 100 nm in diameter. Fig. 1(b) shows an oblique view of the unannealed TiO<sub>2</sub> nanotubes (55° from normal). The tube length determined by accounting for foreshortening from this image was found to be approximately 430 nm. Fig. 1(c and d) shows top and oblique views after annealing at 500 °C. Comparing before and after views, we see no difference in the micrographs. Thus the size and shape of the nanotubes are not affected by the 500 °C anneal.

Fig. 2 summarizes the X-ray characterization of Ti foil and TiO<sub>2</sub> nanotube layers before and after annealing at different temperatures in oxygen for 1 h. The unannealed TiO<sub>2</sub> nanotube layer exhibits only the peaks from titanium metal foil under the nanotube layer. In order to convert the nanotube layer to a crystalline phase, the samples were annealed at 300–600 °C in increments of 50 °C. The characteristic line of anatase (1 0 1) appears at 300 °C, while the rutile line (1 1 0) appears at 500 °C. These lines are shown in more detail in Fig. 2(b). Crystallite size was calculated using the Scherrer formula,  $D = 0.94\lambda / \beta \cos \theta$ , where  $\lambda$  is the wavelength of the Cu K $\alpha_1$  line,  $\theta$  is the Bragg diffraction angle, and  $\beta$  is the full-width at half max (FWHM) of a peak. We calculated the crystallite size



**Fig. 1.** SEM images of TiO<sub>2</sub> nanotubes obtained by anodizing Ti foil. (a) Top view image of the ordered array of unannealed TiO<sub>2</sub> nanotubes showing typical diameter to be about 100 nm. (b) Oblique view (55° from normal) of the unannealed TiO<sub>2</sub> nanotubes showing tube length of about 430 nm. (c) Top view of TiO<sub>2</sub> nanotube array annealed at 500 °C. (d) Oblique view (55° from normal) of TiO<sub>2</sub> nanotube array at 500 °C.



**Fig. 2.** (a) X-ray diffraction patterns of Ti foil, as grown and annealed TiO<sub>2</sub> nanotube layers. Annealing temperatures are marked. Lattice planes indicate anatase (A), rutile (R), and titanium (Ti). (b) Evolution of the (1 0 1) anatase, and (1 1 0) rutile lines at 300–600 °C. (c) Peak heights of (1 0 1) anatase and (1 1 0) rutile lines, and crystallite size for anatase and rutile phases (calculated using Scherrer's formula) versus temperature.

evolution by using the FWHM of the anatase (1 0 1) and the rutile (1 1 0) peaks. Fig. 2(c) is a plot of crystallite size versus temperature. We found that the size of anatase grows from 17 nm to 40 nm as the annealing temperature is increased from 300 °C to 500 °C. The rutile crystallite size was 17 nm at 500 °C. After 500 °C, the anatase peak decreases significantly while the rutile peak increases. At 500 °C the anatase-to-rutile mass ratio was around 55:45. The anatase-to-rutile mass ratio decreased to 30:70 and further to 20:80 after one-hour annealing at 550 °C and 600 °C, respectively. It is interesting to note, that even after annealing at 500 °C the size and shape of the nanotubes were not observed to change, while the crystalline structure clearly does change. This is in agreement with the results described by Varghese et al. [15] and Macak et al. [14].

### 3.2. Photo-catalytic activity study

The photo-degradation of AO7 in the presence of TiO<sub>2</sub> nanotubes under different conditions is summarized in Fig. 3. This shows the AO7 concentration versus time as determined by the solution's absorbance at 254 nm. As shown in Fig. 4, a plot of absorption versus wavelength, 254 nm is at the center of an AO7 absorption band. For Fig. 3, the initial concentration of the AO7 was  $5.0 \times 10^{-5}$  mol/L. Fig. 3, curve (a) shows the photo-degradation of AO7 under UV light without TiO<sub>2</sub> present. This result indicates that AO7 is not substantially degraded by UV radiation alone. Curve (b) shows that the reduction in the concentration of AO7 in the presence of TiO<sub>2</sub> nanotubes for 40 h without UV irradiation was about 20%. Thus, the effect of adsorption of the dye on the TiO<sub>2</sub> surface is small but not negligible. Curve (c) shows the variation in the concentration of AO7 in the presence of unannealed TiO<sub>2</sub> nanotubes under UV irradiation. Here we only observe the adsorption effect. Curves (d), (e) and

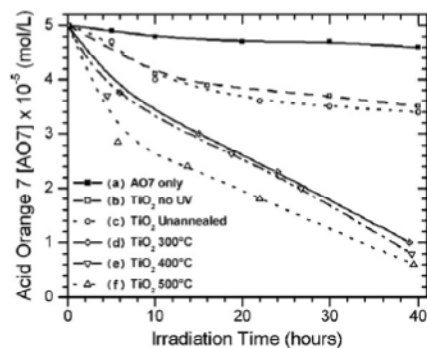


**Fig. 3.** Photo-degradation of acid orange 7 (AO7) dye under UV-lamp irradiation at wavelengths of 350–400 nm in the presence of TiO<sub>2</sub> nanotube layer, as measured by the absorbance of the irradiated dye at 254 nm. (a) AO7 only with UV; (b) AO7 with TiO<sub>2</sub> nanotube layer without UV; (c) unannealed TiO<sub>2</sub> nanotube layer; (d) TiO<sub>2</sub> nanotube layer annealed at 300 °C; (e) TiO<sub>2</sub> nanotube layer annealed at 400 °C; (f) TiO<sub>2</sub> nanotube layer annealed at 500 °C.

(f) illustrate photo-degradation of AO7 after the samples had been annealed at 300 °C, 400 °C and 500 °C, respectively. We observed a complete de-colorization of the AO7 dye after 40 h. These results show the decay of organic molecules with UV irradiation in the presence of the annealed nanotubes.

We observed the strongest photo-catalytic activity for the sample annealed at 500 °C. In this case, the kinetics are first order with a rate constant of about  $0.05 \text{ h}^{-1}$ . At this temperature the anatase-to-rutile mass fraction is about 55:45 and the anatase crystallite size of 40 nm was maximum. It seems that the TiO<sub>2</sub> nanotube layers show strong photo-catalytic activity when composed of mixed crystalline phases (anatase and rutile) with excess anatase. This behaviour is similar to that for the crystalline powder Degussa P25, which exhibits a strong photo-catalytic activity and has an anatase-to-rutile mass fraction of 80:20. Our results are in agreement with those observed by Macak et al. [14] for the de-colorization of AO7 dye. The difference in the rate constant of Macak et al. compared to our rate constant ( $0.63 \text{ h}^{-1}$  vs.  $0.05 \text{ h}^{-1}$ ) is due to differences in their experiment to our experiment: nanotube length (0.5 μm vs.

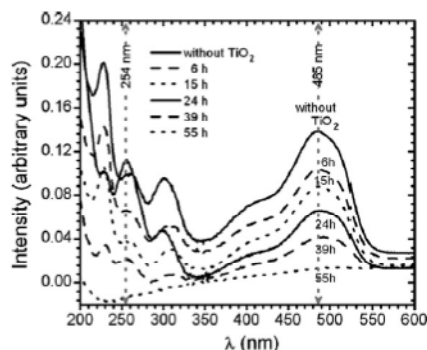


**Fig. 4.** Absorption versus irradiation time for the acid orange 7 (AO7) for polychromatic light (350–400 nm) without TiO<sub>2</sub> nanotube layers, and in the presence of TiO<sub>2</sub> nanotube layers annealed at 300 °C with exposure times of 6 h, 15 h, 24 h, 39 h, and 55 h, as labelled.

0.43  $\mu\text{m}$ ), illuminated sample area (1  $\text{cm}^2$  vs. 6.5  $\text{cm}^2$ ), intensity at the sample (60  $\text{mW}/\text{cm}^2$  vs. 2  $\text{mW}/\text{cm}^2$ ), and AO7 volume (3 mL vs. 15 mL). In detail, taking our rate constant of  $0.05 \text{ h}^{-1}$  and converting it to the experimental situation of Macak et al., we expect a rate constant of  $0.05 \text{ h}^{-1} \times (0.5/0.43) \times (1/6.5) \times (60/2)/(3/15)$ , or  $1 \text{ h}^{-1}$ , which is in reasonable agreement with Macak's rate constant of  $0.63 \text{ h}^{-1}$  (see [26]).

It is useful to compare the photo-catalytic activity of this  $\text{TiO}_2$  nanotube surface with other  $\text{TiO}_2$  surfaces. Macak et al. compares the activity of a similar nanotube surface to a standard preparation of Degussa P25 powder and finds comparable activity for equal illuminated sample areas ( $0.63 \text{ h}^{-1}$  vs.  $0.50 \text{ h}^{-1}$ ). This indicates that the  $\text{TiO}_2$  nanotube surface is promising. Comparing our  $\text{TiO}_2$  nanotube surface to an optimized sputter-deposited  $\text{TiO}_2$  surface [27] (sputtered from a Ti target in a reactive  $\text{Ar-O}_2$  gas mixture) we find similar rate constants, even though the sputtered  $\text{TiO}_2$  surface has a lower specific area in comparison. This implies the photo-catalytic activity of the surface of the  $\text{TiO}_2$  nanotubes is lower than that of an optimized sputtered surface, indicating there is room for improvement in the activity of the surface of the  $\text{TiO}_2$  nanotubes.

Fig. 4 shows typical UV-vis spectra obtained during UV irradiation of AO7 in the presence of the  $\text{TiO}_2$  nanotubes annealed at  $300^\circ\text{C}$ . (Results for nanotube layers annealed at the higher temperatures are similar.) These spectra clearly show that the intensity of the characteristic band of AO7 at 485 nm decreases as a function of irradiation time, so that after 50 h of irradiation the AO7 solution is colorless.

Mineralization of AO7 was studied by following the disappearance of the total organic carbon (TOC), as shown in Fig. 5. The formation of anion species (nitrites, nitrates, and sulphates) was followed by using ionic liquid chromatography during irradiation. Fig. 5 shows that the  $\text{TiO}_2$  nanotube structure is efficient at eliminating the AO7 dye in aqueous solution. During the UV irradiation, a rapid decrease in the number of carbon atoms was observed corresponding to the scission and oxidation of AO7.

Conversely, Fig. 6 shows the increase of the concentration of anions (formed after mineralization) with irradiation time. The chemical formula for AO7 is  $\text{HOC}_{10}\text{H}_6\text{N}=\text{NC}_6\text{H}_4\text{SO}_3\text{Na}$ , so there is one sulphur atom and two nitrogen atoms for every AO7 molecule. Regarding sulphur, the concentration of sulphates reaches a plateau of about 4.7  $\text{mg}/\text{L}$  or  $4.9 \times 10^{-5} \text{ mol}/\text{L}$ . Given the starting concentration of AO7 is  $5.0 \times 10^{-5} \text{ mol}/\text{L}$ , essentially all (98%) of the sulphur in the starting AO7 is converted into sulphates. Regarding nitro-

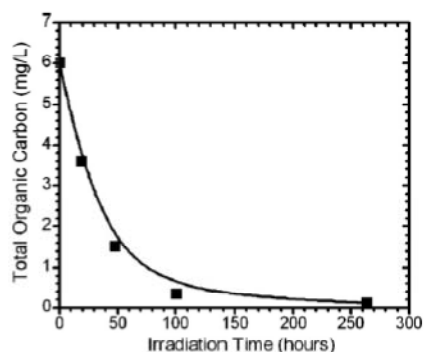


Fig. 5. The evolution of total organic carbon (TOC) of acid orange 7 (AO7) dye (starting concentration  $5.0 \times 10^{-5} \text{ mol}/\text{L}$ ) versus irradiation time in the presence of a  $\text{TiO}_2$  nanotube layer annealed at  $500^\circ\text{C}$ .

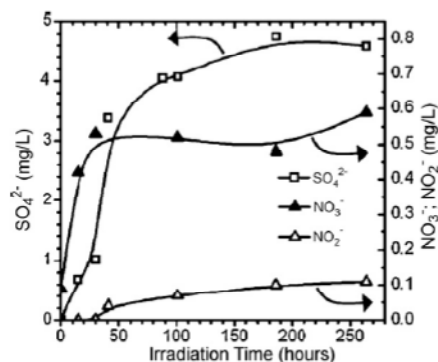


Fig. 6. Formation of inorganic anions, nitrates, nitrites, and sulphates, upon UV irradiation of AO7 dye in the presence of a  $\text{TiO}_2$  nanotube layer annealed at  $500^\circ\text{C}$ .

gen, the formation of the nitrate and nitrite ions reached a plateau in concentration of 0.6  $\text{mg}/\text{L}$  or  $1 \times 10^{-5} \text{ mol}/\text{L}$ , and 0.1  $\text{mg}/\text{L}$  or  $0.2 \times 10^{-5} \text{ mol}/\text{L}$ , respectively. Taking into account the two N atoms in AO7, 10% (2%) of the nitrogen ends up as nitrate (nitrite). This suggests the remaining 88% of the nitrogen forms  $\text{N}_2$  [20,24] and/or ammonium ions that are not directly tracked [21,25].

#### 4. Conclusions

Photo-degradation and the mineralization capacity of  $\text{TiO}_2$  nanotube layers were studied using AO7 in aqueous solution as a probe. Anodization of Ti foil results in ordered arrays of  $\text{TiO}_2$  nanotubes. The  $\text{TiO}_2$  nanotube layers annealed at  $500^\circ\text{C}$  for 1 h in oxygen show strong photo-catalytic activity, in agreement with earlier studies [14]. After this anneal, X-ray diffraction indicated the nanotube layer is composed of mixed crystalline phases (anatase and rutile) with an excess of anatase in agreement with the earlier work [14–16]. For the nanotube layer annealed at  $500^\circ\text{C}$  we observe the breakdown of AO7 by following the absorption of the UV-irradiated solution at 254 nm. Complete de-colorization of the AO7 dye was observed after 40 h. The mineralization of the AO7 was confirmed by direct measurement of the reduction of total organic carbon, and by the direct measurement of the increase in the concentration of sulphate, nitrate and nitrite anions in the UV-irradiated solution.

#### References

- [1] S.-A. Lee, K.-H. Choo, C.H. Lee, H.-I. Lee, T. Hyeon, W. Choi, H.-H. Kwon, *Ind. Eng. Chem. Res.* 40 (2001) 1712.
- [2] W. Choi, *Catal. Surv. Asia* 10 (2006) 16.
- [3] J. Ryu, W. Choi, *Environ. Sci. Technol.* 42 (2008) 294.
- [4] G.K. Mor, M.A. Carvalho, O.K. Varghese, M.V. Pishko, C.A. Grimes, *J. Mater. Res.* 19 (2004) 628.
- [5] Y. Xiong, P.J. Strunk, H. Xia, X. Zhu, H.T. Karlsson, *Water Res.* 35 (2001) 4226.
- [6] T. Kasuga, M. Hiramatsu, M. Hirano, A. Honson, K. Oyamada, *J. Mater. Res.* 12 (1997) 607.
- [7] M.R. Hoffmann, S.T. Martin, W. Choi, D.W. Bahnemann, *Chem. Rev.* 95 (1995) 69.
- [8] I. Saeki, N. Okushi, H. Konno, R. Furuichi, *J. Electrochem. Soc.* 143 (1996) 2226.
- [9] B. Karunakaran, R.T.R. Kumar, D. Mangalaraj, S.K. Narayandass, G.M. Rao, *Cryst. Res. Technol.* 37 (2002) 1285.
- [10] M.C. Barnes, S. Kumar, L. Green, N.-M. Hwang, A.R. Gerson, *Surf. Coat. Technol.* 190 (2005) 321.
- [11] P. Hoyer, H. Masuda, *J. Mater. Sci. Lett.* 15 (1996) 1228.
- [12] S.-Z. Chu, K. Wada, S. Inoue, S.-I. Todoroki, *Chem. Mater.* 14 (2002) 266.
- [13] H. Imai, Y. Takei, K. Shimizu, M. Matsuda, H. Hirashima, *J. Mater. Chem.* 9 (1999) 2971.
- [14] J.M. Macak, M. Zlamal, J. Krýsa, P. Schmucki, *Small* 3 (2007) 300.

- [15] O.K. Varghese, D. Gong, M. Paulose, C.A. Grimes, E.C. Dickey, J. Mater. Res. 18 (2003) 156.
- [16] D. Gong, C.A. Grimes, O.K. Varghese, W. Hu, R.S. Singh, Z. Chen, E.C. Dickey, J. Mater. Res. 16 (2001) 3331.
- [17] V. Zwilling, M. Aucouturier, E. Darque-Ceretti, Electrochim. Acta 45 (1999) 921.
- [18] E. Balaur, J.M. Macak, H. Tsuchiya, P. Schmuki, J. Mater. Chem. 15 (2005) 4488.
- [19] S. Funk, B. Hokkanen, U. Burghaus, A. Ghicov, P. Schmuki, Nano Lett. 7 (2007) 1091.
- [20] M.A. Behnajady, N. Modirshahla, N. Daneshvar, M. Rabbani, Chem. Eng. J. 127 (2007) 167.
- [21] K. Tanaka, K. Padermpole, T. Hisanaga, Water Res. 34 (2000) 327.
- [22] E. Vuillet, C. Emmelin, J.-M. Chovelon, C. Guillard, J.-M. Herrmann, Environ. Chem. Lett. 1 (2003) 62.
- [23] J. Fernández, J. Kiwi, J. Baeza, J. Freer, C. Lizama, H.D. Mansilla, Appl. Catal. B Environ. 48 (2004) 205.
- [24] H. Lachheb, E. Puzenat, A. Houas, M. Ksibi, E. Elaloui, C. Guillard, J.-M. Herrmann, Appl. Catal. B Environ. 39 (2002) 75.
- [25] H. Kyung, J. Lee, W. Choi, Environ. Sci. Technol. 39 (2005) 2376.
- [26] The experimental rate constant, determined by the decrease in A07 concentration, should be proportional to tube length, sample area, and UV intensity, while inversely proportional to the volume of the A07 solution. Actually, Macak et al. see diminishing improvement with longer tube length, but this is not important here because the difference in nanotube lengths is very small.
- [27] K.O. Awitor, A. Rivaton, J.-L. Gardette, A.J. Down, M.B. Johnson, Thin Solid Films 516 (2008) 2286.

## Appendix 8: Glossary

Al	Aluminum
Au	Gold
Li	Lithium
LiTf	Lithium-trifluoromethanesulfonate
Pt	Platinum
KBr	Potassium Bromide
LaB6	Lanthanum hexaboride
Nd:YAG	Neodymium Yttrium Aluminum Garnet
ZnSe	Zinc Selenide
PAN	Poly(acrylonitrile)
PEI	Poly(ethylene imine)
PEO	Poly(ethylene oxide)
PMMA	poly(methyl methacrylate)
PPO	Poly(propylene oxide)
PTFE	Poly(tetrafluoroethylene)
PVDF	poly(vinylidene fluoride)
MFC	Methanol fuel cells
PEMFC	Proton exchange membrane fuel cell
AAO	Anodic aluminum oxide
O-AAO	Oxalic-anodic aluminum oxide
S-AAO	Sulfuric-anodic aluminum oxide
FTIR	Fourier transformed infra-red
NMR	Nuclear magnetic resonance
SAXS	Small angle x-ray scattering
SEM	Scanning electron microscopy
WAXS	Wide angle x-ray scattering
AC	Alternating current
C	Capacitance
DC	Direct current
R	Resistance
$\sigma$	Conductivity
CRT	Cathode ray tube
VTF	Vogel-Tamman-Fulcher
WLF	Willams-Landel-Ferry
RF	Radio frequency
UV	Ultra-violet
S/N	Signal-to-noise
A	Area
C-C	Center-to-center
FWHM	Full width half maximum
P	Porosity factor